INTERACTION NOTES

Note 313

October 1976

A Transmission Line Corona Experiment

Philip S. Book
Harold J. Price

Kaman Sciences Corporation
Colorado Springs, Colorado

ABSTRACT

Because of possible importance of corona effects to EMP analysis and hardening programs, a two-part study program was undertaken: first, an experimental phase to measure electric and magnetic fields of a transmission line structure with corona; second, an analytical phase to develop a simple corona model and determine the model parameters from the test data.

ACKNOWLEDGMENT

The authors would like to express their appreciation to various individuals at the Air Force Weapons Laboratory (AFWL) and Kaman Sciences Corporation (KSC) who contributed to this study program, specifically, to Dr. J. Philip Castillo and Dr. Carl E. Baum of AFWL who provided technical assistance to both the experimental analytical phases of the program; to the Project Officer, TSGT Harris A. Goodwin who arranged for the loan of needed equipment and provided other administrative support; to Dr. Walter E. Ware of KSC who assisted with the analytical phase of the program; to John W. Erskine of KSC for his guidance in the design of the test facility and high-voltage pulser; and to Louis Ortiz and Roger Baer who constructed the test facility and performed much of the experimental work.

CONTENTS

ILLUSTRATIONS

SECTION I

INTRODUCTION

It has been suggested that corona may be a significant factor in determining the voltage and current induced on an antenna by a severe electromagnetic pulse (EMP) environment. Because of the possible importance of corona effects to several on-going EMP analysis and hardening programs, a study program was undertaken. This program consisted of two parts: first, an experimental phase to measure the electric and magnetic fields of a transmission line structure with corona; second, an analytical phase to develop a simple corona model and determine the model parameters from the test data.

A wire over a ground plane was selected as the basic experimental configuration. This geometry was selected because of its compatability with existing transmission line theory and also, because the cost and fabrication problems were less severe than for an alternative configuration such as a concentric cylinder transmission line.

Section II of this report describes the transmission line facility, the high-voltage pulser used to drive the test wire and the instrumentation used to acquire the electric and magnetic field data. Test results and some basic calculations performed on the raw data are contained in Section III. A simple corona model for the transmission line over a ground plane configuration is discussed in Section IV. Preliminary conclusions and recommendations for further work are presented in Section V.

SECTION II

EXPERIMENTAL CONFIGURATION

The three basic elements of the experimental configuration are the transmission line over a ground plane test facility, the high-voltage pulser used to drive the test wire, and the field sensors and recording instrumentation. Each of these basic elements is discussed in considerable detail because of their importance to the interpretation of the test data.

1. TEST FACILITY

The test facility was constructed on the northeast corner of the Kaman property in Colorado Springs, Colorado. Relatively minor grading and filling of the natural terrain resulted in a smooth, level area suitable for placement of the 30 x 130 foot ground plane. Figures 1 and 2 are photographs of the completed test facility and Figure 3 is a sketch illustrating some physical characteristics that are not apparent from the photographs.

The vertical members of the wire support stanchions and the end support are 10 foot lengths of construction-grade 2 x 4 inch lumber set about 2 feet into the test site surface. The cross member of each stanchion is an 8 foot length of 1 x 4 inch lumber. Braided rayon cord is used to hold the test wire nearly parallel to the ground plane. This cord is attached directly to the wire and to small eyebolts fitted into the stanchion cross members and end support. An acute angle wire support geometry (i.e., the angle of the cord relative to the test wire) is not used because of the relatively low test voltage levels. However, the support structure is compatible with acute angle geometry if the need should arise in later testing.

A small corona ring (3/16 inch diameter copper tube formed into a 2¼ inch diameter ring) is attached to the test wire at

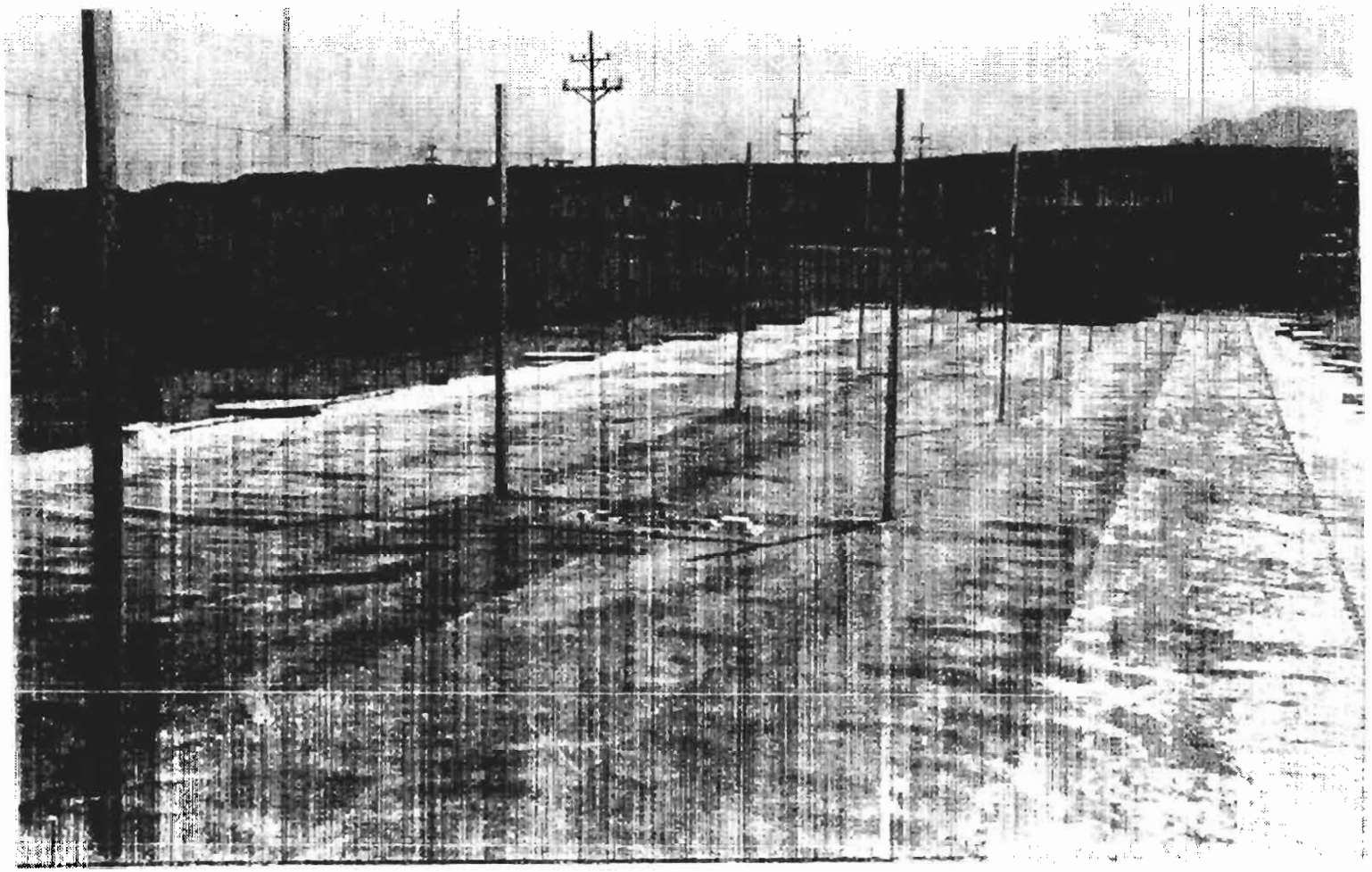

FIGURE 1

VIEW OF TEST FACILITY FROM TERMINATION END

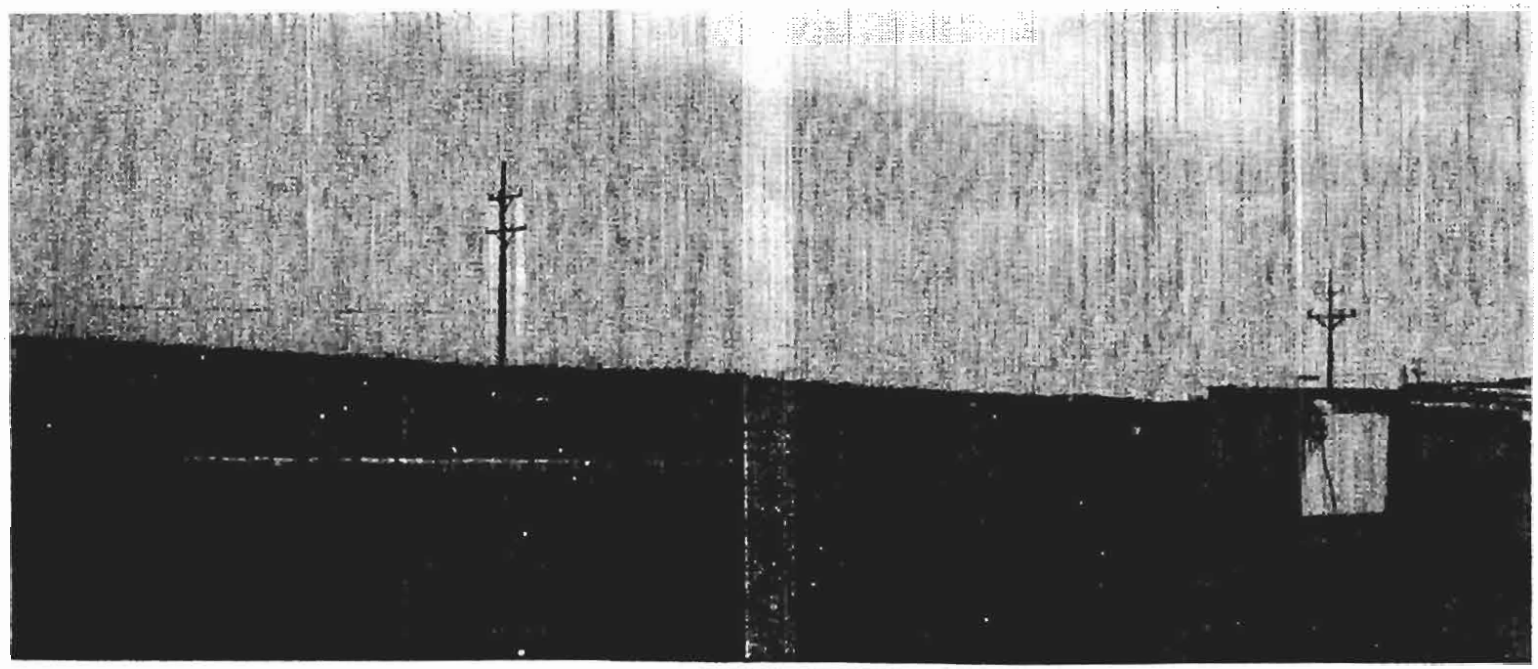

FIGURE 2
VIEW OF TEST FACILITY INCLUDING INSTRUMENTATION TRAILER

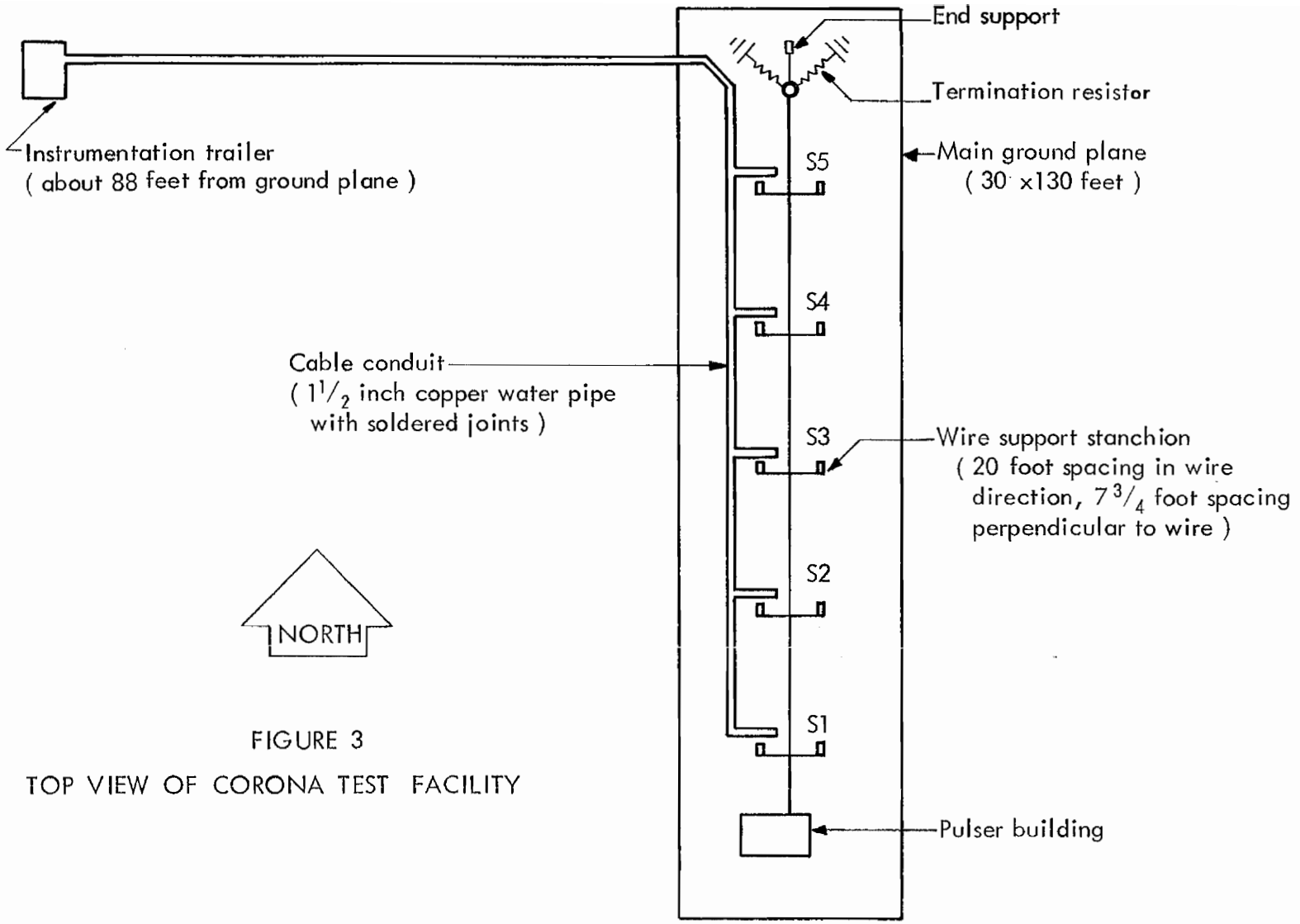

FIGURE 3

TOP VIEW OF CORONA TEST FACILITY

the termination end. Two strings of carbon composition resistors (20 2-watt, 51-ohm resistors in each string) are soldered to the corona ring and tapered down to the ground plane at approximately a 45 degree angle. The test wire is fastened to the end support with several feet of braided rayon cord running from the corona ring to a small spring scale attached directly to the end support. This scale is used to establish the proper tension for the test wire - about 2½ pounds for 20 guage copper wire.

The pulser is designed with a cap nut screwed over the primary output terminal. A small hole drilled through the cap nut provides for mechanical and electrical attachment of the test wire to the pulser output. As shown by Figure 4, this results in a very clean output configuration.

The test facility is configured for five measuring stations as indicated by the conduit outline shown in Figure 3. Solder fittings are used for all of the connections in the main part of the conduit; however, the short sections from the measuring stations are clamped into T-joints in the main conduit. All of the conduit in the ground plane region is buried about 4 inches into the test facility surface.

Cable pairs are routed from stations S1, S3 and S5 to the instrumentation trailer. In addition, jumper pairs are routed from S1 to S2 and S3 to S4 to enable measurements to be made from the intermediate stations. An RG-8/U size cable with foam dielectric was chosen because of its high propagation velocity (v_p = 0.78c) and relatively low-loss characteristics (nominal attenuation of 1.2 db/100 ft at 50 MHz and 1.8 db/100 ft at 100 MHz). Cable ends are fitted with locking type GR874 connectors at the sensors and with nonlocking type GR874 connectors at the instrumentation trailer.

Prior to placement of the ground plane, the test site surface was covered with a 0.006 inch plastic sheet to inhibit weed growth. The main ground plane consists of eight 4 x 130 foot

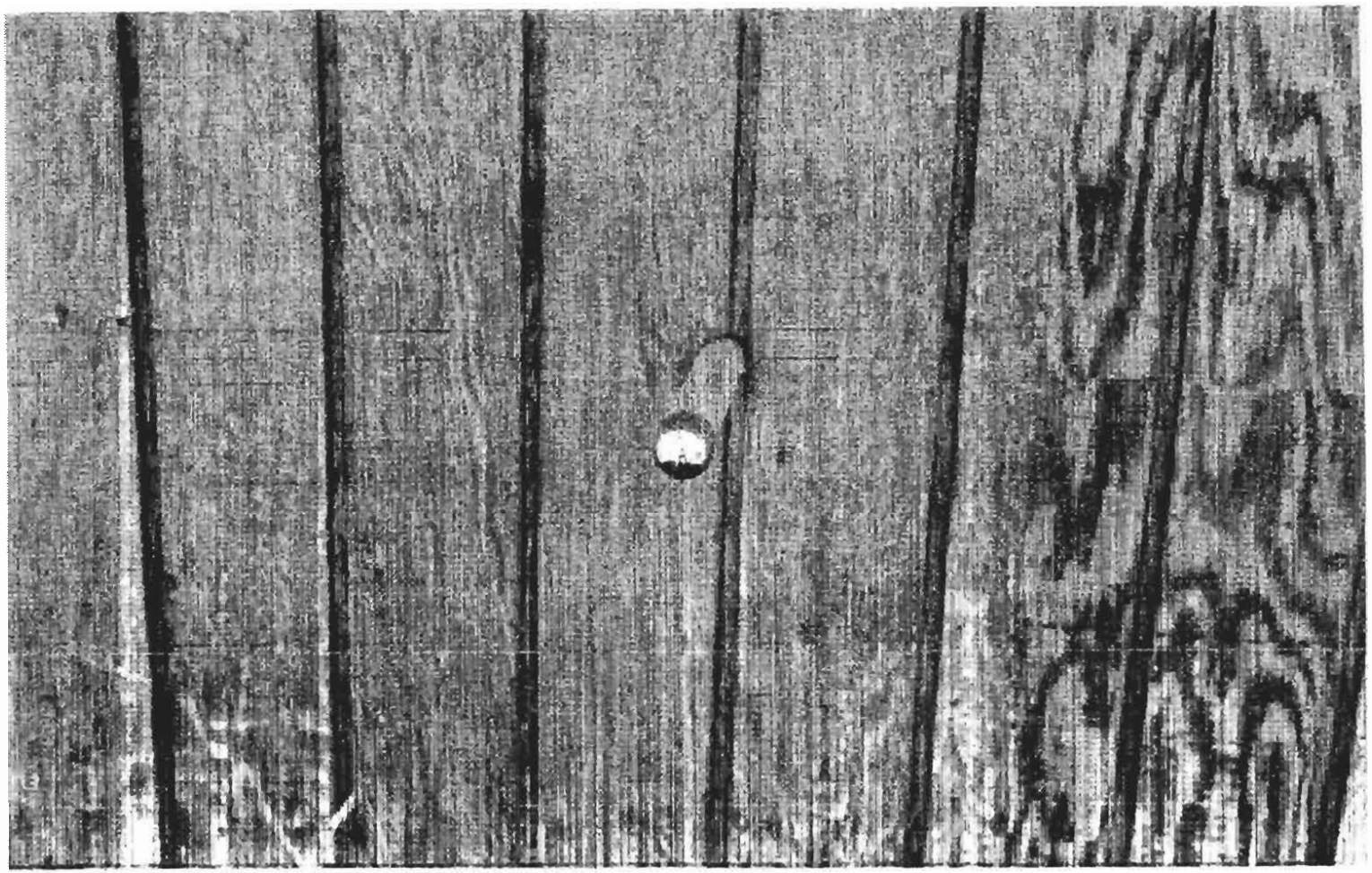

FIGURE 4

ATTACHMENT OF PULSER OUTPUT TO TEST WIRE

rolls of copper wire cloth (No. 16 mesh size, 0.017 inch wire diameter). The rolls are overlapped about 1½ inches and spot-soldered at 4 to 6 inch intervals to form an overall surface slightly wider than 30 feet.

Power for the instrumentation trailer was obtained from a commercial outlet in a Kaman manufacturing building located about 100 feet west of the trailer site. A high-quality power line filter (Lindgren Model C-30-2) is built into the trailer to prevent noise coupled onto the power cord from interfering with operation of the recording oscilloscopes.

The trailer and instrumentation are inherently grounded by the main ground plane and the buried conduit. An additional and perhaps lower impedance ground is provided by an 8 foot copper rod located near the trailer and securely clamped to the cable conduit.

2. HIGH-VOLTAGE PULSER

The high-voltage pulser used to drive the transmission line was designed and fabricated at Kaman. It essentially consists of a 120 kV charging supply (Universal Voltronics Model BPO-130-5-K3), a coaxial cable energy storage element (140 feet of RG-220/U), and a 100 kV spark gap output switch (Maxwell Laboratories Model 40065). Figure 5 is a schematic of the pulser; it shows the basic pulser components plus the charging resistor and the trigger electrode grading resistors. The schematic also indicates the approximate layout of the various components.

Figure 6 is a photograph of the finished unit as installed in the test facility pulser building. The pulser output appears in the lower, left region of the photograph; the output cable exits from the building and is terminated with the cap nut as shown in Figure 4. In accordance with normal design practice, the spark gap and grading resistors are operated in an SF_6 environment. This environment is provided by a 2 x 3 x 3 foot

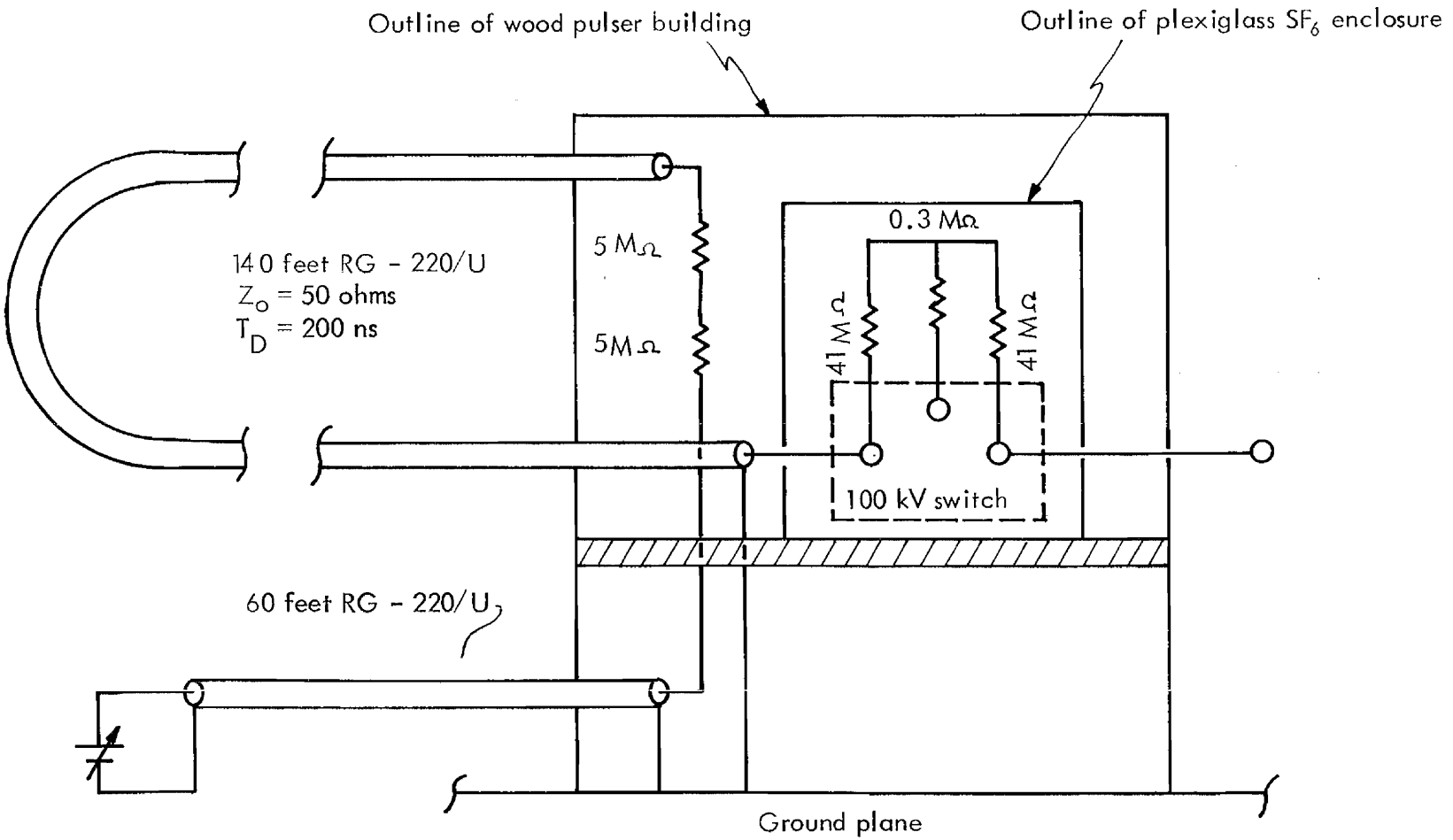

FIGURE 5

DIAGRAM OF HIGH-VOLTAGE PULSER

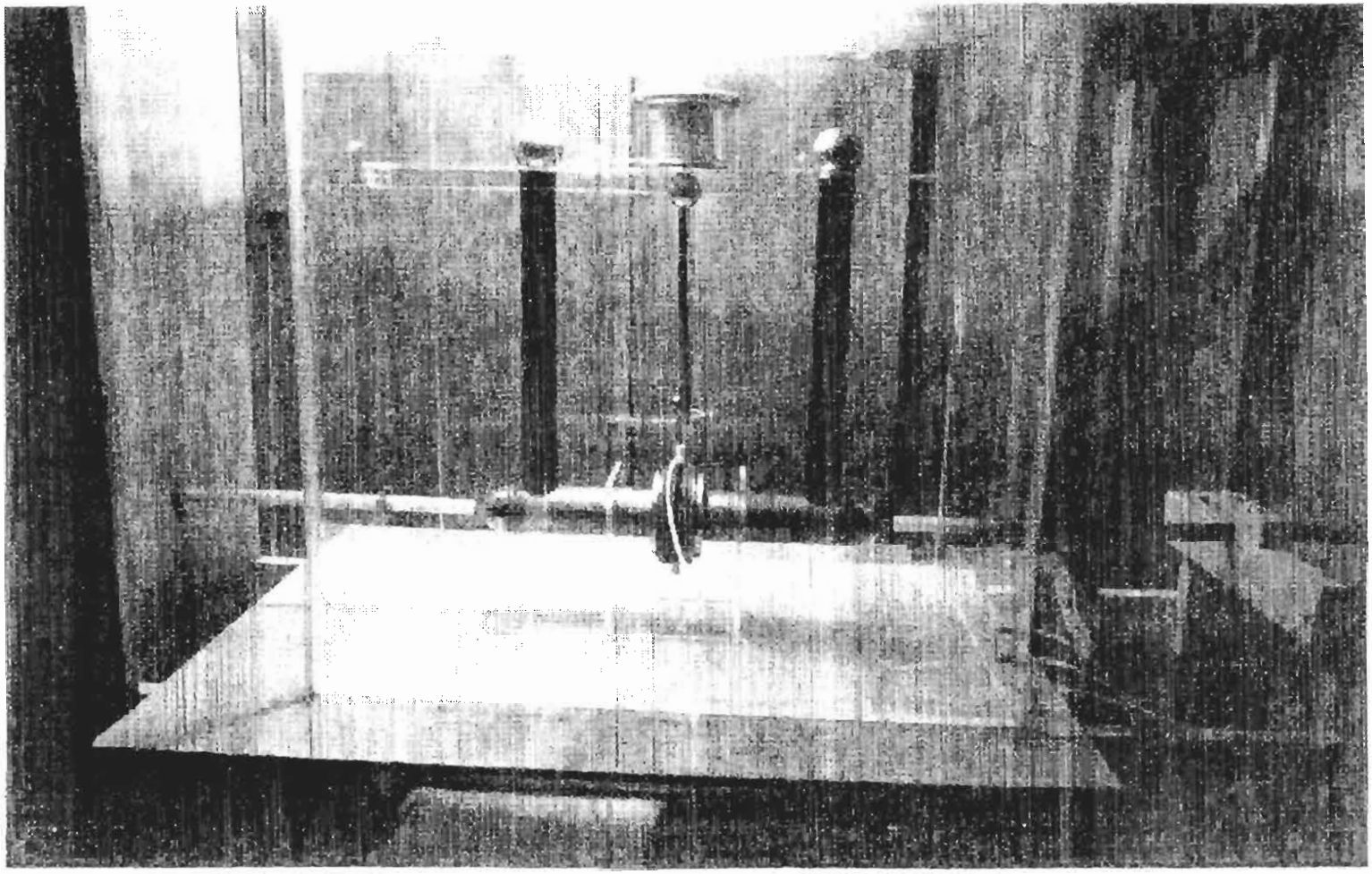

FIGURE 6

PHOTOGRAPH OF HIGH-VOLTAGE PULSER

plexiglass enclosure fabricated from 3/8 inch stock. Air feed and vent lines for the spark gap and the SF_6 feed line to the enclosure are shown in the lower, right region of the photograph. It should be noted that the SF_6 enclosure is mounted on two horizontal 2 x 4s. The purpose of this design feature is to match the pulser height to the line height and thereby maintain a low-inductance configuration.

A second spark gap is apparent in the center, upper region of Figure 6. This gap was included in the initial design to provide a low-jitter trigger capability. However, this capability was not developed because creating a rapid decrease in the gap air pressure proved to be an effective triggering method. This air pressure decrease was effected by manual control of a valve on the air vent line. In addition to its simplicity, the pressure relief triggering method has a further advantage in that there is no precursor pulse.

The pulser was characterized by operation into a load impedance comparable to the 500-ohm characteristic impedance of the transmission line test facility. Measurements were made with a 500-ohm copper sulfate resistor (2¼ inch diameter x 23 inch length) and a 500-ohm carbon composition resistor configuration (two parallel strings with 10 2-watt, 100-ohm units in each string). In each case, the Stoddart Model 93686-3 current probe was located on the ground plane to minimize the effects due to the parasitic capacitance between the current probe and the pulser output lead. The current waveforms were recorded with the same oscilloscope as was used for primary data acquisition. Figures 7 and 8 show the current waveforms for various negative and positive operating levels. These photographs are for the carbon composition resistor, but other photographs with the copper sulfate resistor showed virtually the same waveform.

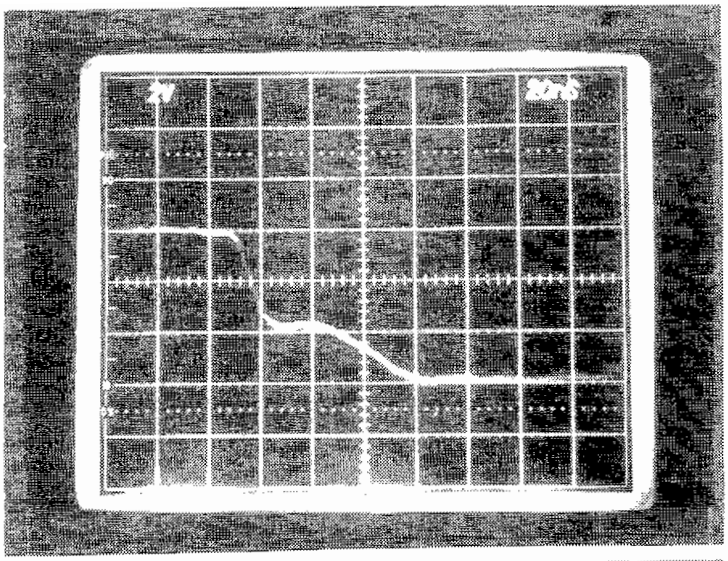

V_P = - 30 kV

S_V = 20 A/cm

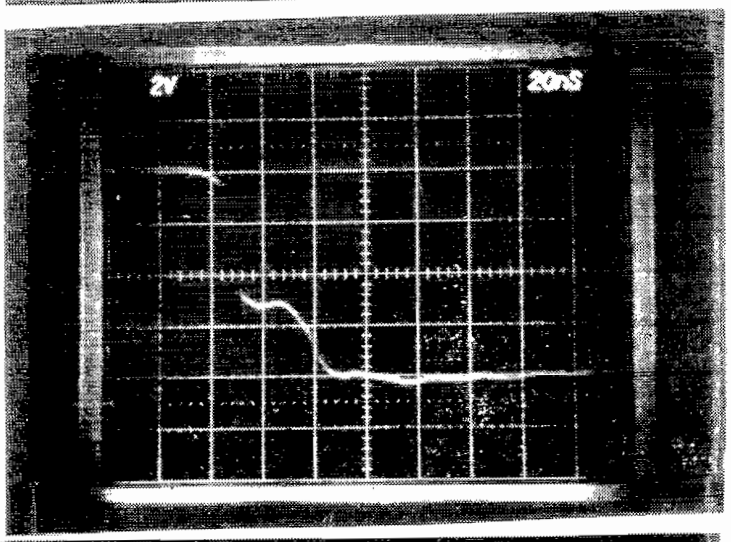

V_P = - 40 kV

S_V = 20 A/cm

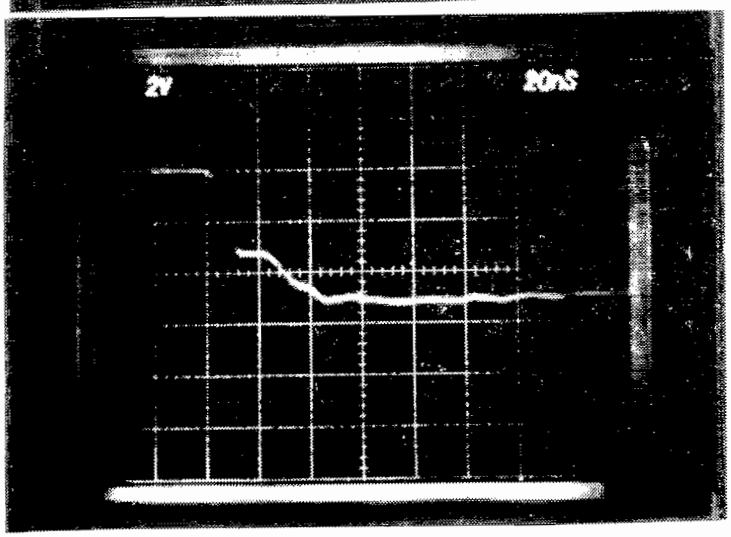

V_P = - 50 kV

S_V = 40 A/cm

FIGURE 7

PULSER OUTPUT FOR NEGATIVE VOLTAGES

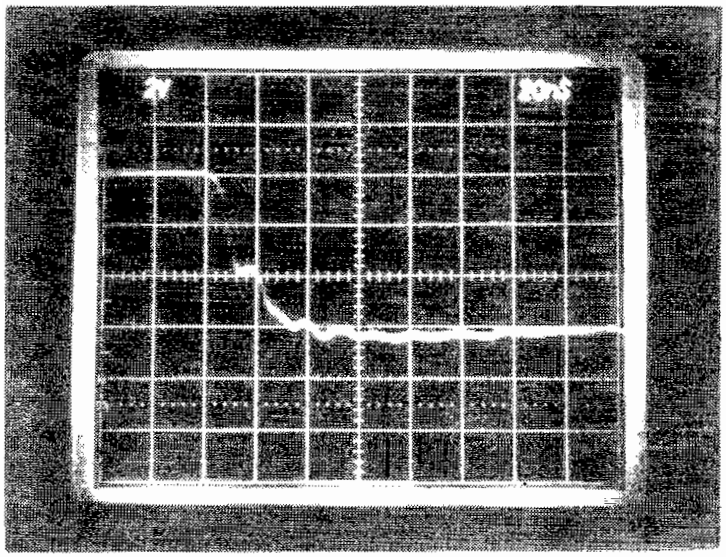

V_P = - 60 kV

S_V = 40 A/cm

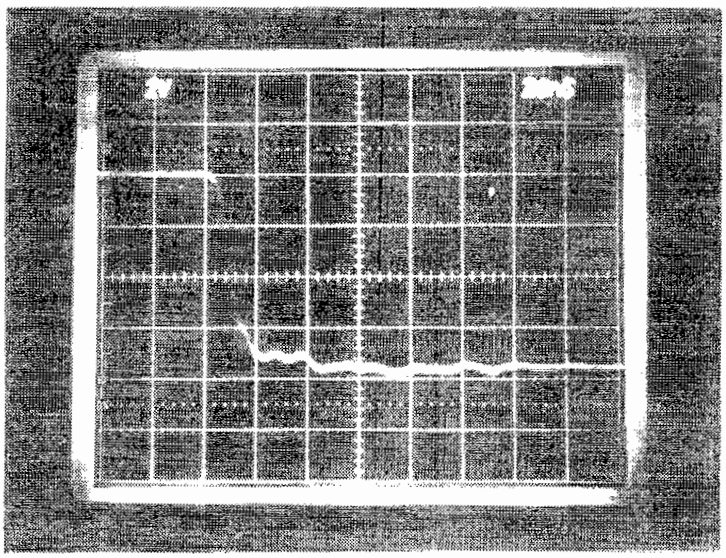

V_P = -70 kV

S_V = 40 A/cm

FIGURE 7 (Continued)
PULSER OUTPUT FOR NEGATIVE VOLTAGES

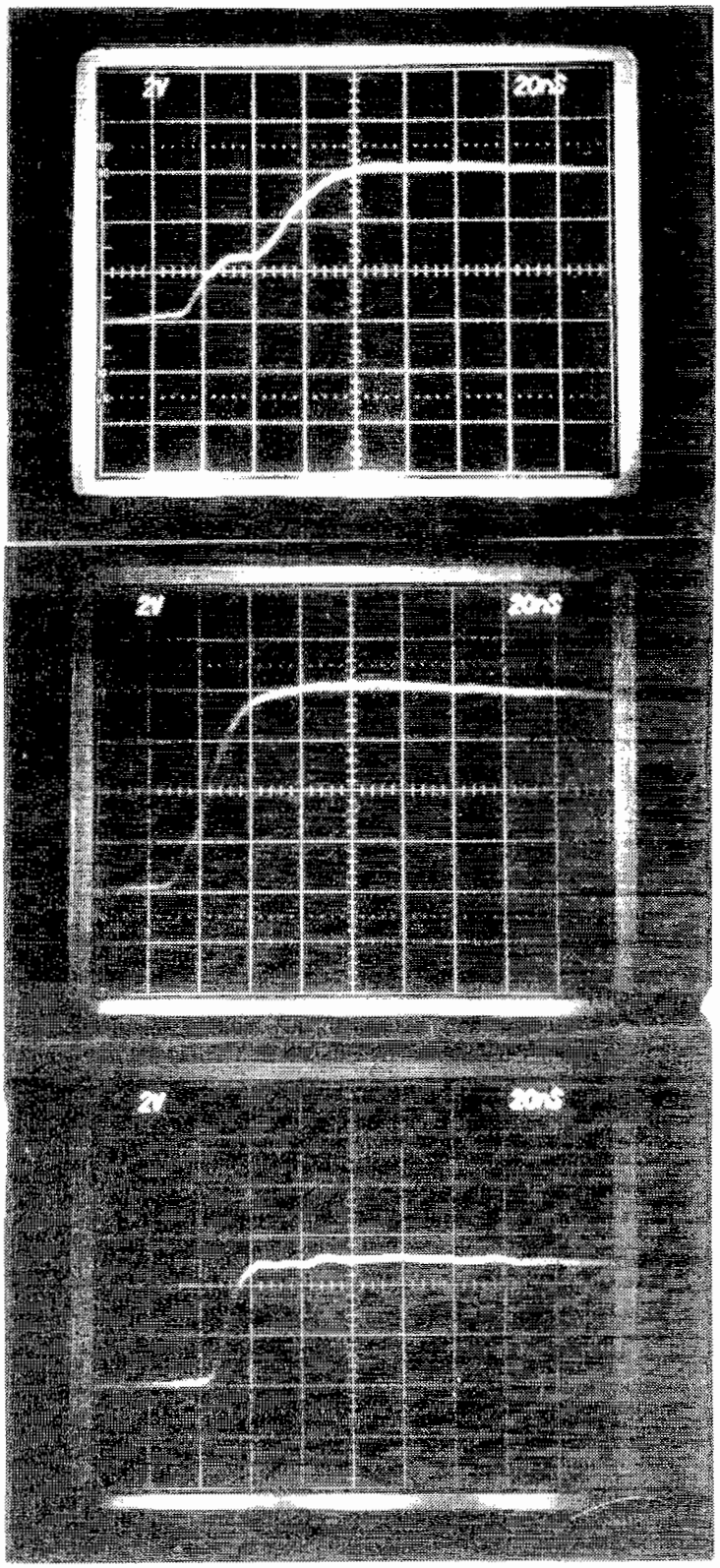

V_P = 30 kV

S_V = 20 A/cm

V_P = 40 kV

S_V = 20 A/cm

V_P = 50 kV

S_V = 40 A/cm

FIGURE 8

PULSER OUTPUT FOR POSITIVE VOLTAGES

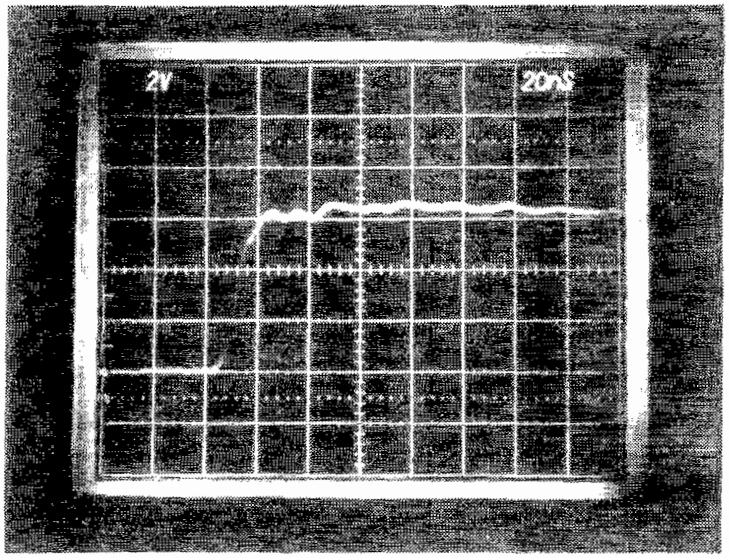

V_P = 60 kV

S_V = 40 A/cm

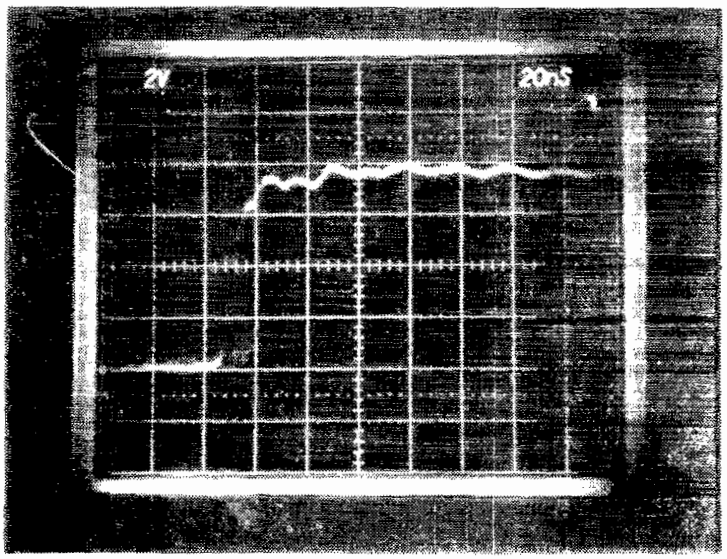

V_P = 70 kV

S_V = 40 A/cm

FIGURE 8 (Continued)
PULSER OUTPUT FOR POSITIVE VOLTAGES

The voltage levels referred to throughout this report are the levels on the charged coaxial cable. Since the RG-220/U cable has a 50-ohm characteristic impedance and the load impedance is 500 ohms, the peak line voltage is given by

$$V_L = \frac{R_L}{R_L + Z_o} V_P$$

$$V_L = 0.91\ V_p$$

The expected peak load current is simply

$$I_L = \frac{V_L}{R_L} = \frac{V_P}{R_L + Z_o} = \frac{V_P}{550}$$

$$I_L = 1.82\ V_P$$

where I_L is in amperes and V_P is in kV. A cursory examination of Figures 7 and 8 shows that the current levels are somewhat higher than expected. This probably indicates that the actual high-voltage level is a few percent greater than the recorded level since the current measurement is inherently more accurate than the voltage measurement.

A pulser characteristic of considerable importance in the interpretation of the test facility data is the decrease in current risetime at higher operating voltages. This is about as expected since the low voltage, high impedance operating condition represents an extremely light load for the model 40065 spark gap. Another characteristic of importance is the distinctive shoulder on the leading edge of the current waveform - particularly in the 30 to 40 kV operating region. Again, this is not too surprising since the 30 to 40 kV region is the lower end of the recommended operating range for the

spark gap. Figure 9 is a comparison of pulse-to-pulse repeatability for two typical operating levels; very good pulse-to-pulse repeatability is apparent at 50 kV in contrast to the significant variations evident at 40 kV.

3. INSTRUMENTATION

The signal measuring instrumentation consisted of Tektronix type 7704A oscilloscopes with standard P31 phosphor, type 7A16A amplifiers and type 7B50 or 7B53A time base units. The specified bandwidth for this combination of equipment is 160 MHz. Each oscilloscope was equipped with a Tektronix type C50R camera. Based on specifications given in the supplier's product catalog, the expected photographic writing speed is about 1 cm/ns for the combination of P31 phosphor and C50R camera with Polaroid type 410 film (ASA 10,000).

Six complete oscilloscope/camera systems were assembled in the instrumentation trailer which was located about 90 feet west of the ground plane as shown in Figures 2 and 3. Figures 10 and 11 are close-up views of the trailer interior and exterior, respectively. One feature that should be noted in the interior view is the presence of a screen enclosure (shown with door open) for the oscilloscopes. Important features visible in the exterior view include the copper braid running from the end of the copper pipe to an entry port of the interior screen room, the power line filter just beneath the waterproof cover, and the equivalent-dipole antenna extending above the trailer.

A signal from the dipole antenna noted in the preceding paragraph was used to generate a trigger for the recording oscilloscopes. The output of the dipole antenna was fed into the "External Trigger" input of a Tektronix type 485 oscilloscope in the instrumentation trailer. The "A Gate" output of the type 485 oscilloscope was used to trigger a special pulse generator which provided a high-level (~ 20 V), short-duration (~ 10 ns) pulse to drive the "External Trigger" inputs of all

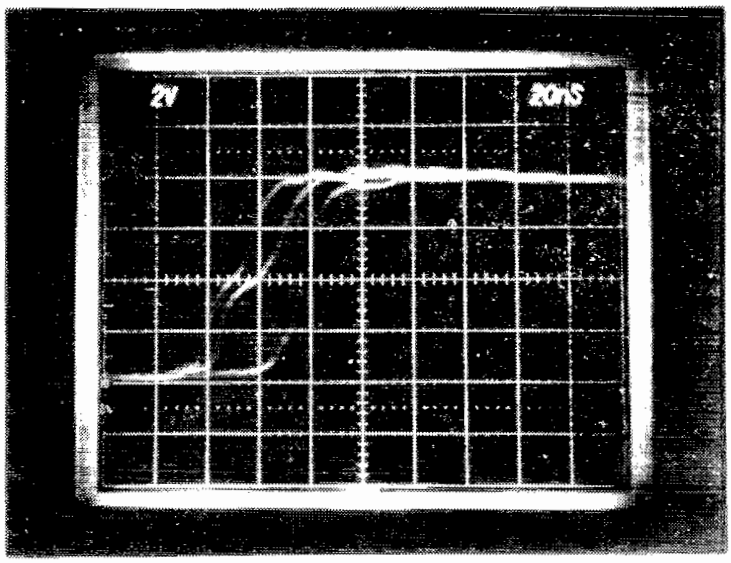

V_P = 40 kV

S_V = 20 A/cm

3 Pulses

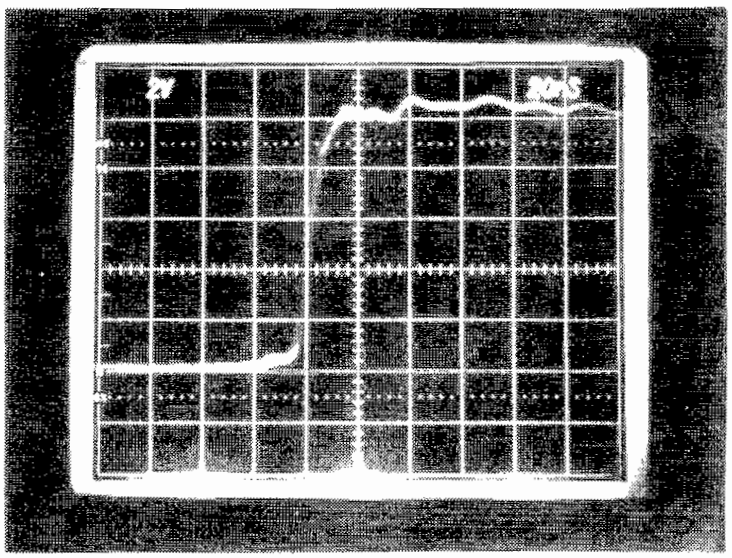

V_P = 50 kV

S_V = 20 A/cm

3 Pulses

FIGURE 9

PULSER OUTPUT FOR SUCCESSIVE PULSES

FIGURE 10
INTERIOR VIEW OF INSTRUMENTATION TRAILER

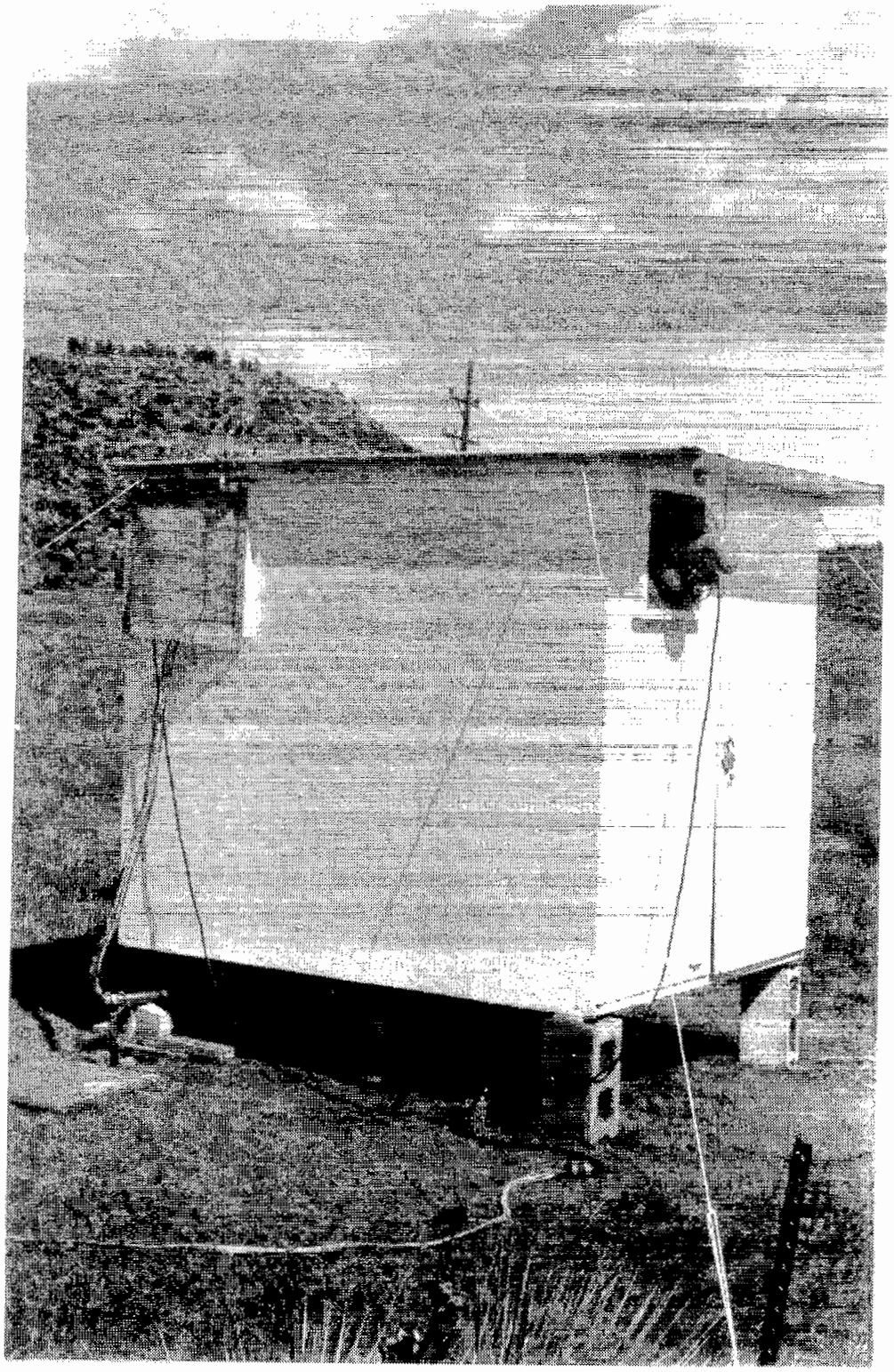

FIGURE 11
EXTERIOR VIEW OF INSTRUMENTATION TRAILER

of the type 7704A recording oscilloscopes. This triggering method enabled the leading edges of the sensor signals to be recorded with no difficulty because of the propagation times of these signals relative to the trigger signal.

A reference signal from a pulse generator was used to check the overall response of the recording instrumentation and the test facility cabling. Figure 12a shows the signal recorded on one of the type 7704A oscilloscopes with the pulse generator located in the instrumentation trailer. Figure 12b shows the same signal with the pulse generator located on the ground plane at station one (that is, after propagation through about 210 feet of the low-loss coaxial cable). As expected, the cable response is characterized by a rapid-rise phase followed by a slow approach to the final level. Since many of the signals of interest are in the 5 to 15 nanosecond regime, it is clear that the measurements will be somewhat low. However, this is not too severe a limitation if the analyses and modeling efforts are based primarily on relative signal levels.

Model MGL-S5A(A) $\dot{B}$ sensors and model HSD-S3A(R) $\dot{D}$ sensors were selected to measure the magnetic and electric fields at the ground plane. These types were chosen because of availability, a comparatively small size compatible with a transmission line height from 0.5 to 1 meter, and sufficient sensitivity to generate a measurable signal for the lowest expected operating voltage. Also, the risetime capability of less than 1 nanosecond for both types is considerably better than required.

As shown in Figure 13, each sensor is bolted to a copper sheet which is soldered to the ground plane. The transmission wire is located directly over the seam indicated in the center of the photograph (see Figure 1 for an overall view of the sensor locations). A 34 inch spacing between sensors was chosen to avoid mutual interference. Copper braid is used to shield the cable section between the sensor outputs and cable conduit located just below the ground plane. Each braid is clamped to

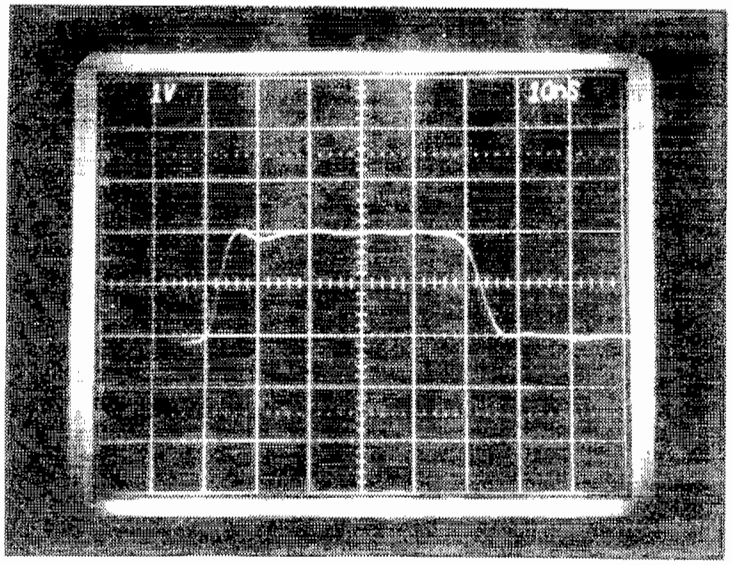

FIGURE 12a

RESPONSE WITH PULSE GENERATOR IN TRAILER

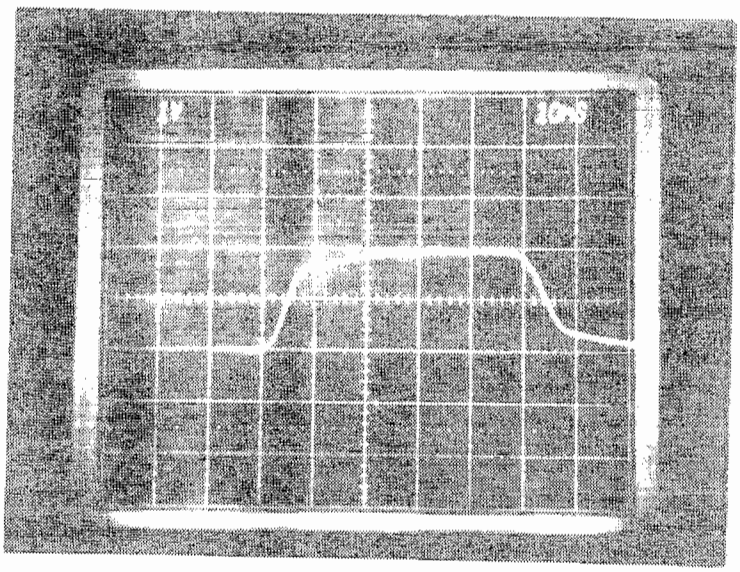

FIGURE 12b

RESPONSE WITH PULSE GENERATOR AT STATION ONE

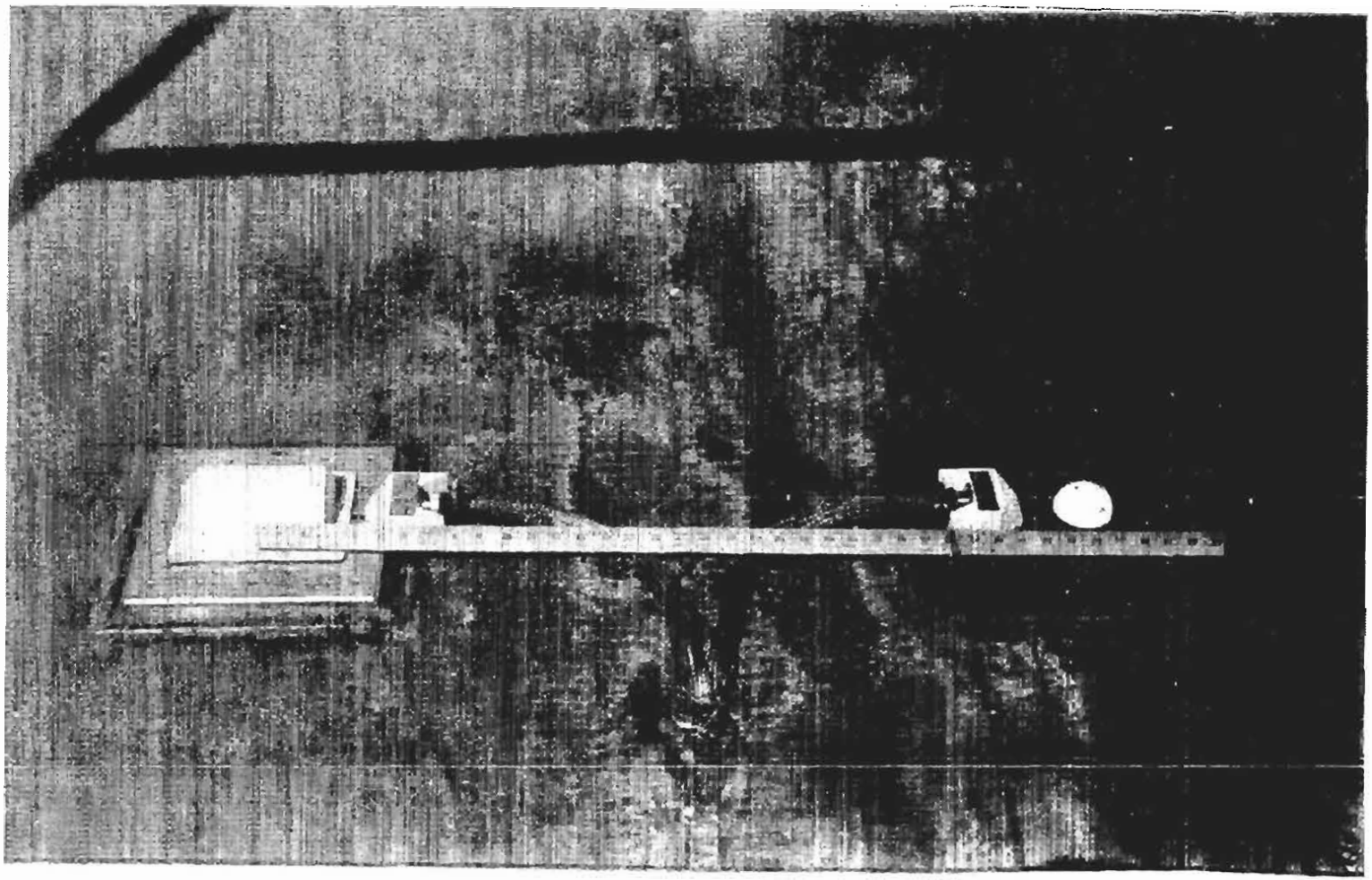

FIGURE 13

MOUNTING CONFIGURATION FOR MAGNETIC AND
ELECTRIC FIELD SENSORS

the connector shell on the sensor; it is spot-soldered to the ground plane at several places and soldered around the entire periphery where it feeds through the ground plane.

The pertinent equations for the sensors are

$$V_{\dot{B}} = A_{eq} \frac{dB}{dt} \cos\theta$$

where $A_{eq} = 10^{-3}$ m^2 = sensor equivalent area

$\cos\theta = 1$

B = magnetic flux density in webers/m^2

and $$V_{\dot{D}} = R\, A_{eq} \frac{dD}{dt}$$

where $A_{eq} = 10^{-2}$ m^2 = sensor equivalent area

R = 50 ohms = load resistance

D = electric displacement or electric flux density in coul/m^2

RCI-1C type integrators were used to electrically integrate the sensor outputs. The time constant for this type of integrator is 1 microsecond.

SECTION III

TEST RESULTS

Appendix A is a compilation of data for an operating voltage range from ± 30 kV to ± 80 kV. These data were taken with 0.8114 millimeter diameter (A.W.G. No. 20) copper wire positioned at 1 meter above the ground plane and the pulser configuration described in the preceding section. Other data taken earlier in the test program may be slightly different from the data presented in this report because of minor changes made to the test facility and/or the high-voltage pulser.

The atmospheric conditions were not recorded at the time the experiment was performed. However, Table 1 is a summary obtained from NOAA records for the Peterson Field measuring station in Colorado Springs, Colorado. The last column in Table 1 was calculated from the ideal gas law using a correction factor to account for the moisture content of the air (ref. 1). The test data presented in this report were acquired during the time period covered by Table 1, but a specific time cannot be assigned to each set of data.

The data given in Appendix A were taken on the basis of one station per excitation pulse. That is, $\dot{B}$ and $\dot{D}$ or B and D at a particular station pertain to the same excitation pulse but $\dot{B}$ for station 3 is for a different pulse than $\dot{B}$ for station 1. Similarly, $\dot{B}$ and B at a particular station are for different pulses. As indicated by the current waveforms given in Section II, the pulse-to-pulse variation is significant at 30 to 40 kV which represents the lower end of the operating range for the 100 kV spark gap switch.

---

[1] Weast, R. C., Handbook of Chemistry and Physics, The Chemical Rubber Company, Cleveland, Ohio, 1968.

TABLE 1

LOCAL ATMOSPHERIC CONDITIONS

DATE	TIME	TEMP (°F)	RELATIVE HUMIDITY (Percent)	DEW POINT (°F)	ABSOLUTE BAROMETRIC PRESSURE* (Inches of Hg)	AIR DENSITY (g/l)
10 Sept 1976	0800	57	64	45	24.175	0.989
	0900	60	60	46	24.165	0.983
	1000	67	52	49	24.150	0.968
	1100	69	53	51	24.125	0.964
	1200	72	44	49	24.100	0.958
	1300	75	37	47	24.080	0.952
	1400	75	37	47	24.055	0.951
	1500	74	40	48	24.050	0.952
	1600	75	38	48	24.030	0.950
	1700	75	38	48	24.025	0.950
13 Sept 1976	0800	60	62	47	24.155	0.983
	0900	62	60	48	24.165	0.984
	1000	65	54	48	24.175	0.979
	1100	67	51	48	24.165	0.969
	1200	68	49	48	24.155	0.967
	1300	71	43	47	24.150	0.962
	1400	70	44	47	24.150	0.964
	1500	71	44	48	24.140	0.962
	1600	69	44	46	24.130	0.970
	1700	68	44	45	24.130	0.972
14 Sept 1976	0800	55	86	51	24.165	0.992
	0900	59	81	53	24.165	0.990
	1000	64	70	54	24.160	0.980
	1100	67	63	54	24.140	0.967
	1200	70	57	54	24.115	0.961
	1300	71	51	52	24.080	0.958
	1400	69	55	52	24.090	0.962
	1500	68	36	40	24.090	0.966
	1600	71	39	45	24.065	0.959
	1700	64	56	48	24.105	0.973

* The reference altitude for these data is 6092 feet.

TABLE 1 (Continued)

LOCAL ATMOSPHERIC CONDITIONS

DATE	TIME	TEMP (°F)	RELATIVE HUMIDITY (Percent)	DEW POINT (°F)	ABSOLUTE BAROMETRIC PRESSURE (Inches of Hg)	AIR DENSITY (g/l)
15	0800	64	58	49	24.090	0.972
Sept	0900	67	50	48	24.100	0.967
1976	1000	69	45	47	24.100	0.963
	1100	72	44	49	24.090	0.957
	1200	66	63	53	24.080	0.967
	1300	69	55	52	24.065	0.961
	1400	69	55	52	24.050	0.960
	1500	70	51	51	24.050	0.959
	1600	67	49	47	24.060	0.965
	1700	65	52	47	24.065	0.970
16	0800	54	80	48	24.150	0.994
Sept	0900	57	75	49	24.140	0.987
1976	1000	58	72	49	24.140	0.985
	1100	62	65	50	24.130	0.977
	1200	65	61	51	24.110	0.971
	1300	68	55	51	24.090	0.964
	1400	69	53	51	24.080	0.962
	1500	68	55	51	24.055	0.963
	1600	69	57	53	24.080	0.961
	1700	69	57	53	24.080	0.961
17	0800	59	81	53	24.080	0.980
Sept	0900	63	70	53	24.080	0.973
1976	1000	68	59	53	24.075	0.963
	1100	74	41	49	24.055	0.952
	1200	77	32	45	24.040	0.947
	1300	80	25	41	24.015	0.944
	1400	78	28	42	24.010	0.945
	1500	79	26	41	24.000	0.943
	1600	74	33	43	24.000	0.951
	1700	70	47	49	24.000	0.957

Several basic calculations can be performed on the raw data to gain further insight into the transmission line response as a function of the pulser voltage. First of all, it is useful to summarize the relationships between the measured voltages and field quantities. For the MGL-S5A(A) $\dot{B}$ sensor, the output voltage is given by

$$V_{\dot{B}} = A_{eq}\, \dot{B} \cos\theta$$

and since $A_{eq} = 10^{-3}\ m^2$ and $\cos\theta = 1$

$$\dot{B} = 10^{3}\, V_{\dot{B}}$$

For the HSD-S3A(R) $\dot{D}$ sensor, the output voltage is given by

$$V_{\dot{D}} = R\, A_{eq}\, \dot{D}$$

and since R = 50 ohms and $A_{eq} = 10^{-2}\ m^2$,

$$\dot{D} = 2V_{\dot{D}}$$

RCI-1C integrators were used to electrically integrate the derivative signals. For time intervals that are small compared to the RC time constant of the integrator, the expected output is

$$V_B = \frac{1}{C}\int i\,dt = \frac{1}{C}\int \frac{V_{\dot{B}}}{R}\,dt$$

$$= \frac{1}{RC}\int 10^{-3}\ dB$$

$$= \frac{10^{-3}\ B}{RC}$$

Since $RC = 10^{-6}$ seconds for the RCI-1C type integrator,

$$B = 10^{-3}\, V_B$$

A similar manipulation of $V_{\dot{D}}$ yields

$$D = 0.2 \times 10^{-5} V_D$$

The normal mode of propagation for the transmission line over a ground plane test configuration is TEM. For this mode of propagation, the ratio of E/H is simply the characteristic impedance of free space, Z_o. One reasonable test on the data is to calculate Z at the ground plane to determine at what pulser level the impedance deviates significantly from Z_o. The impedance can be calculated from the integral data in a very straightforward manner:

$$Z = \frac{E}{H} = \frac{D/\varepsilon_o}{B/\mu_o} = Z_o^2 \frac{D}{B}$$

$$= \frac{Z_o^2}{500} \frac{V_D}{V_B}$$

$$= 284 \frac{V_D}{V_B}$$

Table 2 is a tabulation and Figures 14 through 19 are graphs of the calculated impedance at each of the three measuring stations.

One of the primary error sources in the foregoing impedance calculation is in the determination of t_o for the recorded B and D waveforms. This limitation can be circumvented if the calculation is based on the peak $\dot{B}$ and $\dot{D}$ waveforms. For very early times or for pulser voltages less than the corona threshold, the appropriate relationship is

$$Z = Z_o^2 \frac{\dot{D}}{\dot{B}}$$

$$= 284 \frac{V_{\dot{D}}}{V_{\dot{B}}}$$

Table 3 shows the impedance values calculated from the above expression.

TABLE 2
IMPEDANCE VALUES CALCULATED FROM INTEGRAL DATA

PULSER VOLTAGE (kV)	TIME (ns)	V_{B1} (mV)	V_{D1} (mV)	Z1 (ohms)	V_{B3} (mV)	V_{D3} (mV)	Z3 (ohms)	V_{B5} (mV)	V_{D5} (mV)	Z5 (ohms)
-30	20	10.5	15	406	10	14	397	10	15	428
	40	11	15.5	400	12	16	378	11	16	414
	60	13.5	19	400	14	20.5	416	14	20	406
	80	14.5	21	411	14.5	21	411	15	21	397
	100	15	21	397	14	21	426	14.5	21	426
	120	15	21	397	13.5	20.5	431	14	21	411
-40	20	15	21	397	16	22	390	15.5	23	421
	40	20	29	412	17	25	418	15.5	23	421
	60	22	34	438	19	30	448	17	25	403
	80	23	38	470	20	34	482	19	31	464
	100	23	38	470	20	36	512	20	35	497
	120	23	39	482	21	38	515	20	40	568
-60	20	28	40	406	19	28	418	17.5	25	406
	40	33	54	464	27.5	42	434	20	29	412
	60	35	60	487	31.5	52	469	29	45	435
	80	35	61	495	32.5	56	490	31	57	512
	100	35	61	495	32.5	57	498	31	61	559
	120	34	61	495	32	57	506	31	62	558
	140	34	61	495	32	57	506	31	63	578
-80	20	36	52	410	22	30	387	18.5	29	446
	40	45	73	462	38	62	464	31	49	449
	60	47	79	478	42	71	481	39	69	502
	80	47	80	484	44	76	491	41	78	541
	100	47	82	496	43	77	508	41	82	568
	120	47	82	496	43	77	508	41	84	582
+30	20	7.5	11	416	6.5	9	394	11	14.5	374
	40	12.5	17.5	398	12	16	379	14	18.5	375
	60	15	21	398	14	19.5	396	15	21	397
	80	15	21.5	407	15	20.5	388	15	21	397
	100	15	21.5	407	15	20.5	388	15	21	397
	120	15	21.5	407	15	20.5	388	15	21	397

TABLE 2 (Continued)
IMPEDANCE VALUES CALCULATED FROM INTEGRAL DATA

PULSER VOLTAGE (kV)	TIME (ns)	V_{B1} (mV)	V_{D1} (mV)	Z1 (ohms)	V_{B3} (mV)	V_{D3} (mV)	Z3 (ohms)	V_{B5} (mV)	V_{D5} (mV)	Z5 (ohms)
+40	20	17	23	384	17	23	384	15.5	22	403
	40	19	29	434	17	26	434	16.5	23	396
	60	20	32	454	17.5	26	422	17	26	434
	80	21.5	37	489	18.5	29	446	17	27	452
	100	22.5	38	479	19	31	463	17	27	452
	120	23	41	507	20	32	454	17	28	468
+60	20	27	40	421	21	32	433	17	26	434
	40	31	49	449	23.5	38	459	18.5	30	461
	60	35	58	471	27.5	48	496	23	38	469
	80	36	62	489	30	48	549	26	50	547
	100	36	66	521	31	62	568	28.5	58	578
	120	36	67	528	32	64	568	29.5	63	606
	140							29.5	67	645
+80	20	40	62	440	23	35	432	19	31	463
(Set 1)	40	46	80	494	35.5	58	464	23	38	469
	60	50	88	500	42	74	500	33	53	456
	80	51	94	523	44	84	542	38	70	524
	100	52	96	524	46.5	88	537	41	83	576
	120	52	98	536	48	90	533	41	91	631
	140							41.5	98	671
+80	50	48	52	485	40	70	497	29	47	461
(Set 2)	100	52	96	524	46.5	88	538	41	83	575
	150	50	105	596	46	95	586	42	98	663
	200	49	105	608	44	105	677	41	107	741
	380	34	90	752	34	94	760	32	97	860

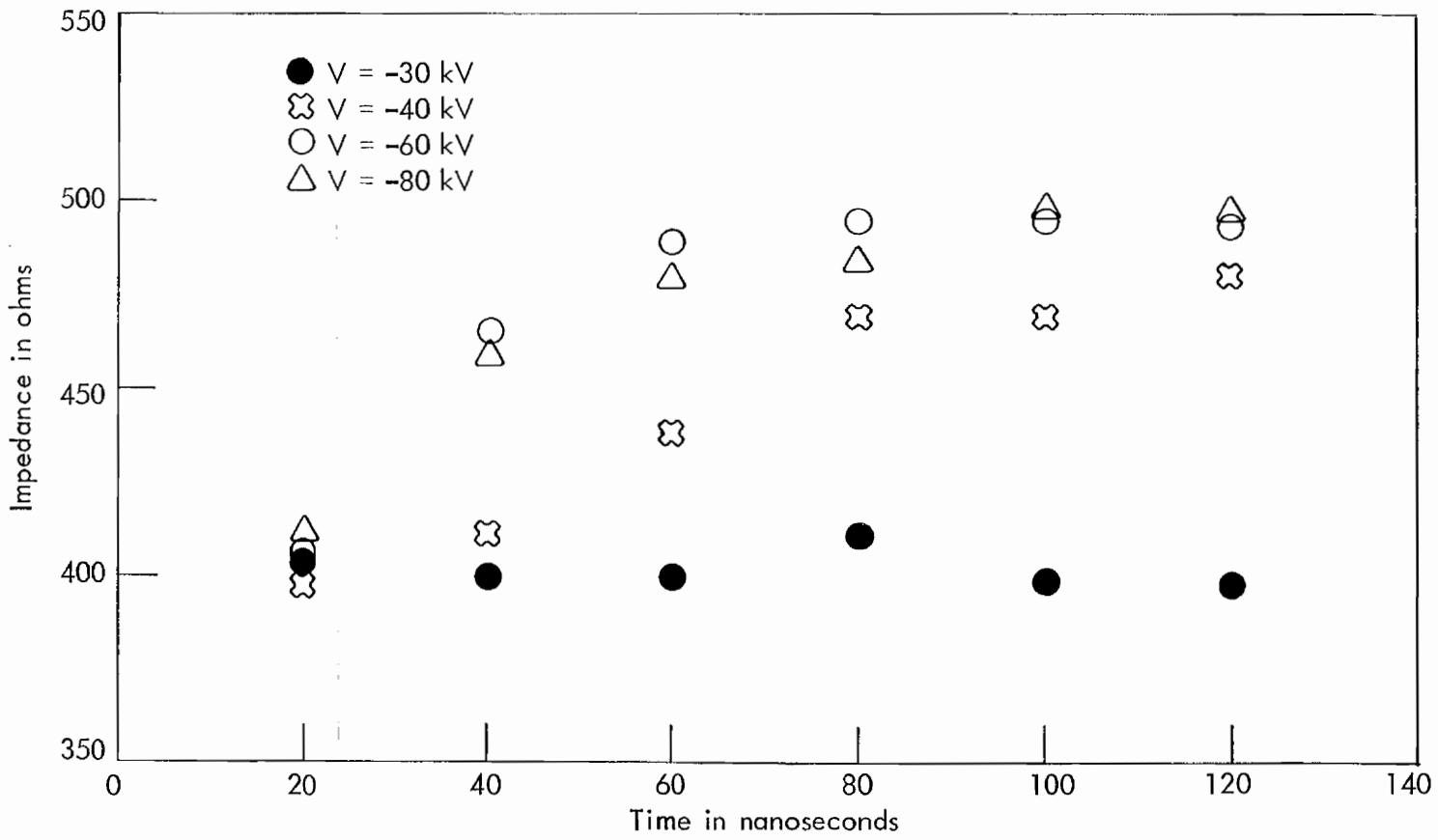

FIGURE 14

IMPEDANCE AS A FUNCTION OF TIME -STATION 1

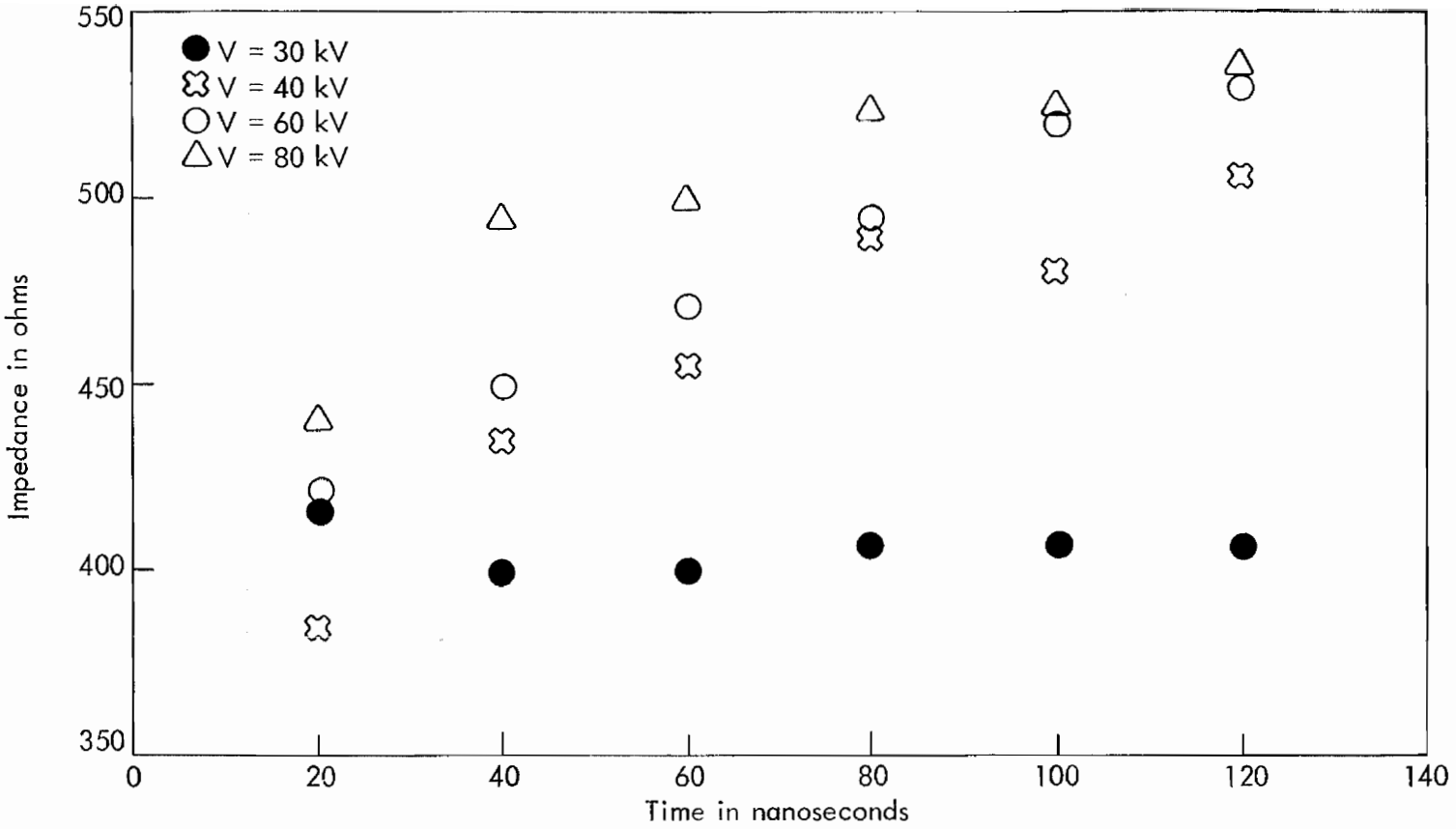

FIGURE 15

IMPEDANCE AS A FUNCTION OF TIME -STATION 1

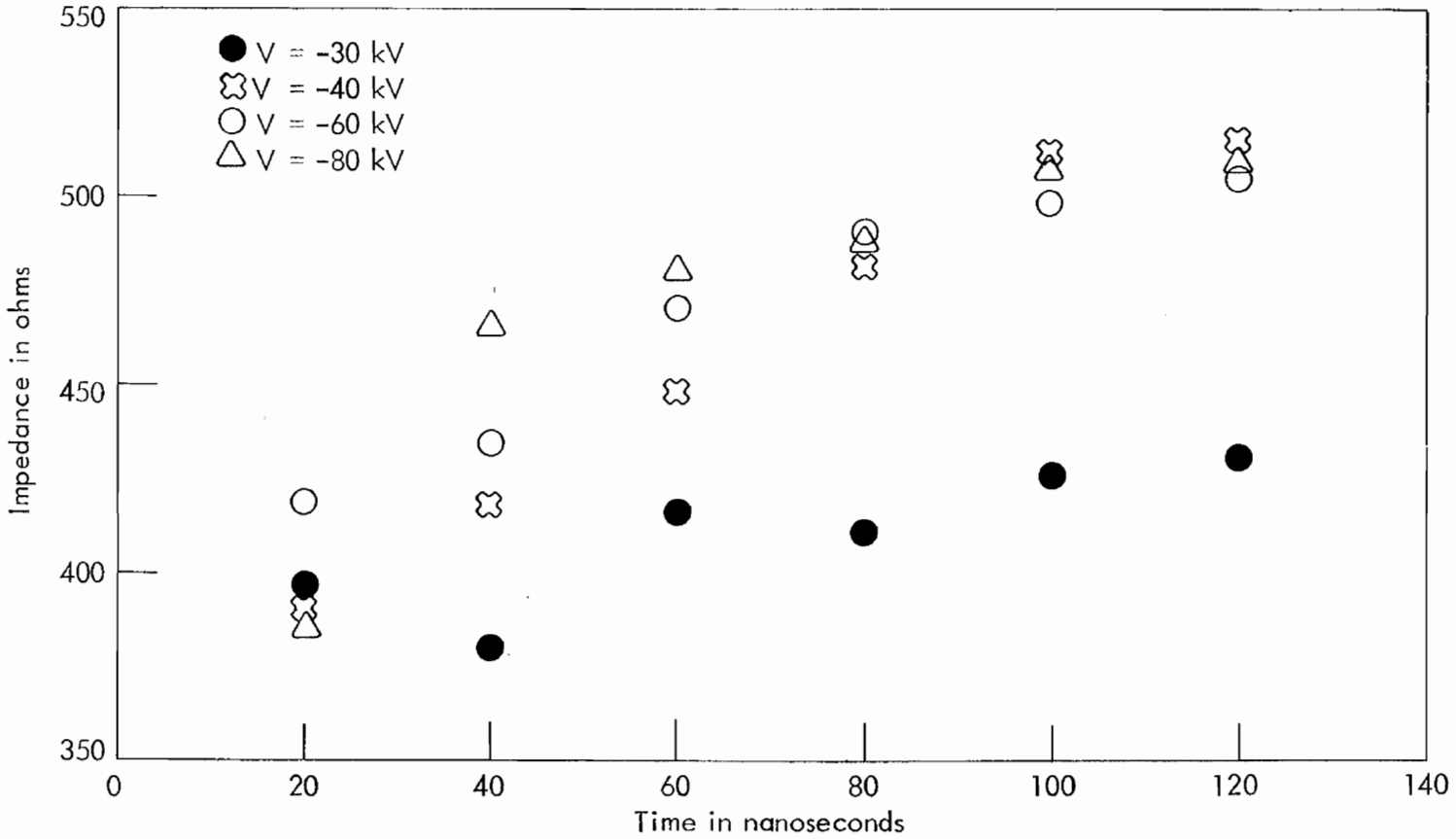

FIGURE 16

IMPEDANCE AS A FUNCTION OF TIME -STATION 3

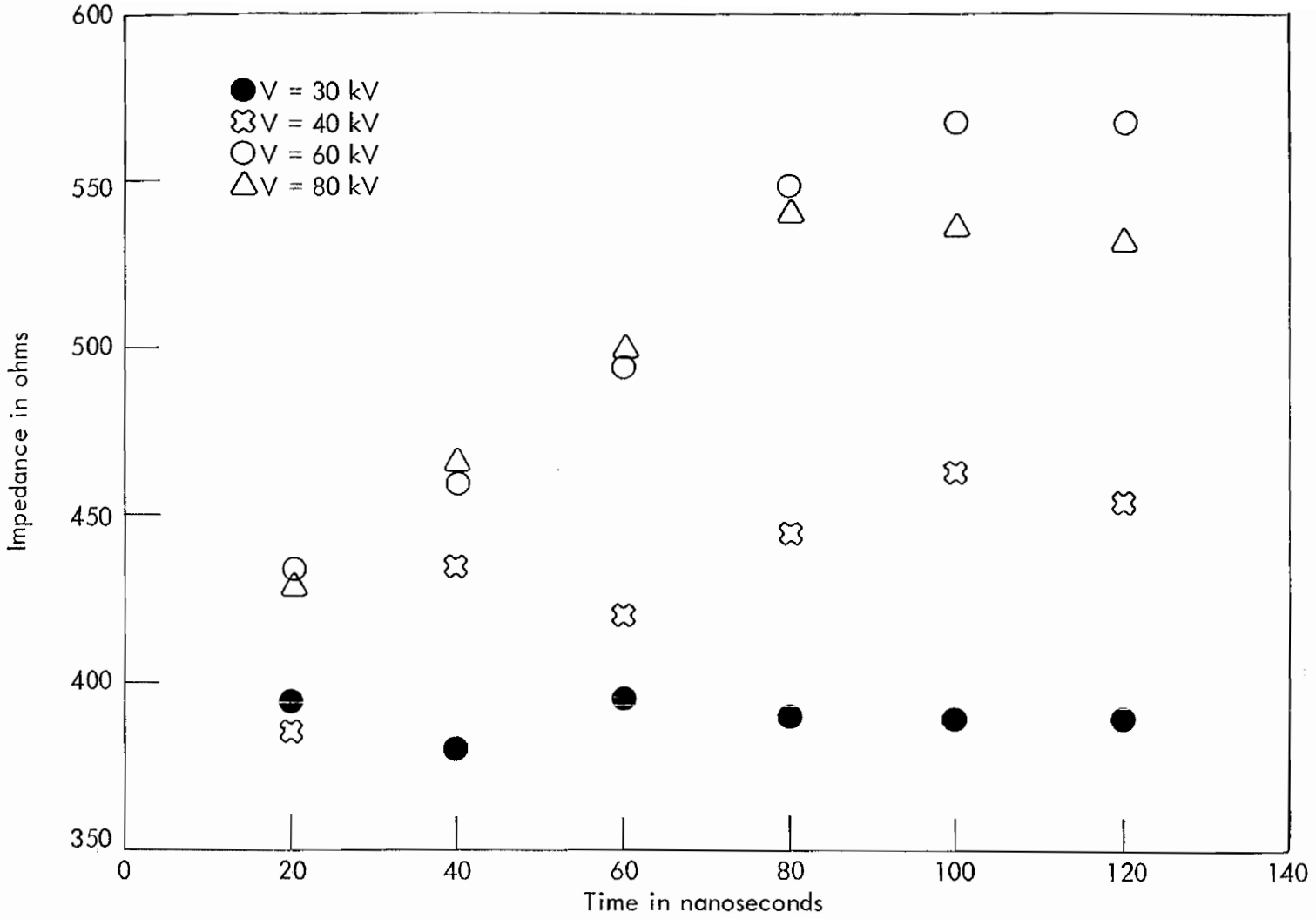

FIGURE 17

IMPEDANCE AS A FUNCTION OF TIME -STATION 3

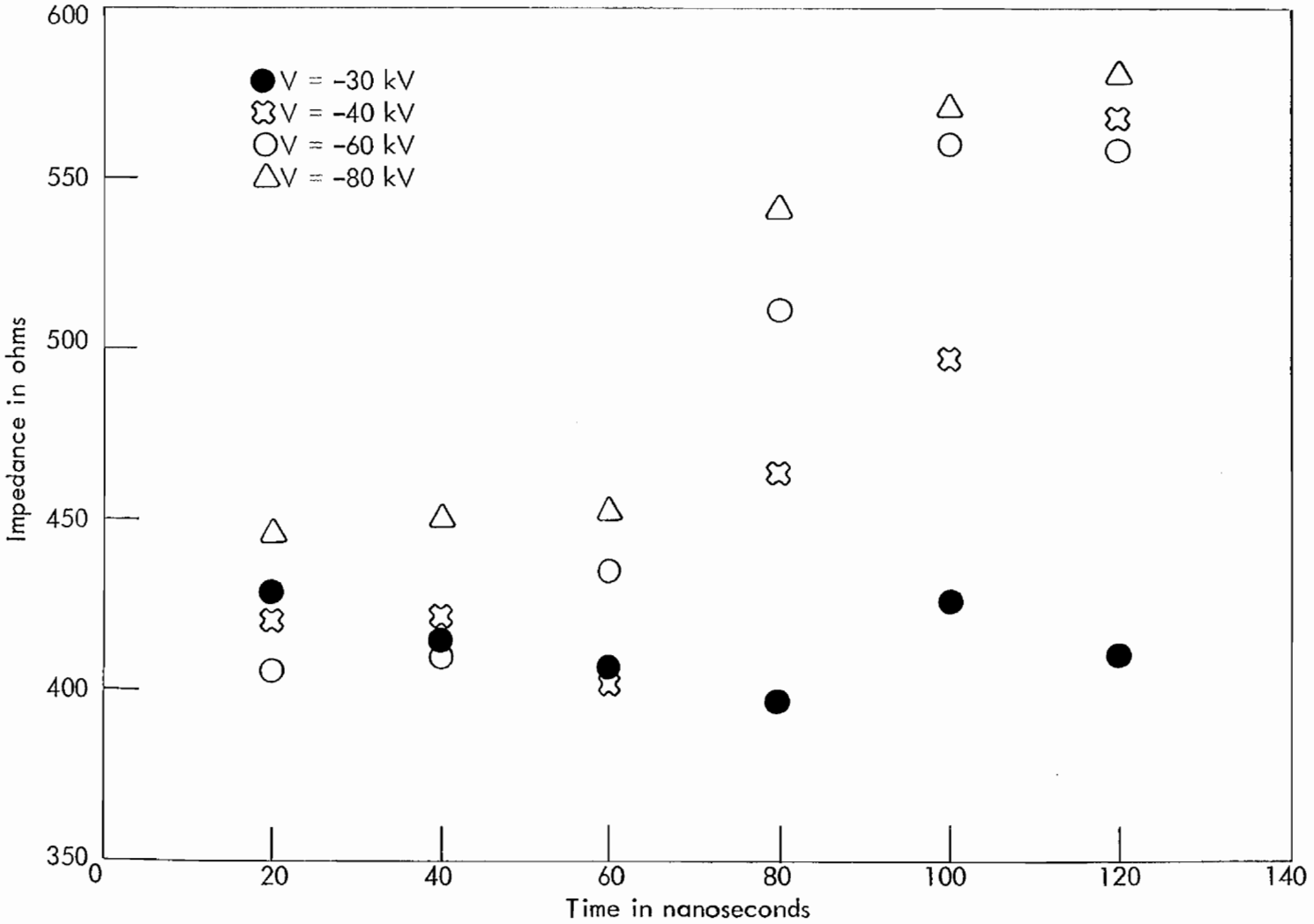

FIGURE 18

IMPEDANCE AS A FUNCTION OF TIME -STATION 5

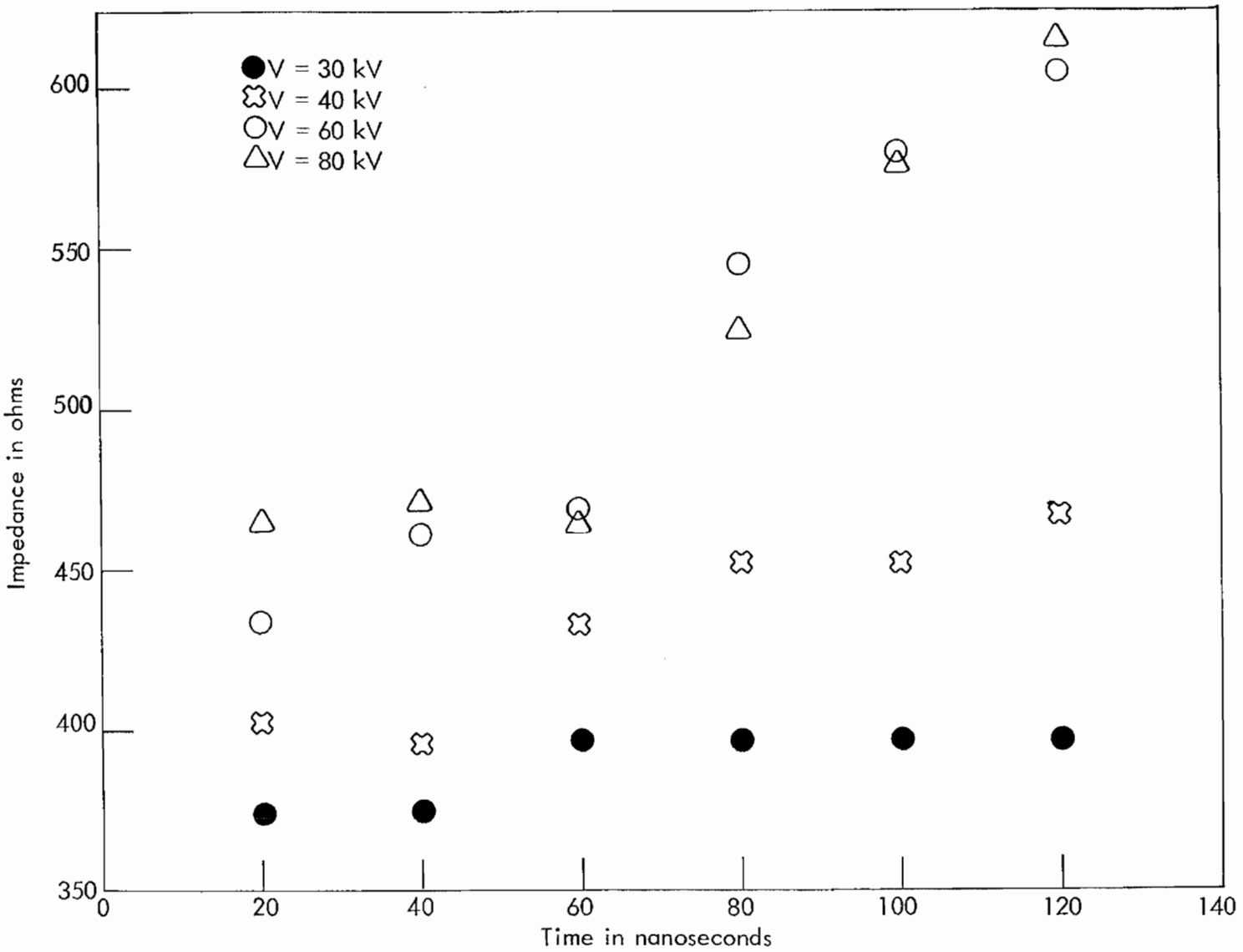

FIGURE 19
IMPEDANCE AS A FUNCTION OF TIME -STATION 5

TABLE 3

IMPEDANCE VALUES CALCULATED FROM PEAK DERIVATIVE DATA

PULSER VOLTAGE (kV)	V_{B1} (volts)	V_{D1} (volts)	Z1 (ohms)	V_{B3} (volts)	V_{D3} (volts)	Z3 (ohms)	V_{B5} (volts)	V_{D5} (volts)	Z5 (ohms)
-30	.95	1.25	374	.90	1.20	379	1.00	1.30	369
-40	1.80	2.40	379	1.80	2.55	402	1.70	2.50	418
-60	3.00	4.50	426	3.10	4.20	385	3.30	5.00	430
30 (1st pk)	.53	.70	376	.35	.50	406	.45	.65	411
30 (2nd pk)	.50	.72	409	.64	.90	399	.55	.80	413
40 (1st pk)	.73	1.00	389	.83	1.20	411	.68	.95	396
40 (2nd pk)	1.05	1.40	379	.85	1.30	434	1.00	1.45	412
60	4.40	6.40	413	4.50	7.00	442	4.80	7.40	438
80	5.80	7.50	368	6.00	9.00	426	7.00	10.0	406

It is reasonable to infer that the impedance variation indicated by Tables 2 and 3 is due to corona on the transmission wire. As an aid to understanding the phenomenon, it may be useful to examine the data to determine if B or D is more affected by corona. One method of doing this is to calculate normalized output signals for late times (the early time calculation would be somewhat ambiguous since the pulser risetime is relative slow and subject to pulse-to-pulse variations at the lower operating voltages). Table 4 is a summary of the B and D outputs per unit of applied voltage.

Several preliminary conclusions can be drawn from the raw test data irrespective of any further analysis or reduction:

(1) Some of the impedance values plotted in Figures 14 through 19 are corrupted by reflections from an imperfect line termination. Because of the measuring station spacing, the effects of pulse reflections will be apparent for $t > 20$ ns at station 5, $t > 100$ ns at station 3 and $t > 180$ ns at station 1.

(2) The corona threshold for 0.8114 mm diameter wire at 1 meter above a ground plane is somewhat less than plus or minus 30 kV.

(3) There is an observable corona starting time which generally decreases with applied voltage. However, it is difficult to quantify this parameter because of the variability of pulser risetime as a function of operating voltage.

TABLE 4

NORMALIZED OUTPUT SIGNALS FOR LATE TIMES

PULSER VOLTAGE (kV)	TIME (ns)	V_{B1} (mV)	$\frac{V_{B1}}{Vp}$	V_{D1} (mV)	$\frac{V_{D1}}{Vp}$	V_{B3} (mV)	$\frac{V_{B3}}{Vp}$	V_{D3} (mV)	$\frac{V_{D3}}{Vp}$	V_{B5} (mV)	$\frac{V_{B5}}{Vp}$	V_{D5} (mV)	$\frac{V_{D5}}{Vp}$
-30	60	13.5	.45	19	.63	14	.47	20.5	.68	14	.47	20	.67
	120	15	.50	21	.70	14	.47	21	.70	14.5	.48	21	.70
-40	60	22	.55	34	.85	19	.48	30	.75	17	.43	25	.63
	120	23	.58	39	.98	21	.53	38	.95	20	.50	40	1.00
-60	60	35	.58	60	1.00	31.5	.53	52	.87	29	.48	45	.75
	120	34	.57	61	1.02	32	.53	57	.95	31	.52	62	1.03
-80	60	47	.59	79	.99	42	.53	71	.89	39	.49	69	.85
	120	47	.59	82	1.02	43	.54	77	.96	41	.51	84	1.05
+30	60	15	.50	21	.70	14	.47	19.5	.65	15	.50	21	.70
	120	15	.50	21.5	.72	15	.50	20.5	.68	15	.50	21	.70
+40	60	20	.50	32	.80	17.5	.44	26	.65	17	.43	26	.65
	120	23	.58	41	1.05	20	.50	32	.80	17	.43	28	.70
+60	60	35	.58	58	.96	27.5	.46	48	.80	23	.38	38	.63
	120	36	.60	67	1.12	32	.53	64	1.17	29.5	.49	63	1.05
+80	60	50	.63	88	1.10	42	.53	74	.93	33	.41	53	.65
	120	52	.65	98	1.22	48	.60	90	1.12	41	.51	91	1.14

SECTION IV

CORONA MODEL

This section is concerned primarily with development of a simplified model to characterize the effects of corona on the transmission line. Some basic corona mechanisms are reviewed and the data are used to calculate an important parameter in the corona model. Also included in this section are some preliminary thoughts on an analytical approach for studying signal propagation under corona conditions.

1. BASIC PHYSICAL MECHANISMS OF CORONA

Ward has shown (ref. 2) that the Townsend Avalanche model is adequate for explaining the entire breakdown transition in air near atmospheric pressure. Previously, it was generally accepted that the avalanche model was valid for low pressures and low overvoltages and that for higher voltages and over-pressures, the so-called streamer model was valid. Thus, it is believed that the avalanche model should be adequate to explain the corona phenomena observed on the transmission line.

In the Townsend Avalanche model, residual free electrons, i.e., those caused by cosmic rays, photoionization, etc., are accelerated in the presence of an electric field. These accelerated electrons produce additional electrons upon colliding with air molecules. When the magnitude of the electric field is sufficiently high, the colliding electrons, in the process of ionizing the air, produce an increase in electrons, so that the free electron density increases. Such a condition is termed corona and the value of electric field at which the net free electron density starts to increase is

---

[2] Ward, A. L., "Calculations of Electrical Breakdown in Air at or Near-Atmospheric Pressure," Phys. Rev., Vol. 138, Number 5A, 31 May 1965.

termed the breakdown strength of air. The parameter which measures the rate of increase of electrons per unit volume is called the avalanche coefficient and is a strong function of the local electric field strength.

The major competing process to the production of electrons by ionization is the loss of electrons due to attachment, primarily oxygen attachment. The loss of electrons due to oxygen attachment is also a strong function of the local electrical field strength. The avalanching and attachment of electrons can be summarized in the continuity equation for free electrons; i.e.,

$$\nabla \cdot \vec{i}_e + \frac{\partial \rho_e}{\partial t} = (G-\alpha)\rho_e + \dot{S} \qquad (1)$$

where $\vec{i}_e$ is the electron current density

ρ_e is the electron charge/unit volume

$G \equiv G(E)$ is the avalanche coefficient

$\alpha \equiv \alpha(E)$ is the electron attachment rate

$\dot{S}$ is the residual production rate of free electrons due to natural causes, etc.

E is the electric field strength

The quantities G and α have been empirically determined, the best values apparently being those measured quite some time ago by A. V. Phelps at Westinghouse.

As the electric field is varied from low to high values, the quantity $G-\alpha$ in equation (1) changes sign, so that the character of the solution simultaneously changes from a stable to an unstable condition. The value of electric fields at which this transition occurs (approximately 2×10^6 volts/meter at 6000 foot altitude) separates regions of corona from those with no corona.

Another equation, similar to equation (1) could be written for the ions. However, for present considerations, the short time scales of interest seem to indicate that the electron motion is the predominant phenomenon.

Equation (1), together with Maxwell's equations and relations equating current, velocity, charge and mobility, are potentially soluble with appropriate boundary conditions at the cathode and/or anode. Such a solution has been attempted in connection with the Navy TACAMO programs. Unfortunately, the very small radii involved require, for numerical stability, extremely large computation times. Partial solutions obtained to date do indicate that space charge, and the resulting displacement currents, play a predominant role. The solutions also indicate that the corona region surrounding a small wire increases rapidly outwards and extends appreciable distances from the wire. Also, the corona region increases as the wave travels down the wire. These effects can be seen in the measured data.

2. CORONA EFFECT ON TRANSMISSION LINE PARAMETERS

It can be seen from the foregoing analysis that corona will cause a region of high, free-electron density in the immediate region surrounding the transmission line where the electric field is highest. The currents in this region cause both resistive losses and capacitive currents. A very simple model of the line above a ground plane is shown in Figure 20. If it is assumed that the corona loss resistance is very low or that the corona capacitance is very high, the radius of corona effects around the wire can be estimated from the measured data. In the following material, it is assumed that the corona resistance is very low, so that for capacitive purposes, the effective radius (corona radius) increases.

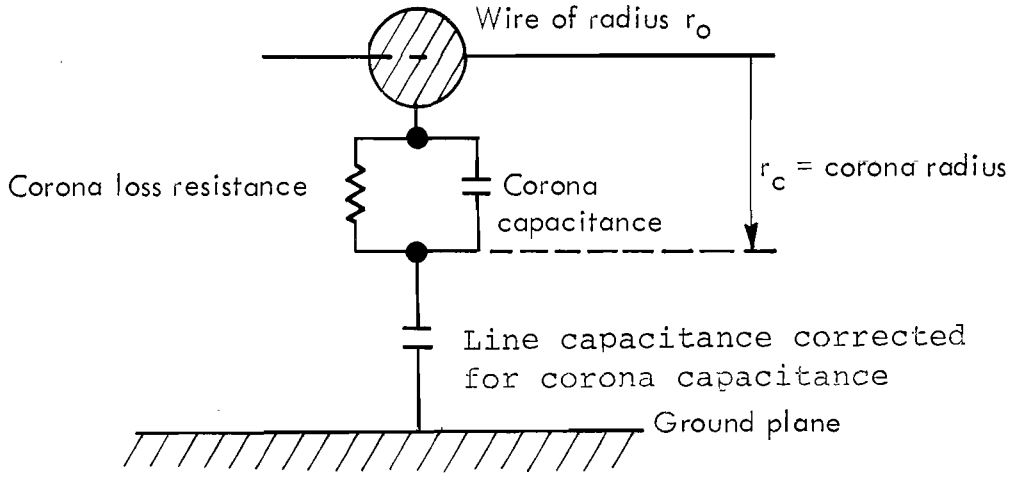

FIGURE 20A

SIMPLE MODEL OF THE EFFECTS OF CORONA ON THE TRANSMISSION LINE

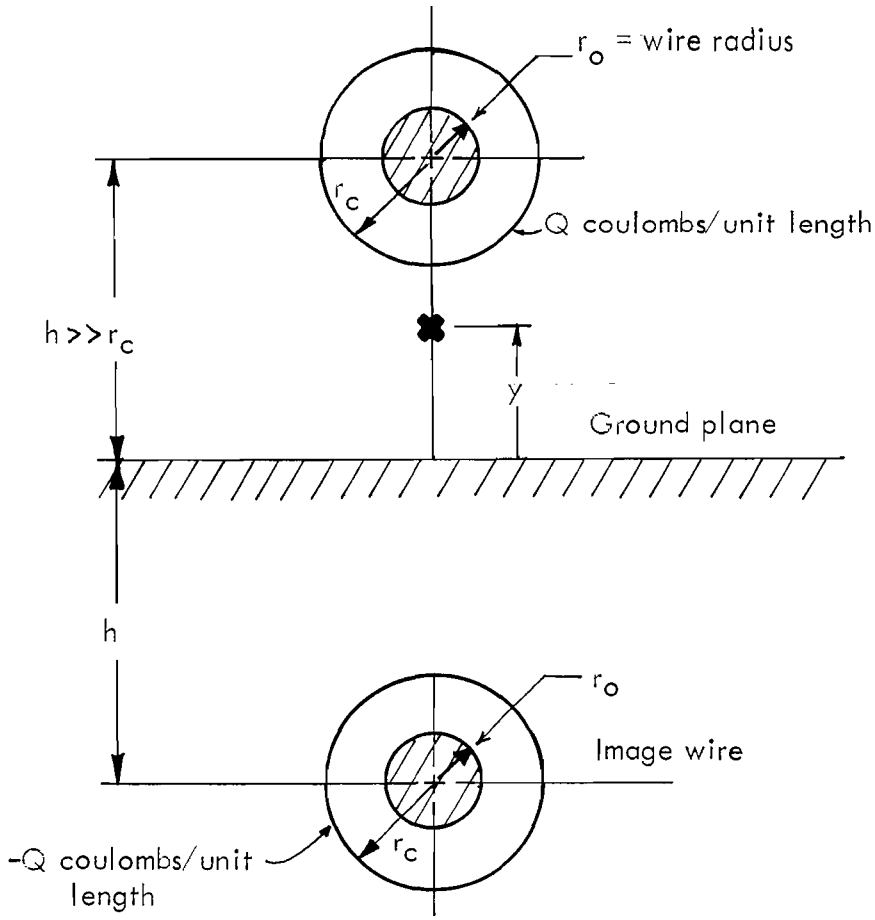

FIGURE 20B

CROSS-SECTION OF TRANSMISSION LINE

Refer to Figure 20 and assume that the conductor potential extends to the corona radius, r_c, where a charge of Q coulombs/unit length exists. The field at point y is

$$E_y = -\frac{Q}{2\pi\varepsilon_o}\left(\frac{1}{h-y} + \frac{1}{h+y}\right) \tag{2}$$

so that the potential difference between the corona radius and the ground plane is

$$V = -\int_o^{h-r_c} E_y dy = \frac{Q}{2\pi\varepsilon_o} \ln \frac{2h-r_c}{r_c} \approx \frac{Q}{2\pi\varepsilon_o} \ln \frac{2h}{r_c} \tag{3}$$

Combining equations (2) and (3), the electric field at y = 0 is

$$E_{y=o} = E_o = \frac{2}{h} \frac{V}{\ln \frac{2h}{r_c}} \tag{4}$$

If the line carries a current I, the magnetic field at y = 0 is

$$H_{y=o} = H_o = \frac{I}{\pi h} \tag{5}$$

so that the ratio of electric to magnetic field at y = 0 is

$$\frac{E_o}{H_o} = \frac{2\pi}{\ln \frac{2h}{r_c}} \frac{V}{I} \tag{6}$$

The capacitance of the line is Q/V; thus, from equation (3),

$$C = \frac{2\pi\varepsilon_o}{\ln \frac{2h}{r_c}}$$

The inductance of the line is

$$L = \frac{\phi}{I} = \frac{1}{I} \int_{r_o}^{h-r_o} B dy$$

Here the radius r_o is used since the magnetic field penetrates the plasma readily. Since,

$$B = - \frac{\mu_o I}{2\pi} \left\{ \frac{1}{h-y} + \frac{1}{h+y} \right\}$$

it follows that

$$\phi = \frac{\mu_o I}{2\pi} \ln \frac{2h-r_o}{r_o} \approx \frac{\mu_o I}{2\pi} \ln \frac{2h}{r_o}$$

so that

$$L = \frac{\mu_o}{2\pi} \ln \frac{2h}{r_o}$$

The characteristic impedance of the line is then

$$R_o = \sqrt{\frac{L}{C}} = \frac{V}{I} = \frac{1}{2\pi} \sqrt{\frac{\mu_o}{\varepsilon_o}} \sqrt{\ln \frac{2h}{r_o} \ln \frac{2h}{r_c}}$$

Using this value in equation (6) yields

$$\frac{E_o}{H_o} = \sqrt{\frac{\mu_o}{\varepsilon_o}} \sqrt{\frac{\ln \frac{2h}{r_o}}{\ln \frac{2h}{r_c}}} \tag{7}$$

Equation (7) can be used to determine the effective corona radius r_c in terms of the measured fields; that is,

$$r_c = 2h \left(\frac{r_o}{2h} \right)^{\frac{\mu_o}{\varepsilon_o} \left(\frac{H_o}{E_o} \right)^2} \tag{8}$$

$$= 2h \left(\frac{r_o}{2h} \right)^{\frac{\varepsilon_o}{\mu_o} \left(\frac{B_o}{D_o} \right)^2}$$

Equation (8) can also be written as

$$r_c = 2h \left(\frac{r_o}{2h}\right)\left(\frac{Z_o}{Z}\right)^2 \qquad (9)$$

where Z_o is the characteristic impedance of free space

Z is the impedance measured at the ground plane.

The graphs on the following pages (Figures 21 through 26) show the calculated corona radii versus time for stations 1, 3, and 5 which are each separated by 40 feet. The following conclusions can be drawn from these figures:

(1) Positive and negative excitations of the wire produce different results for corona radius.

(2) The threshold value of voltage to produce corona on this wire is less than 30 kV.

(3) For a given retarded time on the waveform, the corona radius increases with distance along the wire. Typical values at 100 ns for + 80 kV excitation are 25 mm, 30 mm, and 52 mm for stations 1, 3, and 5. The data have been presented this way in Figures 27 through 30.

(4) For a given spatial position along the wire, the corona radius increases with time for a given excitation voltage. For example, with -60 kV excitation, the corona radius at station 5 changes from 1.3 mm at 20 ns to 42 mm at 100 ns. The data do not unambiguously show whether or not the corona radius has stopped increasing by 100 ns, however, the data suggest in most cases corona radius is still increasing at 100 ns.

(5) The numerical values of corona radius inferred by the simple model are much larger that those which would be predicted from the static

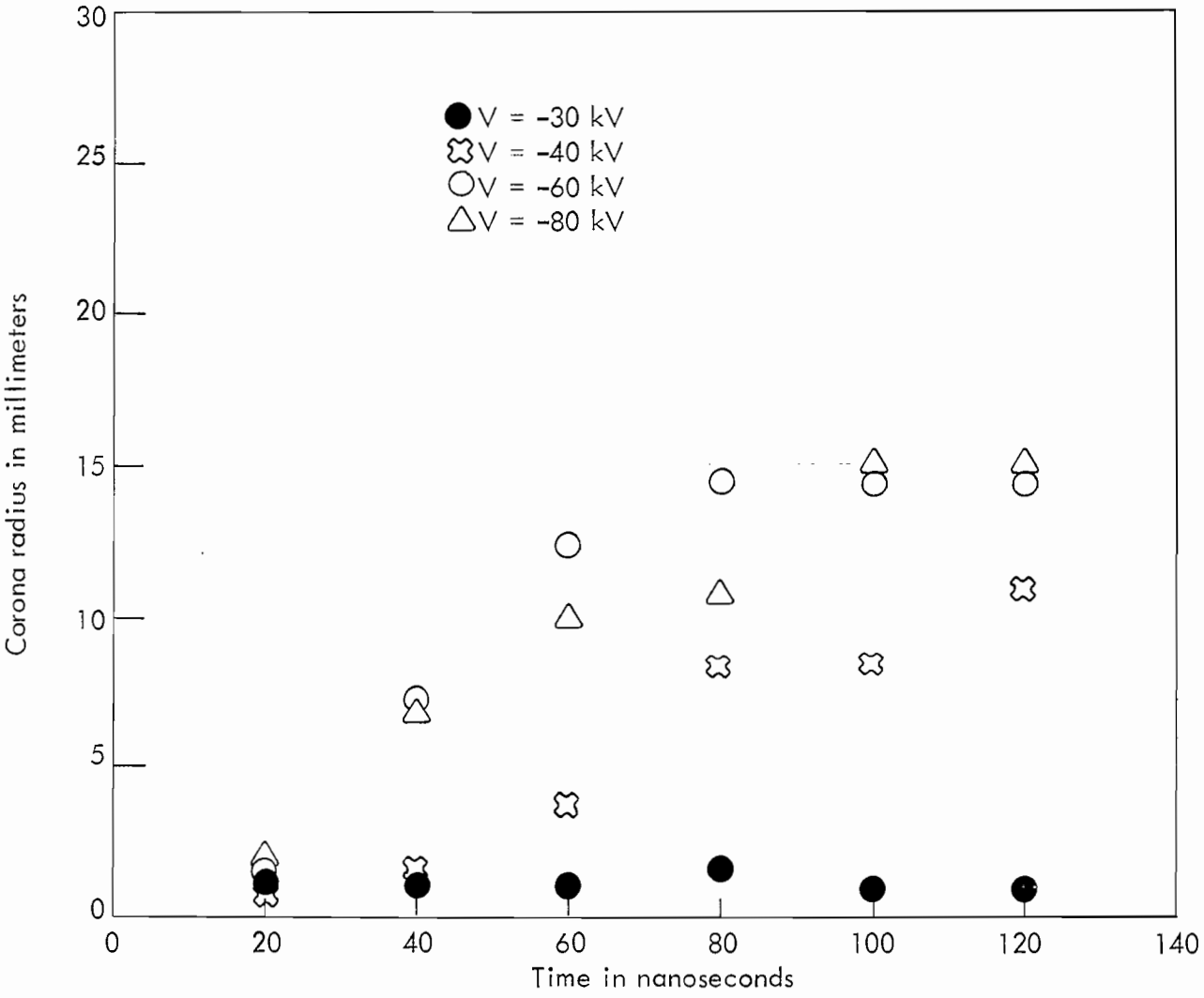

FIGURE 21

CORONA RADIUS AS A FUNCTION OF TIME - STATION 1

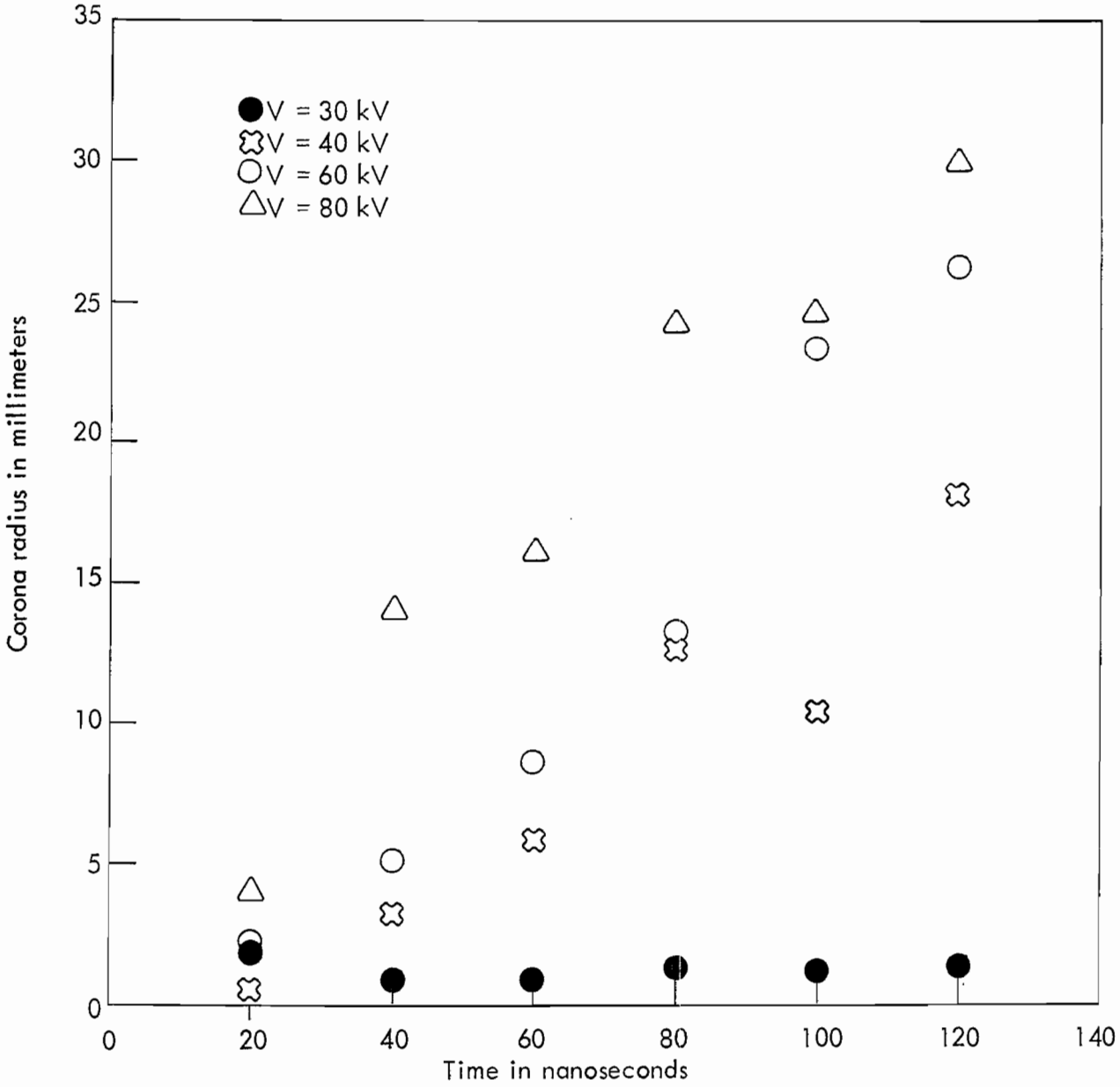

FIGURE 22

CORONA RADIUS AS A FUNCTION OF TIME -STATION 1

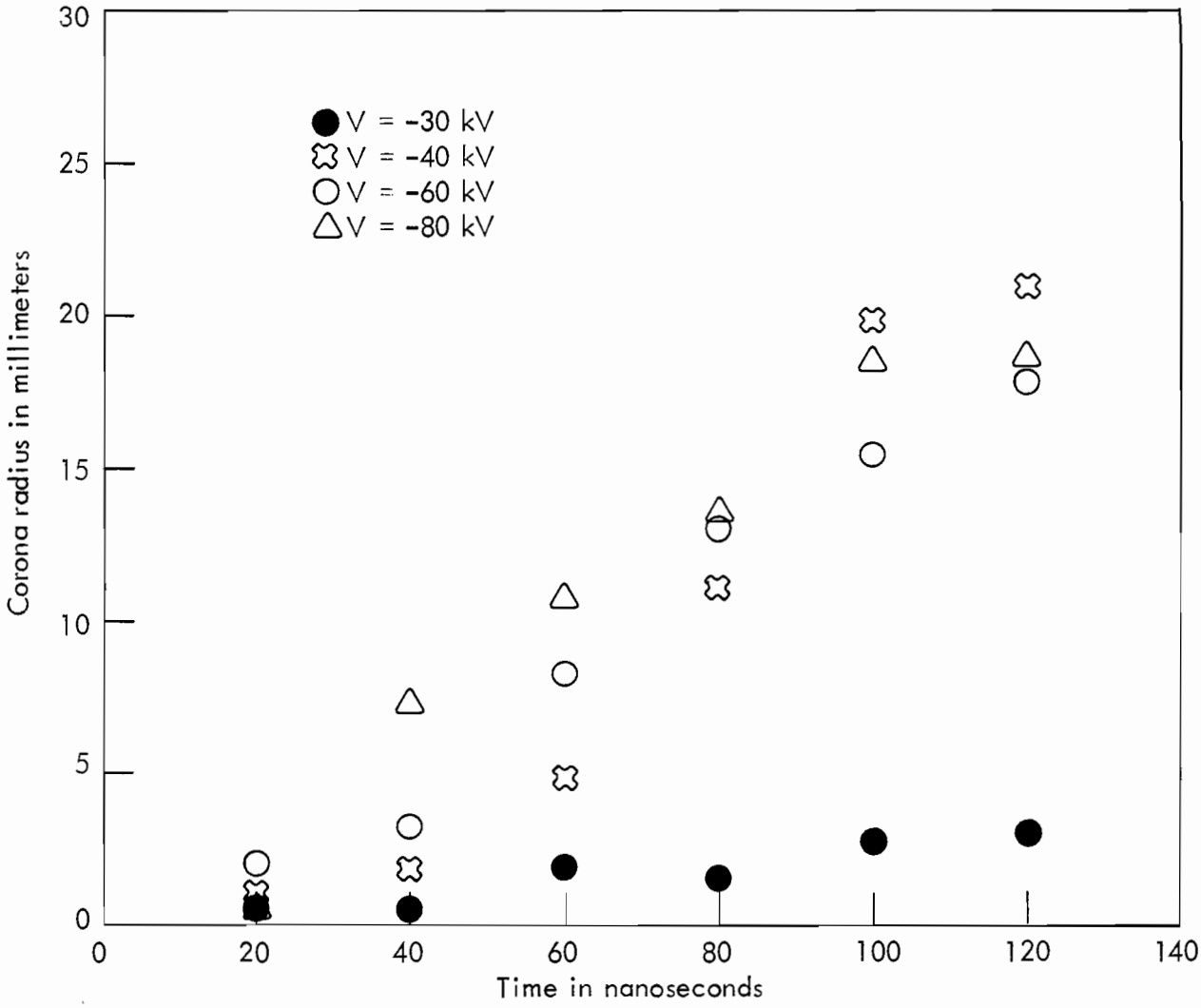

FIGURE 23

CORONA RADIUS AS A FUNCTION OF TIME - STATION 3

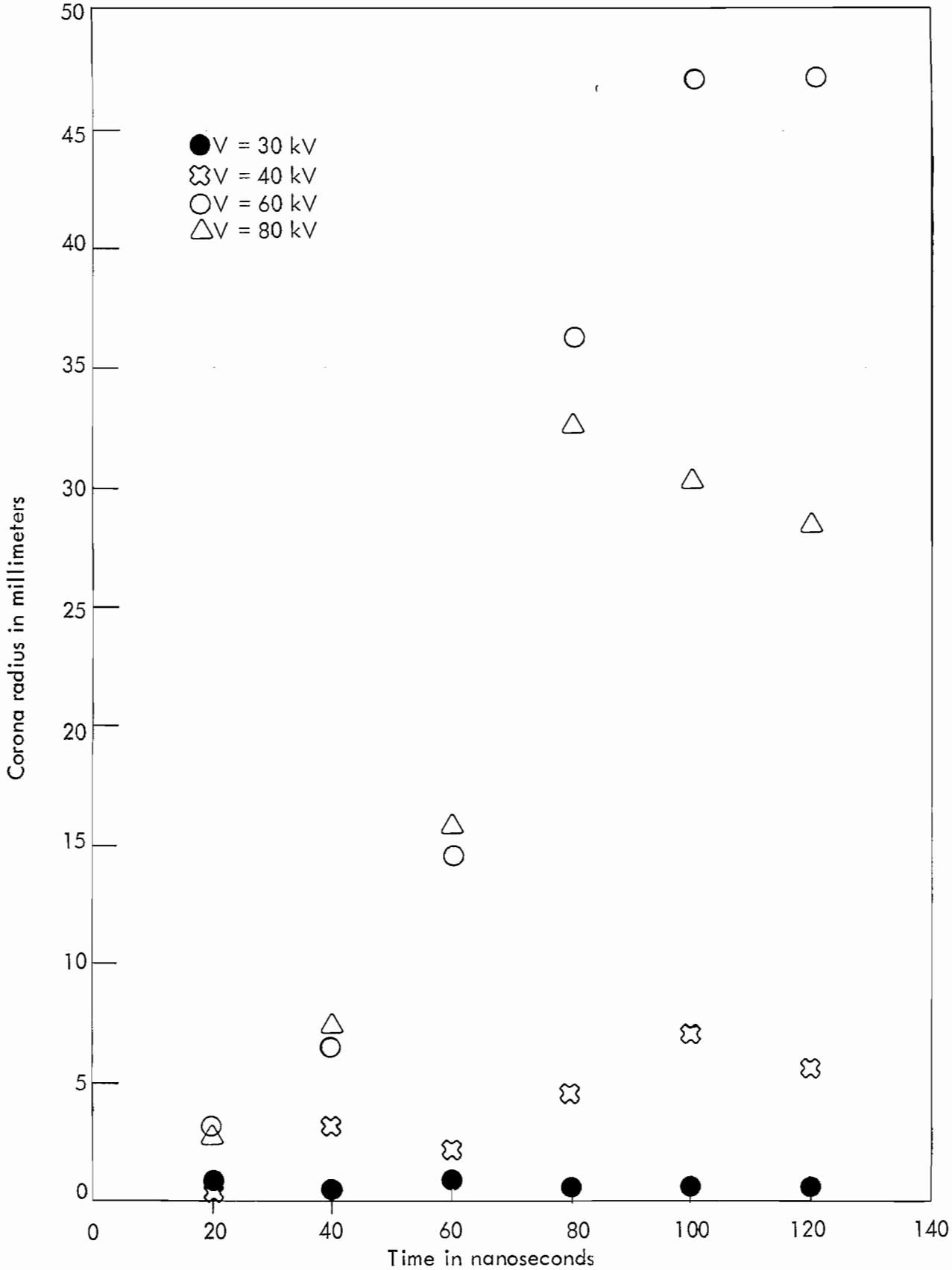

FIGURE 24

CORONA RADIUS AS A FUNCTION OF TIME - STATION 3

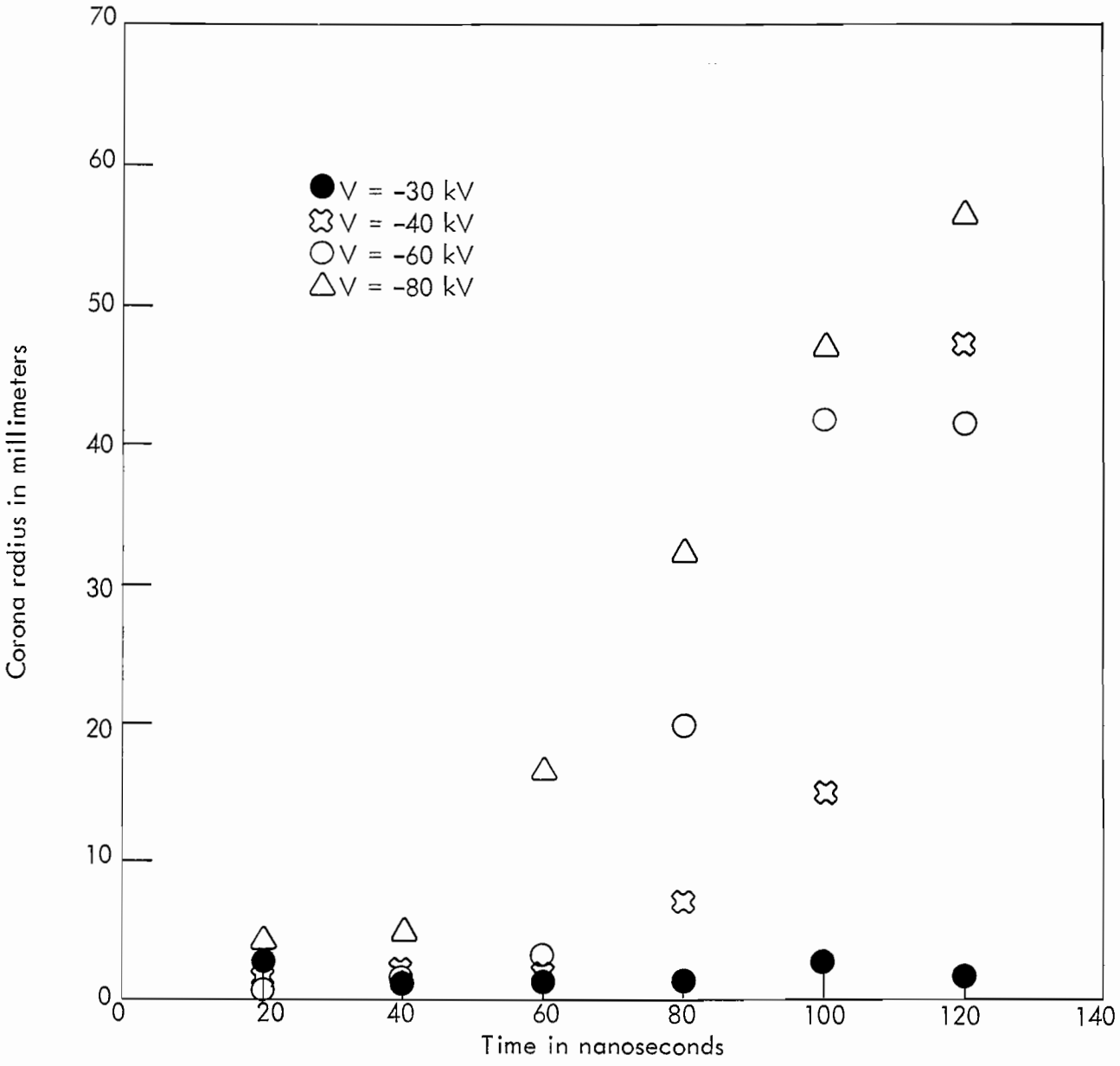

FIGURE 25

CORONA RADIUS AS A FUNCTION OF TIME - STATION 5

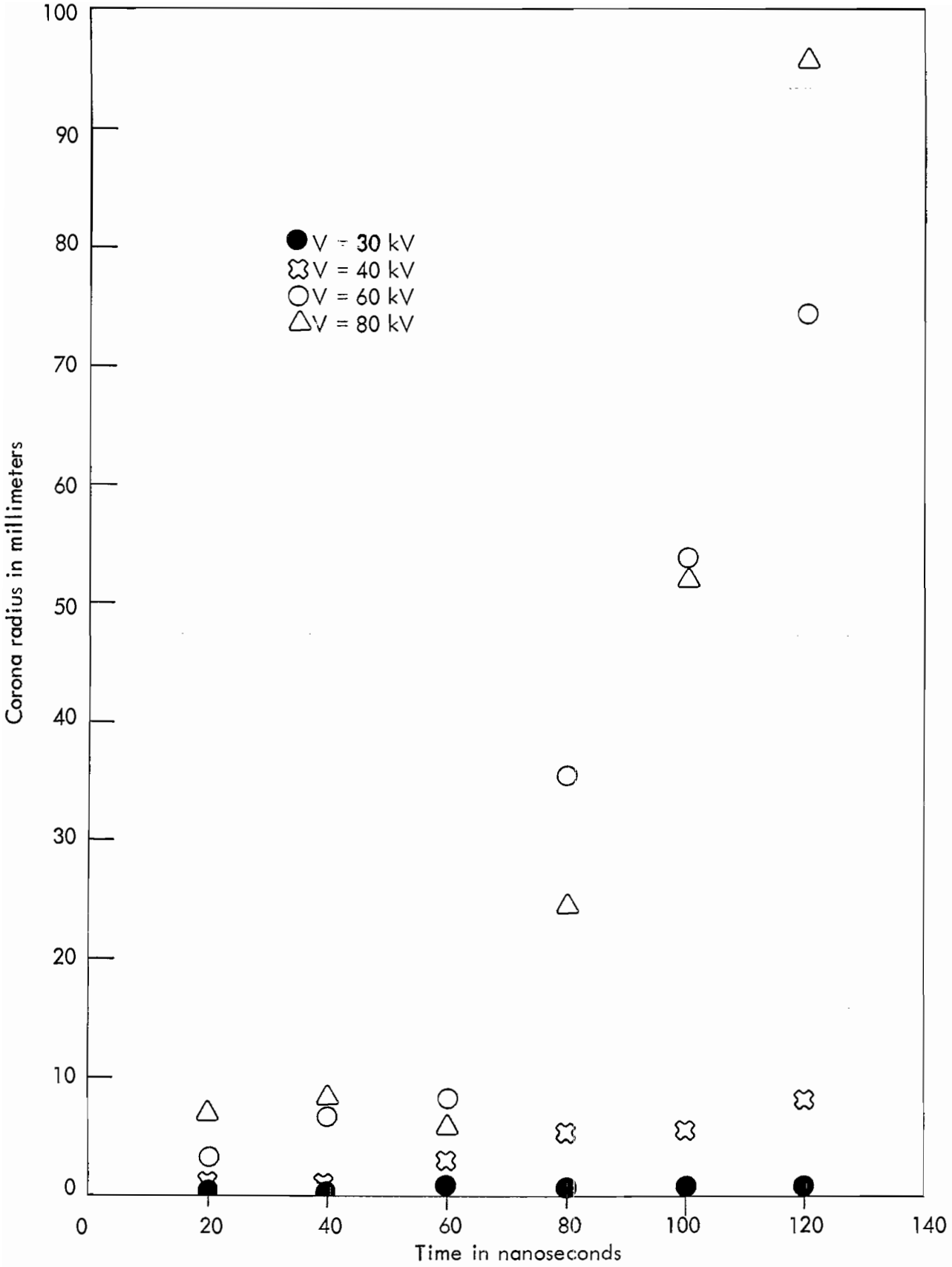

FIGURE 26

CORONA RADIUS AS A FUNCTION OF TIME - STATION 5

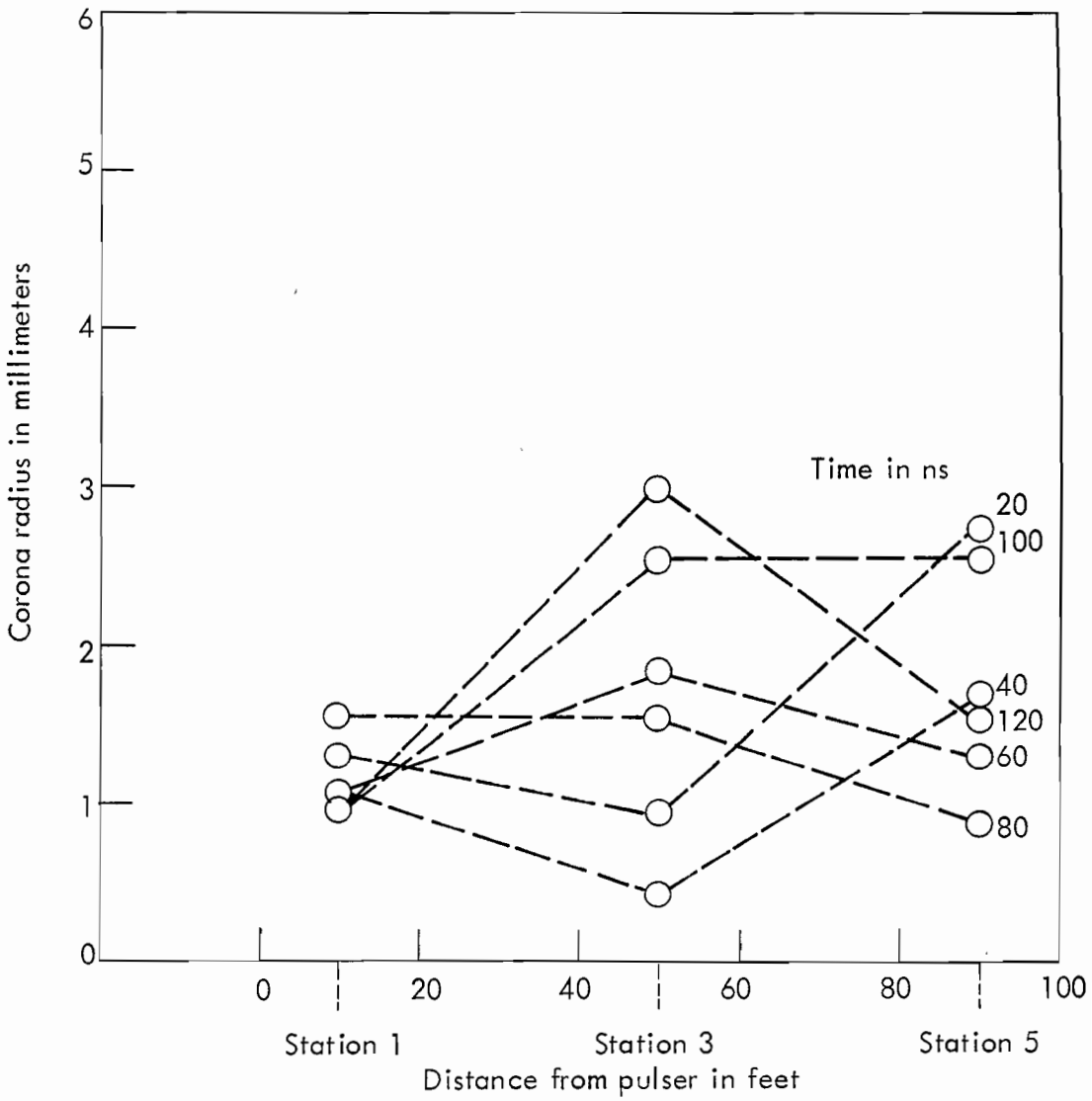

FIGURE 27

CORONA RADIUS AS A FUNCTION OF SPATIAL POSITION - V = -30 KV

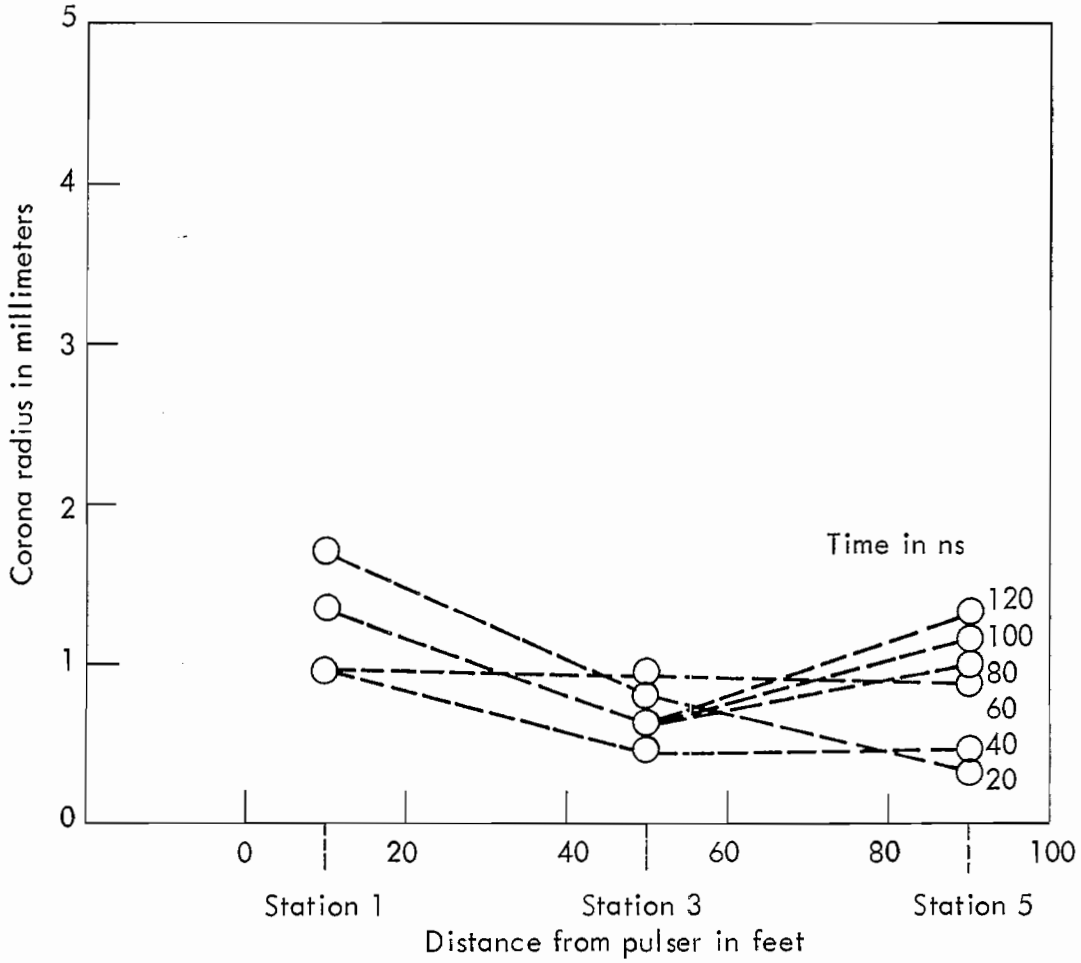

FIGURE 28

CORONA RADIUS AS A FUNCTION OF SPATIAL POSITION - V = 30 KV

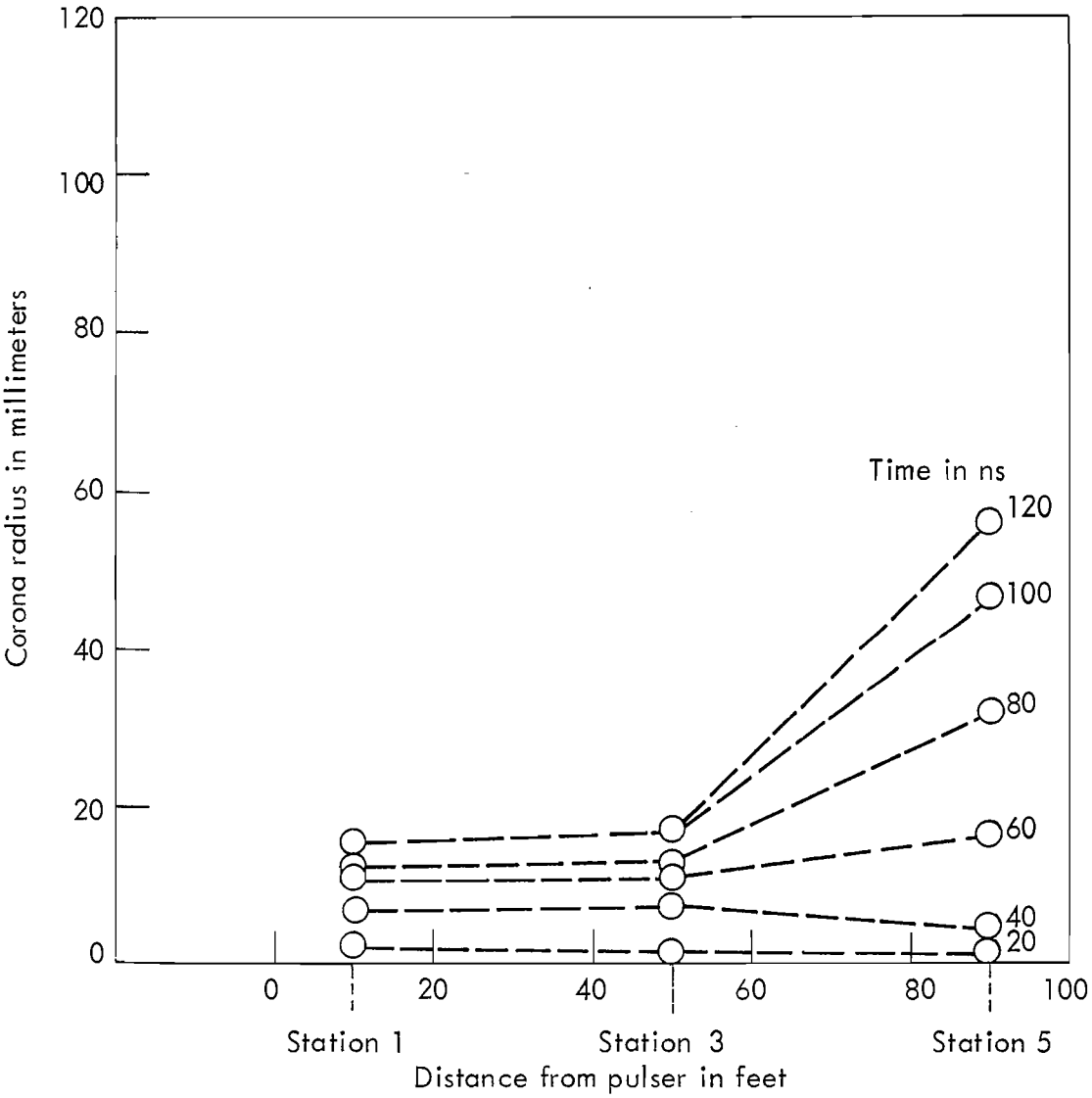

FIGURE 29

CORONA RADIUS AS A FUNCTION OF SPATIAL POSITION - V = -80 KV

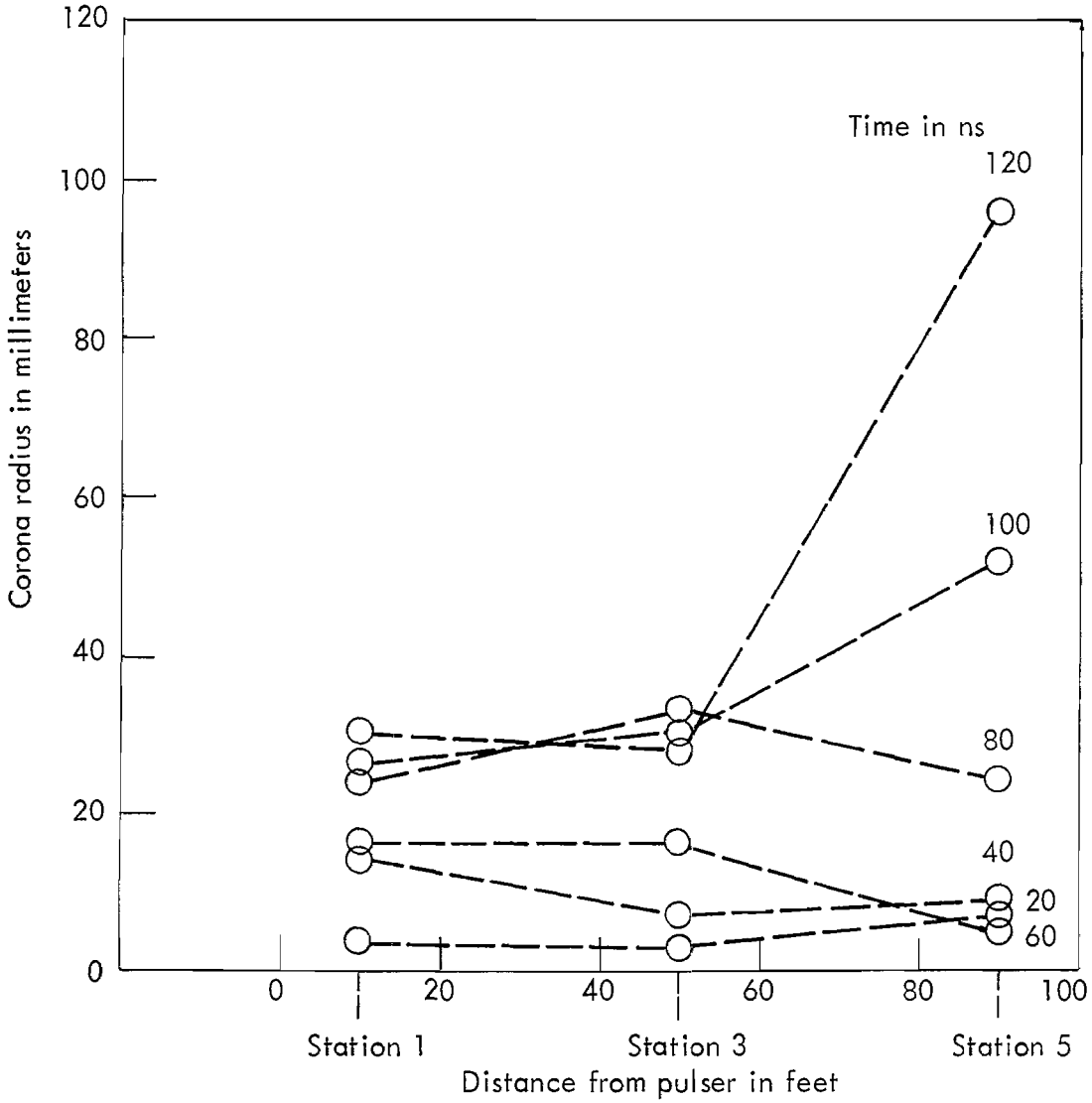

FIGURE 30

CORONA RADIUS AS A FUNCTION OF SPATIAL POSITION
V = 80 KV

approach of setting

$$E_r \approx \frac{V}{r_{cs} \ln \frac{2h}{r_{cs}}} \equiv 2 \times 10^6 \text{ v/m}$$

and inferring r_{cs} therefrom. Typical values of r_{cs} obtained this way are

Voltage (kV)	r_{cs} (mm)
30	2.2
40	3.1
60	5.0
80	7.1

Clearly charge transport, time and electric field modification play important roles in determining corona effects.

There is a third corona model which is more complex than the simple static model but somewhat simpler than the transmission line model presented in Figure 20. For late time intervals where the pulse reflections are not important, the current to voltage ratio is determined by the wire termination. Therefore, from equation (6), the corona radius is given by

$$\ln \frac{2h}{r_{ct}} = \frac{2\pi}{Z} \frac{V}{I}$$

$$r_{ct} = 2he^{-\frac{2\pi \times 510}{Z}} \qquad (10)$$

where r_{ct} is used to distinguish between r_c and r_{cs} calculated from the transmission line and static models, respectively. Table 5 is a summary of calculated values of r_{ct} for stations 3 and 5 at the longest time for which extensive data are available.

It is apparent from Table 5 that corona radii calculated from the line termination model are more in agreement with the static

model calculations than with the transmission line model calculations. Additional analytical and experimental work is required to resolve the differences among the models and determine which model provides the best representation of the corona phenomenon.

TABLE 5

CORONA RADII FROM LINE TERMINATION MODEL

PULSER VOLTAGE (kV)	TIME (ns)	CORONA RADIUS	
		STATION 3 (mm)	STATION 5 (mm)
-30	120	1.18	0.82
-40	120	3.97	7.09
-60	120	3.55	6.41
-80	120	3.64	8.13
+30	120	0.52	0.62
+40	120	1.72	2.12
+60	120	7.09	10.1
+80	120	4.90	12.5

3. SIMPLE TRANSMISSION LINE MODEL OF CORONA

The corona phenomenon is of interest to AFWL because of the potential impact on EMP pickup by long wire antennas trailing from the aircraft. In this coupling situation, attenuation and speed of pulses along the wire under corona conditions are of primary importance. The following transmission line model represents a preliminary effort towards the development of an analytical model for evaluating signal propagation under corona conditions.

Consider a short section of lossless transmission line in the presence of corona as shown in Figure 31. Two currents flow in a direction transverse to the line currents at the wire surface*: conduction current and displacement current. The

---

* These currents flow across the entire cross section of the line; however, the wire surface is a convenient place to quantify them.

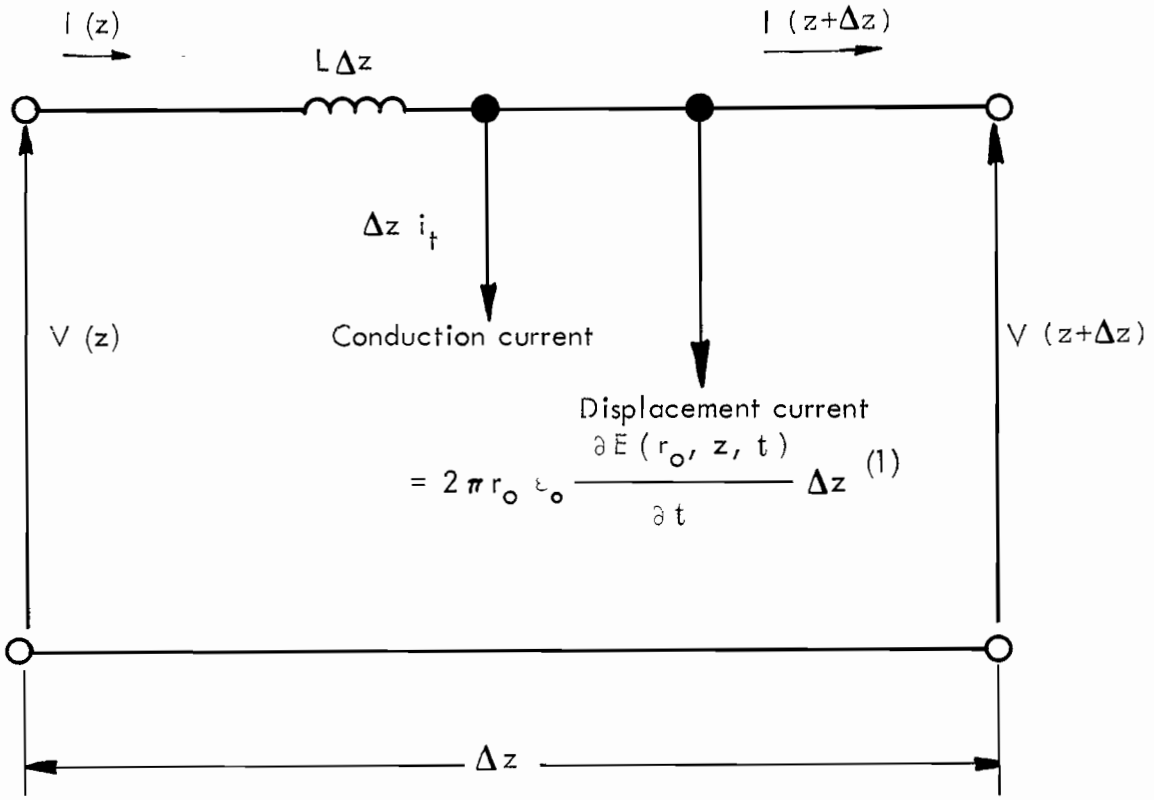

(1) This is the displacement current for a coaxial line

FIGURE 31

SECTION OF LUMPED TRANSMISSION LINE

conduction current, present only with corona, is due to actual charge transfer across the wire surface. The displacement current consists of two terms - the normal displacement current due to line capacity and a second term due to the displacement current induced by charge-transfer alteration of the electric field.

Kirchoff's laws applied to this short section of line yield, in the limit $\Delta z \to 0$

$$\frac{\partial V}{\partial z} = - L \frac{\partial I}{\partial t} \tag{11}$$

$$\frac{\partial I}{\partial z} = - 2\pi r_o \varepsilon_o \frac{\partial E(r_o,z,t)}{\partial t} - i_t \tag{12}$$

Combining equations (11) and (12), the expression which governs the line voltage is

$$\frac{\partial^2 V}{\partial z^2} - 2\pi L r_o \varepsilon_o \frac{\partial^2 E(r_o,z,t)}{\partial t^2} - L \frac{\partial i_t}{\partial t} = 0 \tag{13}$$

Since propagation occurs along the line at the speed of light, it is convenient to change equation (13) to retarded time; i.e.,

$$\tau = t - \frac{z}{\xi}$$

where ξ = speed of light.

With this change of variable, equation (13) becomes

$$\frac{\partial^2 V}{\partial z^2} - \frac{2}{\xi} \frac{\partial^2 V}{\partial z \partial \tau} + \frac{1}{\xi^2} \frac{\partial^2 V}{\partial \tau^2} - 2\pi L r_o \varepsilon_o \frac{\partial^2 E(r_o,z,\tau)}{\partial \tau^2} - L \frac{\partial i_t}{\partial \tau} = 0 \tag{14}$$

Assuming spatial derivatives are small compared with time derivatives, then

$$\frac{\partial}{\partial\tau}\left(-\frac{2}{\xi}\frac{\partial V}{\partial z}+\frac{1}{\xi^2}\frac{\partial V}{\partial\tau}-2\pi Lr_o\varepsilon_o\frac{\partial^2 E(r_o,z,\tau)}{\partial\tau^2}-Li_t\right)=0 \qquad (15)$$

or

$$\frac{\partial V}{\partial z}-\frac{1}{2\xi}\frac{\partial V}{\partial\tau}+\pi Lr_o\varepsilon_o\xi\frac{\partial E(r_o,z,\tau)}{\partial\tau}+\frac{L\xi}{2}i_t=f(z) \qquad (16)$$

when V is small, i_t is small and

$$\pi r_o\varepsilon_o\,\xi\frac{\partial E(r_o,z,\tau)}{\partial\tau}\rightarrow\frac{1}{2\xi}\frac{\partial V}{\partial\tau}$$

thus,*

$$\frac{\partial V}{\partial z}-\frac{1}{2\xi}\frac{\partial V}{\partial\tau}+\pi Lr_o\varepsilon_o\xi\frac{\partial E(r_o,z,\tau)}{\partial\tau}+\frac{L\xi}{2}i_t=0 \qquad (17)$$

Assume that $E(r_o,z,\tau)=E_{applied}+E_{induced}$; where, $E_{applied}$ is the field which exists in the absence of corona. For the coaxial geometry under consideration,

$$E_{applied}=\frac{V}{r\ln\frac{r_{max}}{r_o}}$$

so that equation (17) can be written

$$\frac{\partial V}{\partial z}+\pi Lr_o\varepsilon_o\xi\frac{\partial E_i(r_o,z,\tau)}{\partial\tau}+\frac{L\xi}{2}i_t=0 \qquad (18)$$

It is anticipated that the results from the corona radius model can be used to express the induced voltage and i_t terms as functions of line voltage and current. This would lead to a

---

* Dr. Carl Baum of AFWL has shown that this equation is true to the order of the last two terms on the left side.

differential equation for line voltage and current and thereby provide a basis for studying signal propagation under corona conditions. Additional work is required to develop this concept and fully evaluate its applicability.

SECTION V

CONCLUSIONS AND RECOMMENDATIONS

The experiment demonstrated the existence of a corona threshold in the range of plus or minus 30 kV for a 0.8114 millimeter diameter (A.W.G. No. 20) test wire suspended 1 meter above a ground plane. Basic calculations performed on the electric and magnetic field measurements show that the impedance at the ground plane increases as a function of retarded time, operating voltage and spatial position along the test wire.

A modeling effort associated with the experimental program resulted in a simple model which represents the corona phenomenon by a variable-radius conduction region (defined as the corona radius) around the actual conductor. Calculations of the conduction region from the test data and model equations show that the corona radii are much greater than the actual conductor radius. Moreover, the calculated corona radii increase as a function of retarded time, operating voltage and spatial position along the test wire due to the increase in measured impedance with these same variables.

A continuation of both the experimental and analytical phases of the program is recommended. Two changes in the test phase are recommended although the test facility and test results were generally satisfactory for an initial study program. The first change has to do with the acquisition of test data unambiguously below the corona threshold; this could be accomplished by changing to a larger diameter test wire or through the use of a lower-voltage spark gap in the high-voltage pulser. The second recommended change consists of increasing the length of the ground plane and transmission wire by about 50 feet to minimize the effects of the reflected pulse on the measured data. It is clear from the tabulated data presented in Section III and Figures 15 through 30 given in Section IV that the scatter of the data is more than can

reasonably be attributed to experimental uncertainty. It is believed that elimination of the reflected pulse would cause both the data and calculations based on the data to exhibit the expected monotonic characteristic.

One of the basic objectives of this study and related studies is to provide a framework for evaluating signal propagation on a conductor under corona conditions. This aspect of the problem was briefly considered in Section IV, Part 3, where the transmission line model was presented. Further analytical work with the transmission line model and/or other promising approaches is recommended.

APPENDIX

ELECTRIC AND MAGNETIC FLUX DATA

This appendix is a compilation of B, D, $\dot{B}$ and $\dot{D}$ data for a test voltage range from $\pm$ 30 kV to $\pm$ 80 kV. The data are identified by a pair of alphanumeric characters where the alphabetical character designates the type of data and the number designates the measuring station. Station 1 is near the pulser, station 3 is midway between the pulser and the termination, and station 5 is near the termination. The characters displayed in the upper sections of each photograph are the vertical and horizontal deflection factors in terms of volts/division and time/division, respectively.

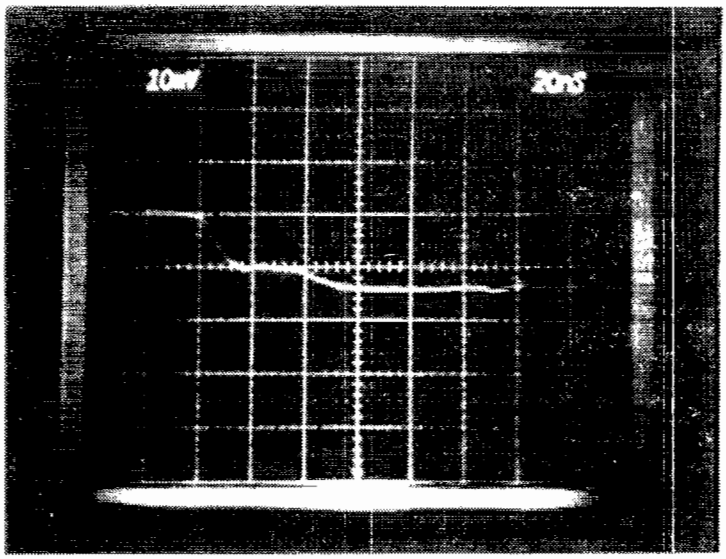

B1

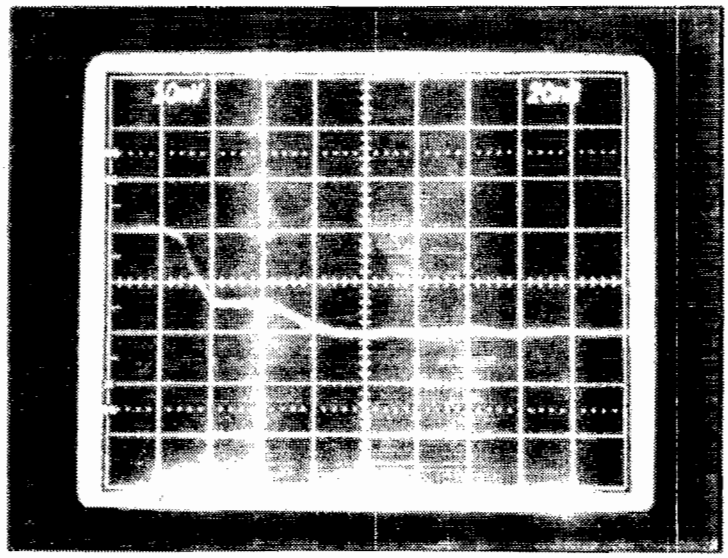

D1

FIGURE A1

B AND D DATA FOR -30 KV

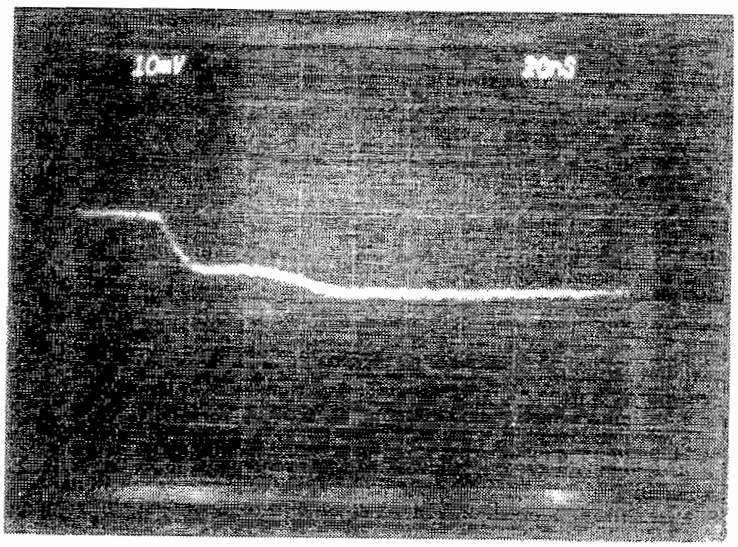

B3

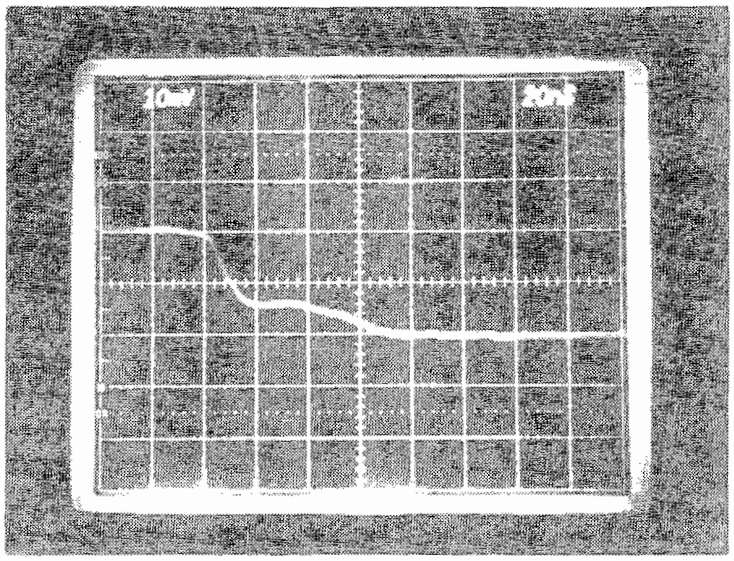

D3

FIGURE A1 (Continued)
B AND D DATA FOR -30 KV

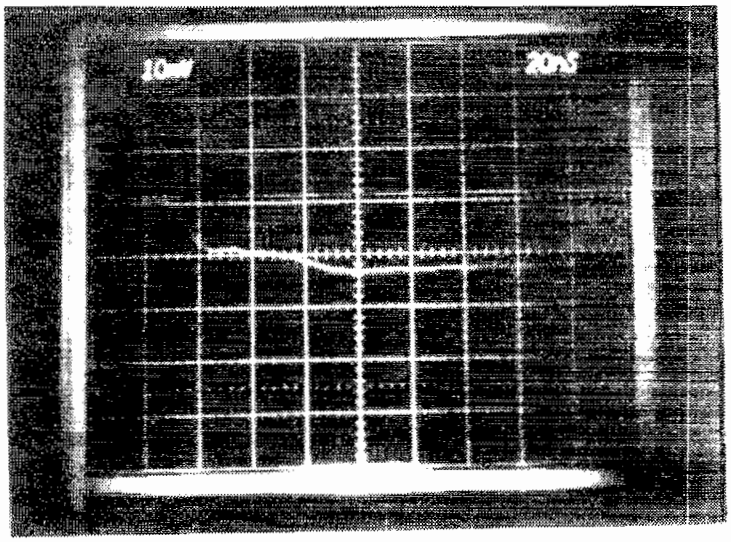

B5

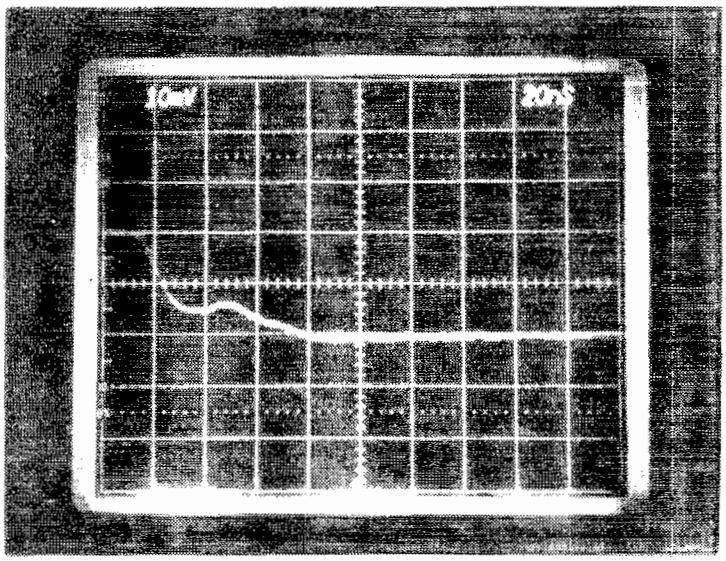

D5

FIGURE A1 (Continued)
B AND D DATA FOR -30 KV

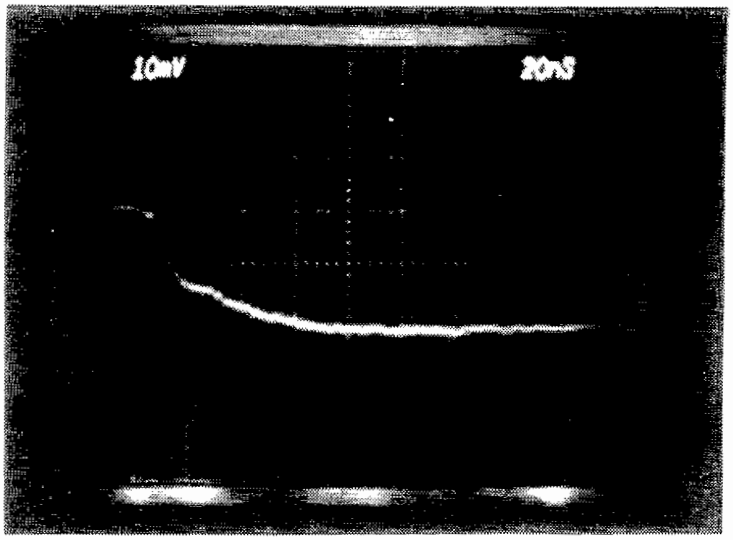

B1

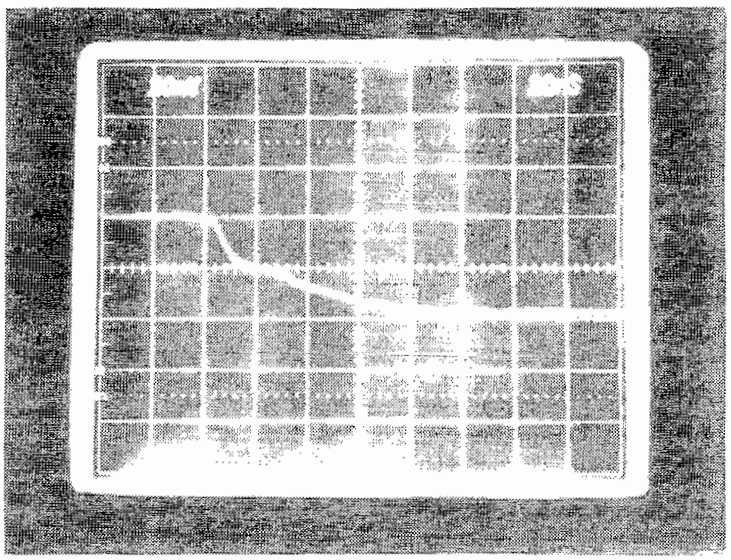

D1

FIGURE A2
B AND D DATA FOR -40 KV

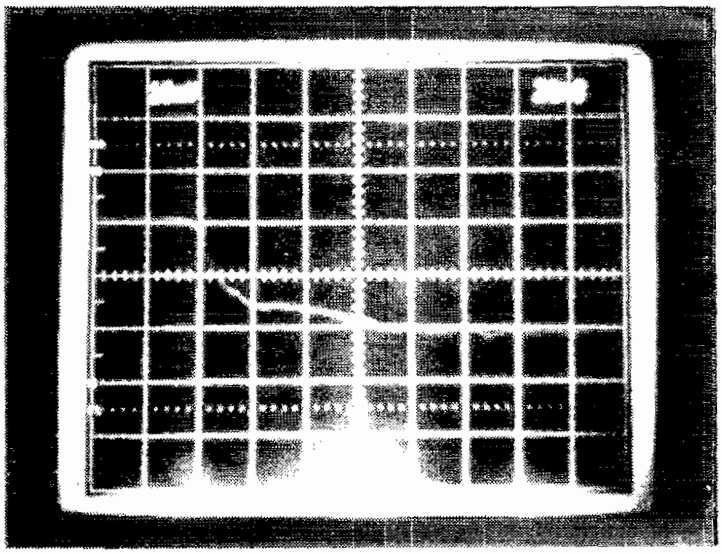

B3

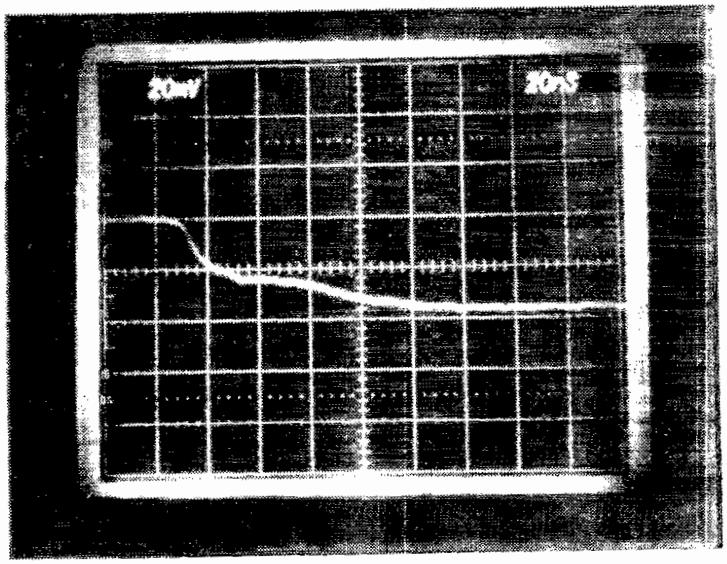

D3

FIGURE A2 (Continued)
B AND D DATA FOR -40 KV

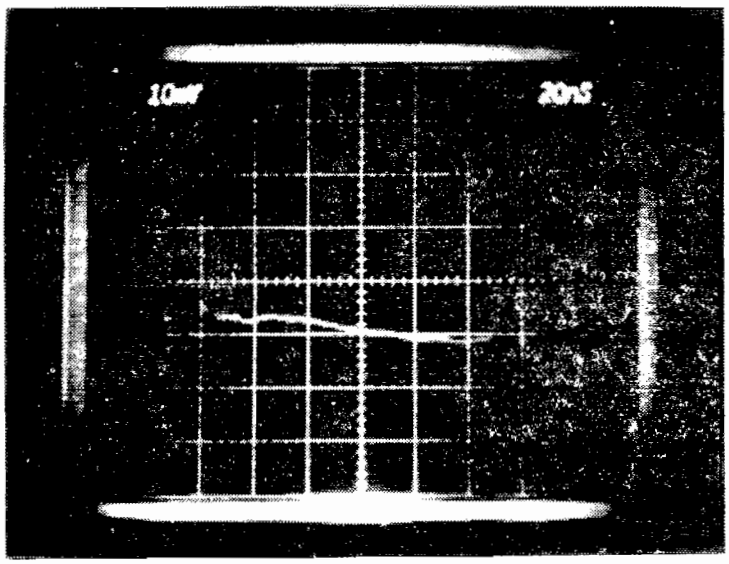

B5

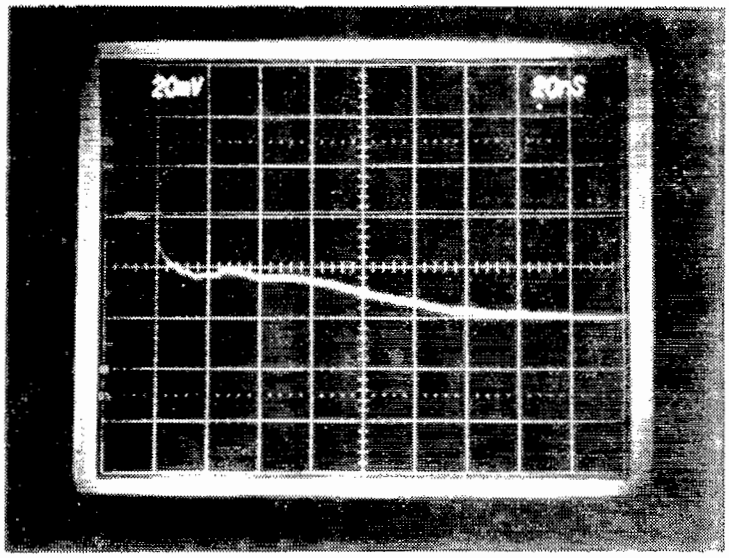

D5

FIGURE A2 (Continued)
B AND D DATA FOR -40 KV

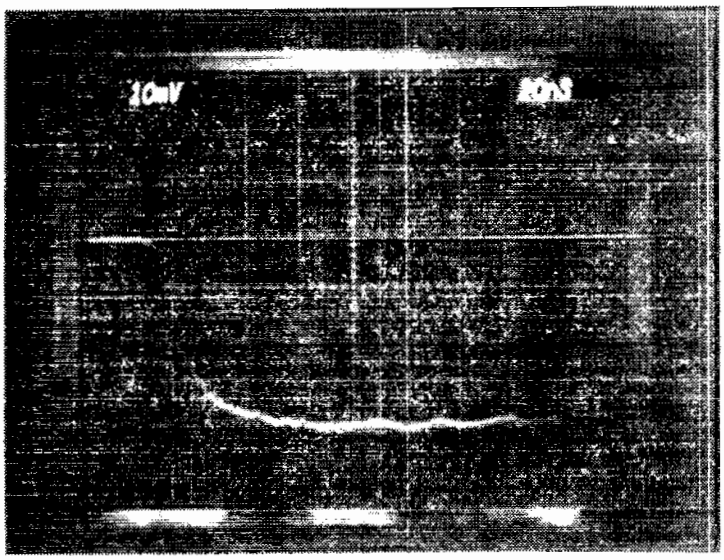

B1

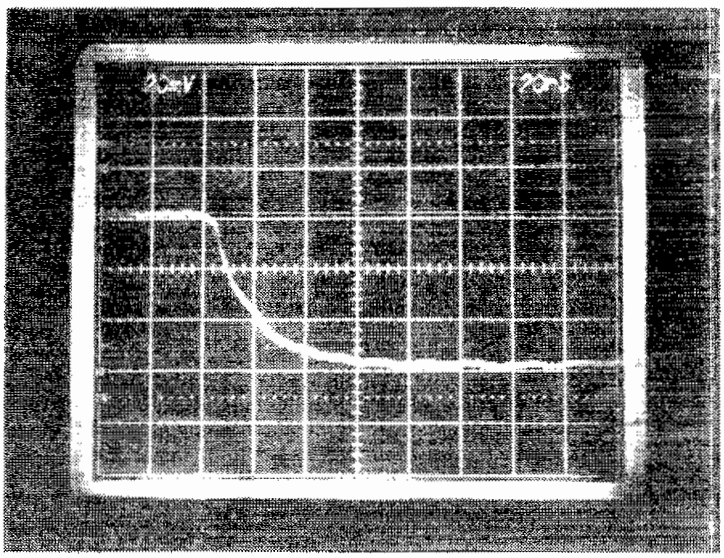

D1

FIGURE A3
B AND D DATA FOR -60 KV

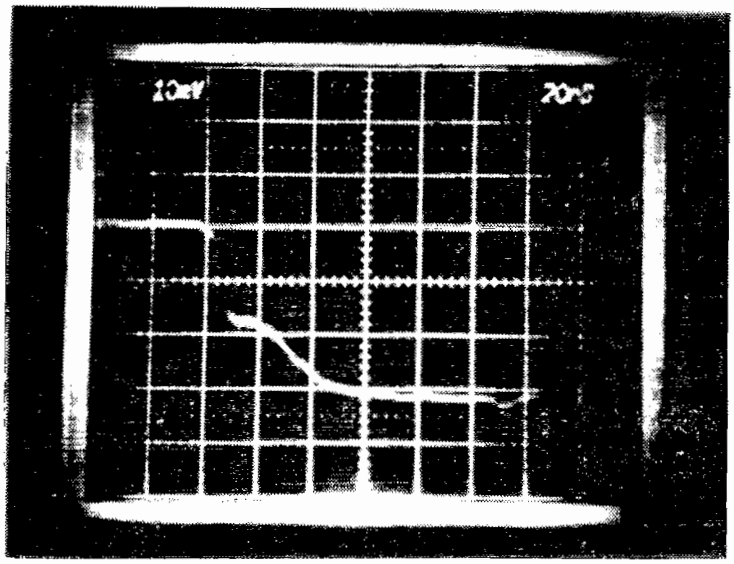

B3

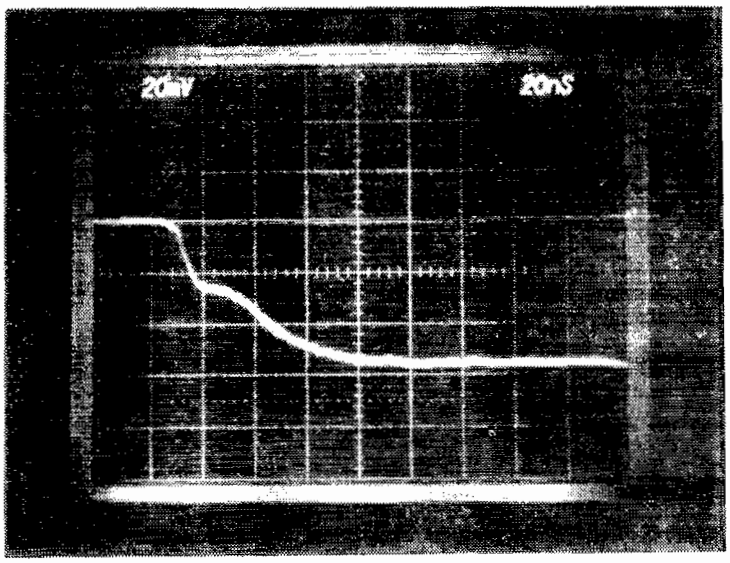

D3

FIGURE A3 (Continued)
B AND D DATA FOR -60 KV

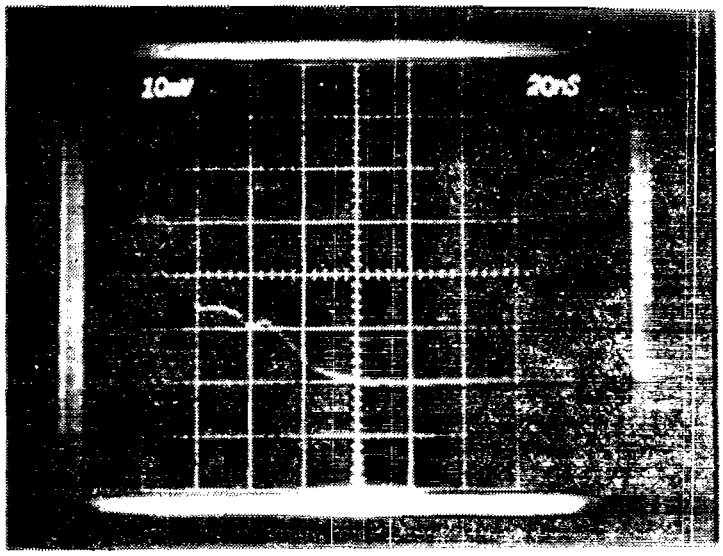

B5

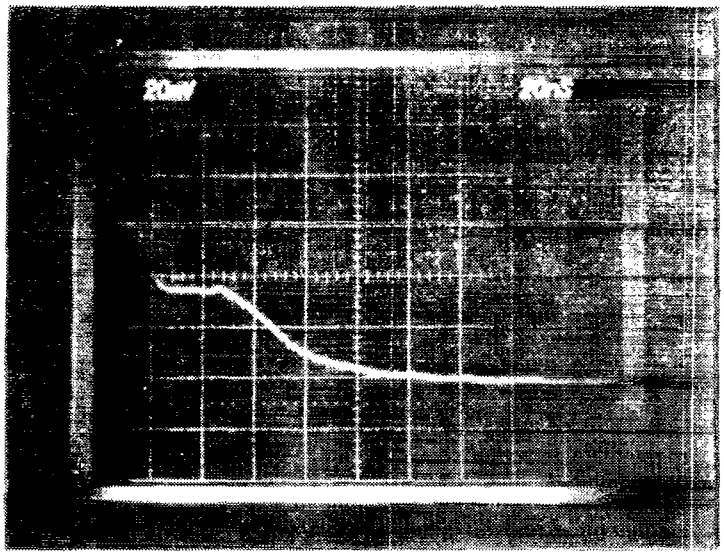

D5

FIGURE A3 (Continued)
B AND D DATA FOR -60 KV

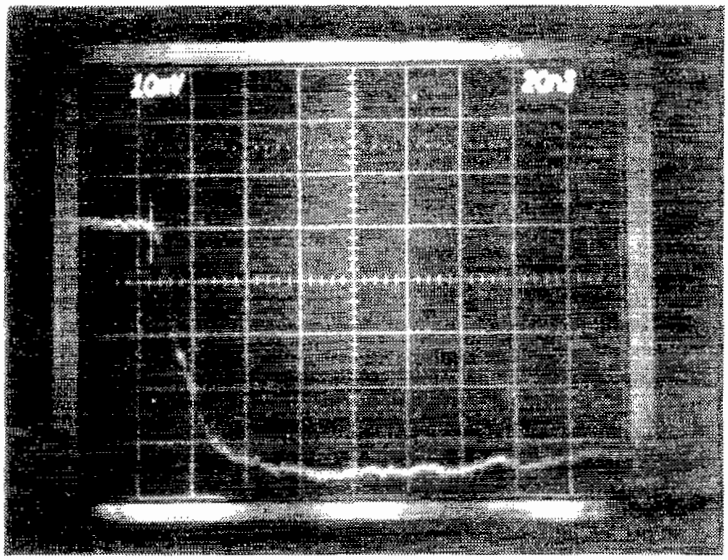

B1

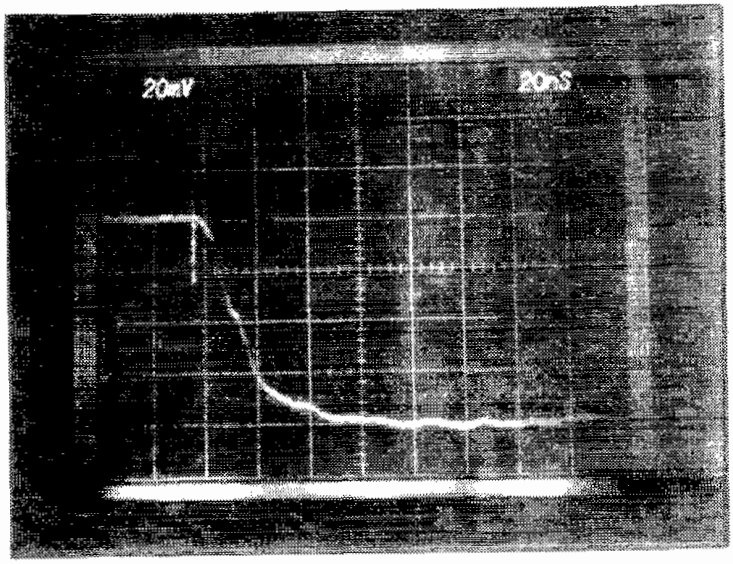

D1

FIGURE A4
B AND D DATA FOR -80 KV

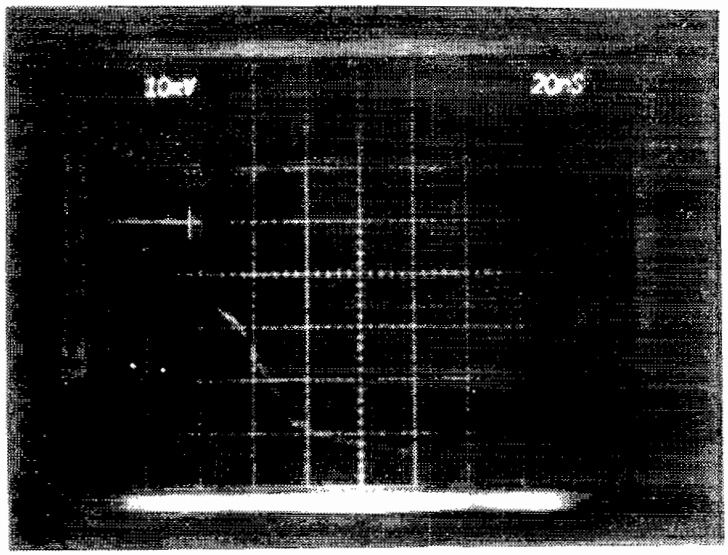

B3

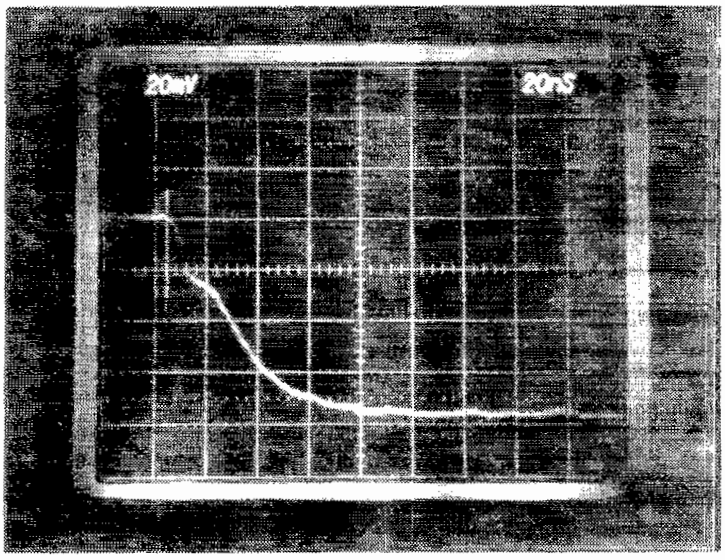

D3

FIGURE A4 (Continued)
B AND D DATA FOR -80 KV

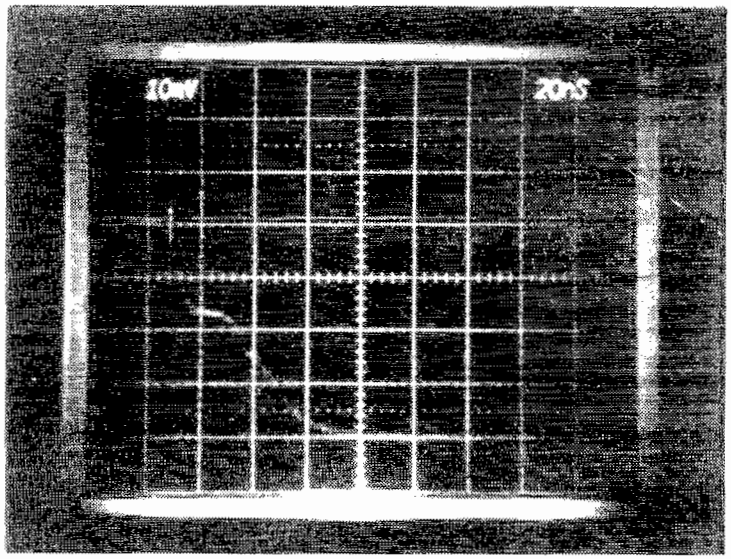

B5

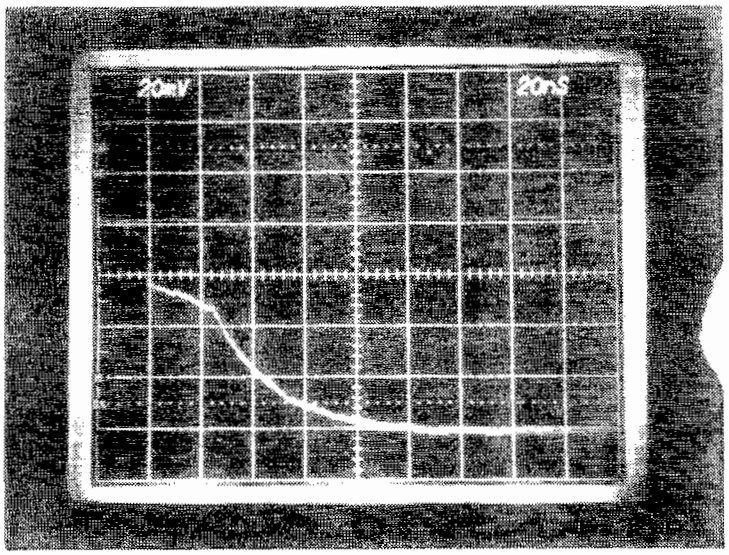

D5

FIGURE A4 (Continued)
B AND D DATA FOR -80 KV

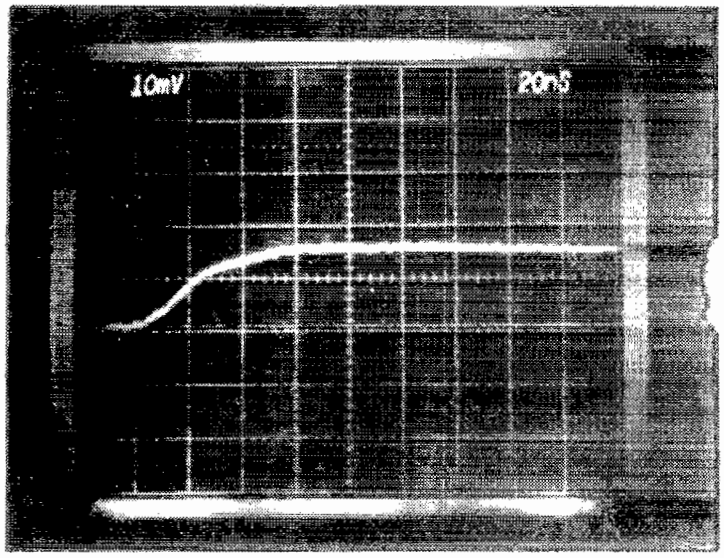

B1

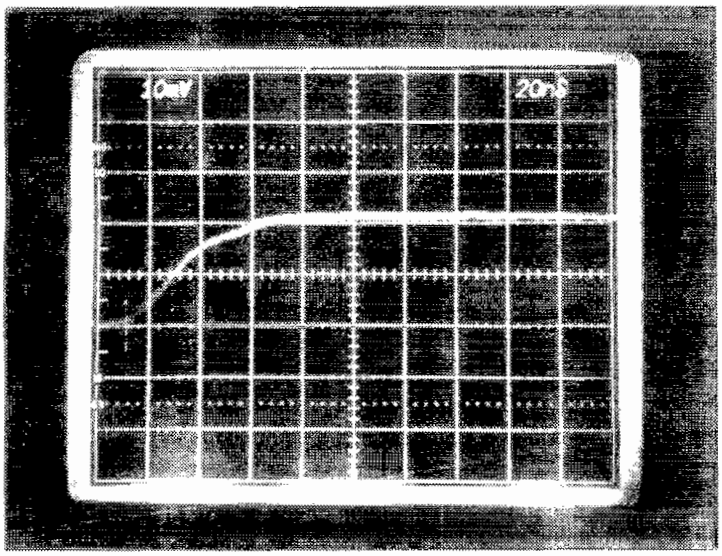

D1

FIGURE A5
B AND D DATA FOR +30 KV

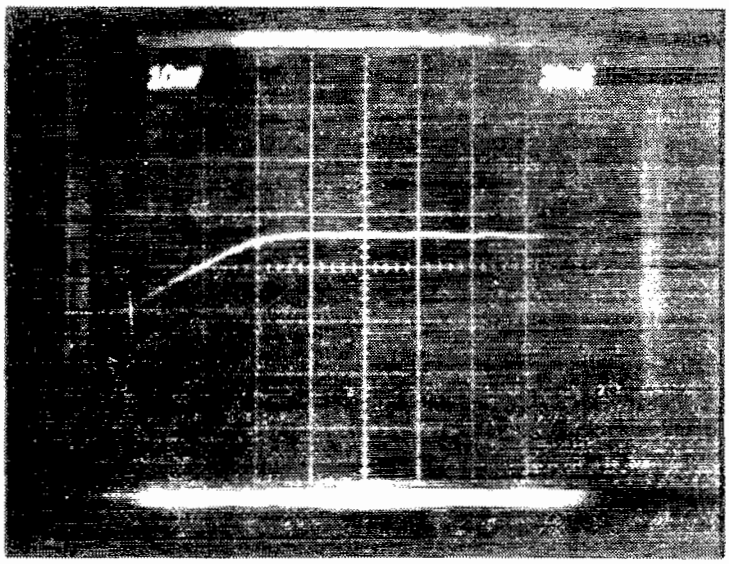

B3

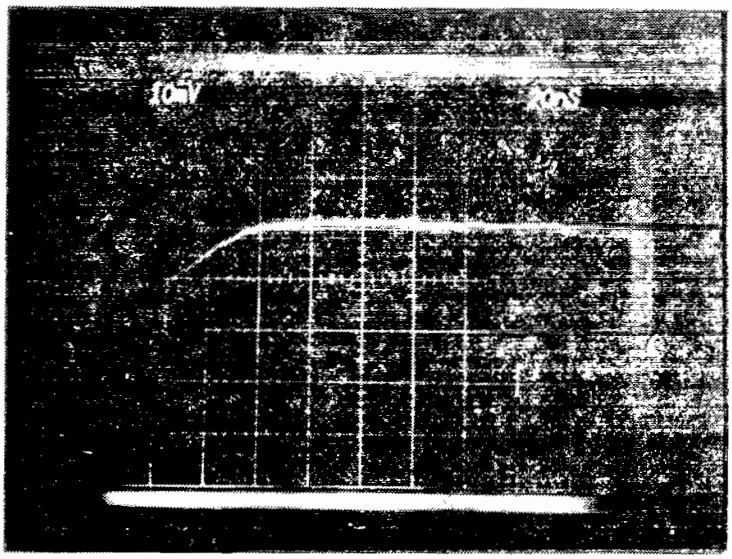

D3

FIGURE A5 (Continued)
B AND D DATA FOR +30 KV

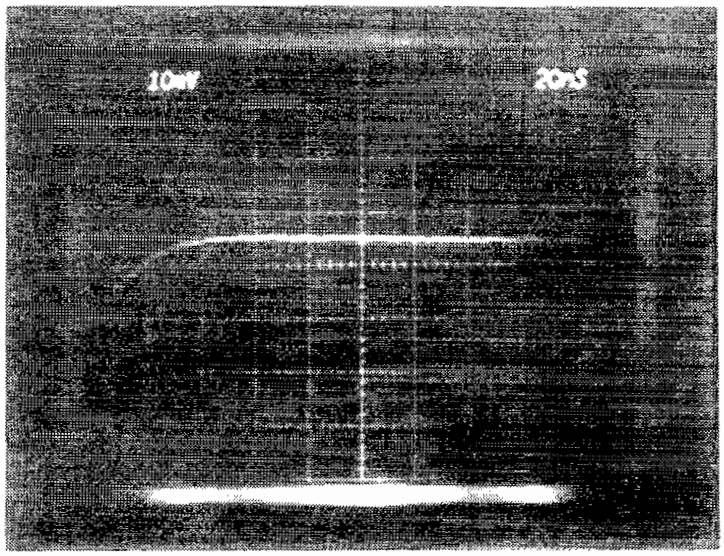

B5

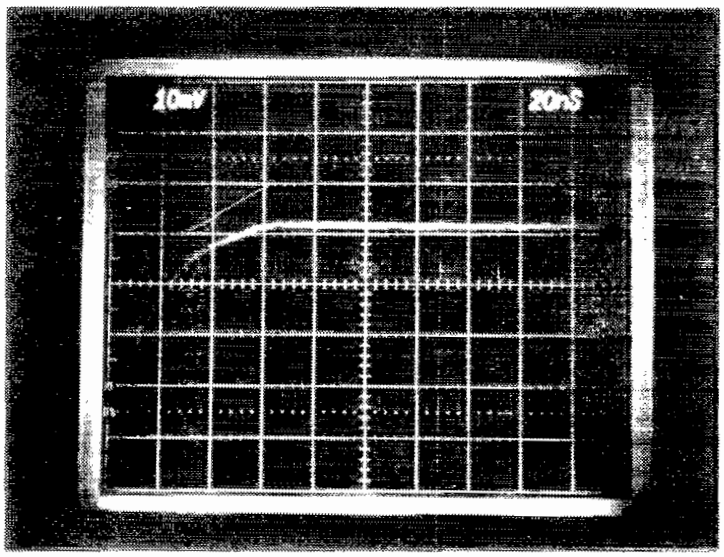

D5

FIGURE A5 (Continued)
B AND D DATA FOR +30 KV

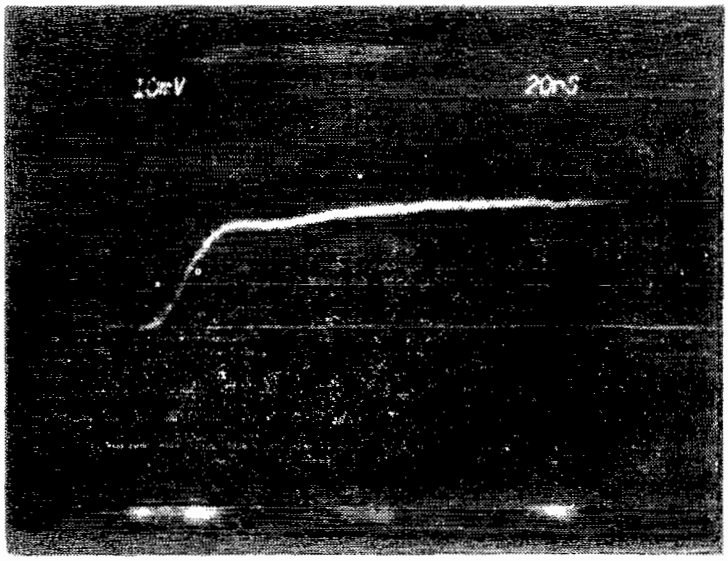

B1

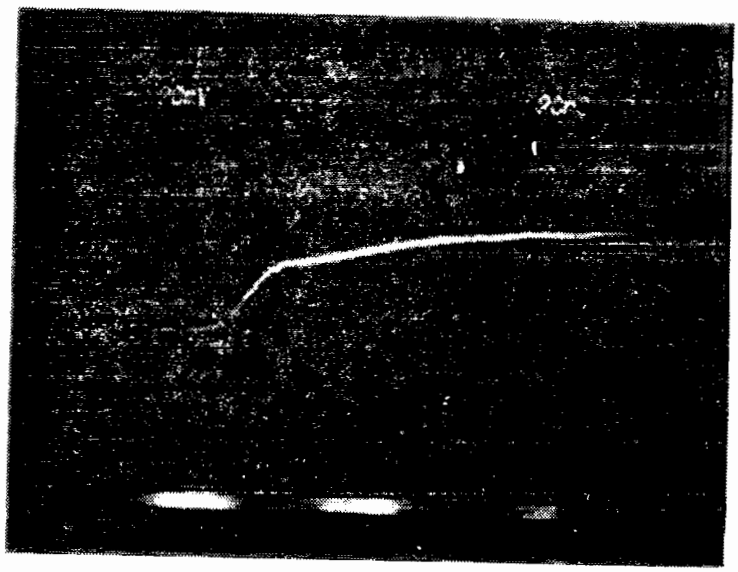

D1

FIGURE A6
B AND D DATA FOR +40 KV

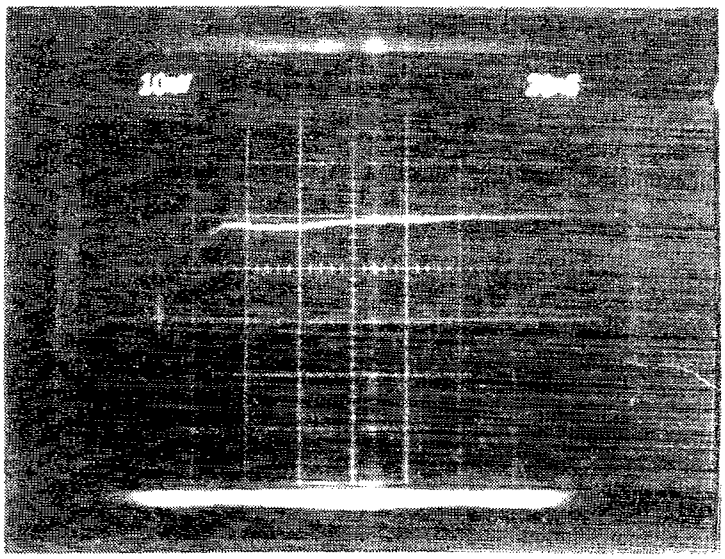

B3

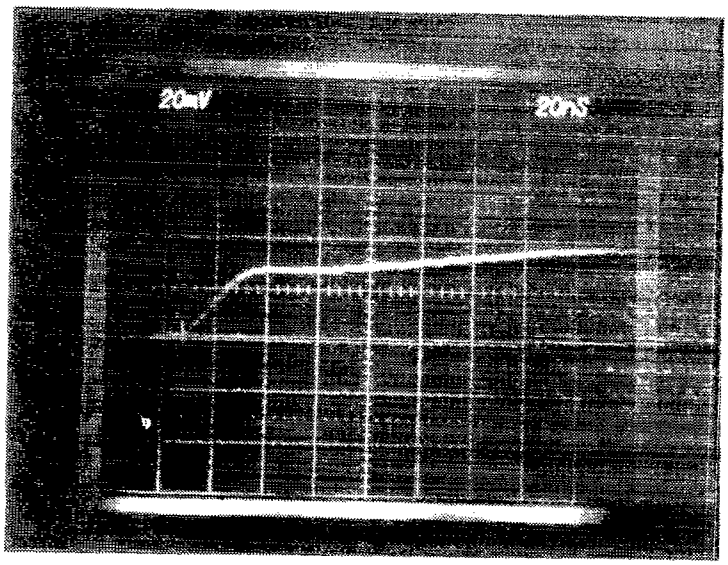

D3

FIGURE A6 (Continued)
B AND D DATA FOR +40 KV

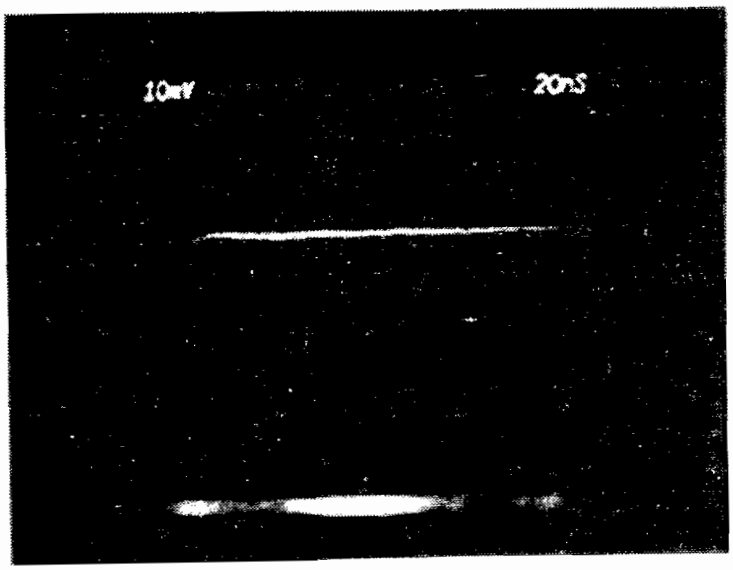

B5

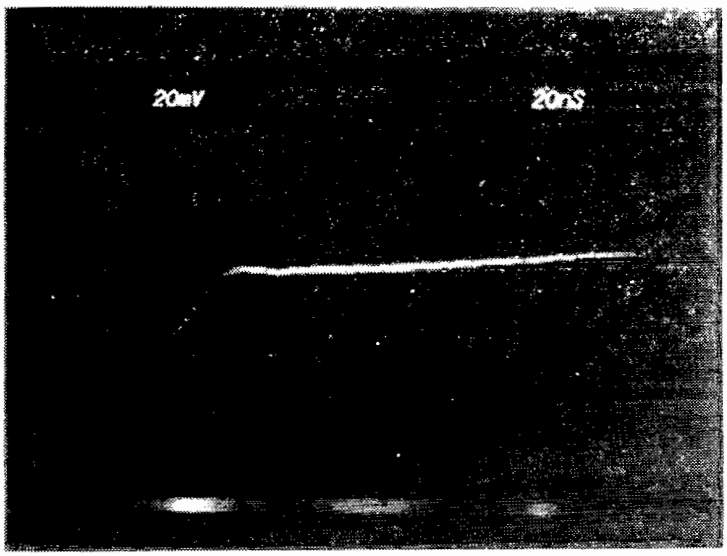

D5

FIGURE A6 (Continued)
B AND D DATA FOR +40 KV

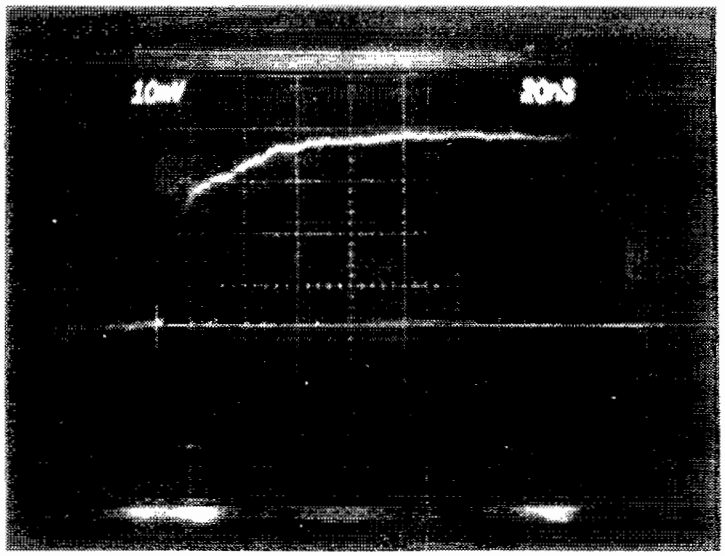

B1

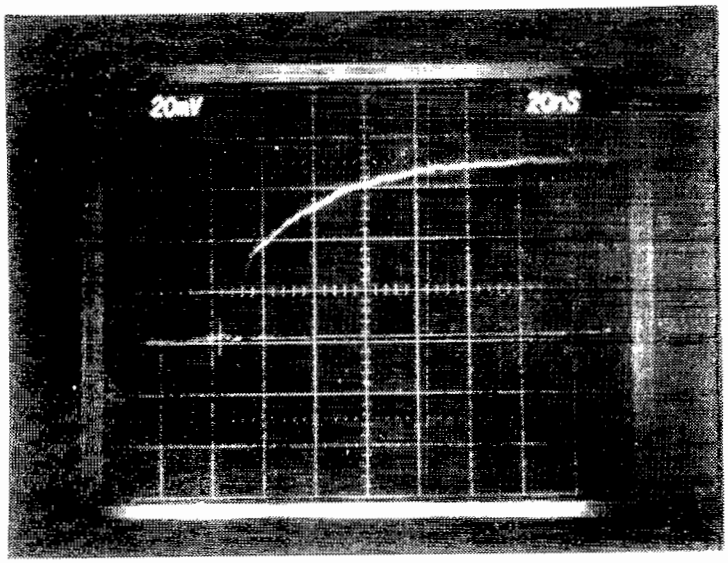

D1

FIGURE A7
B AND D DATA FOR +60 KV

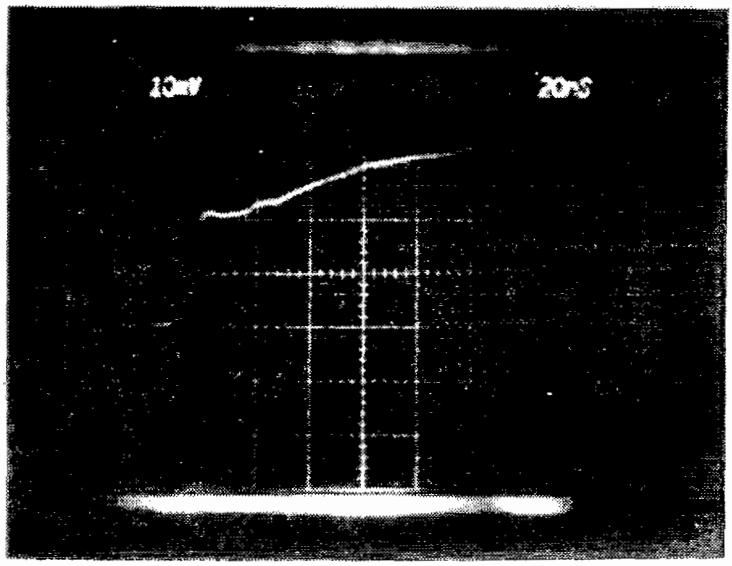

B3

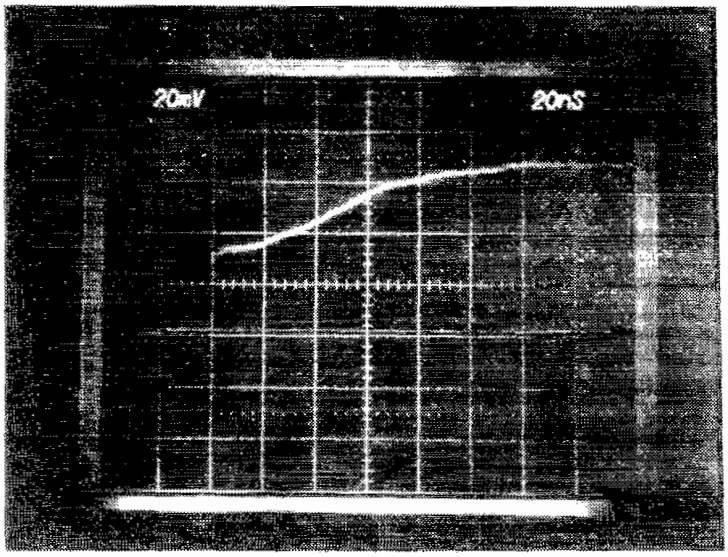

D3

FIGURE A7 (Continued)

B AND D DATA FOR +60 KV

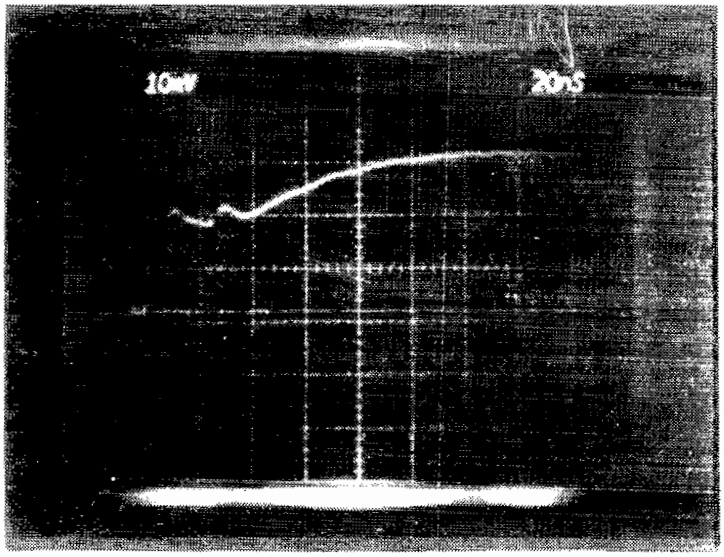

B5

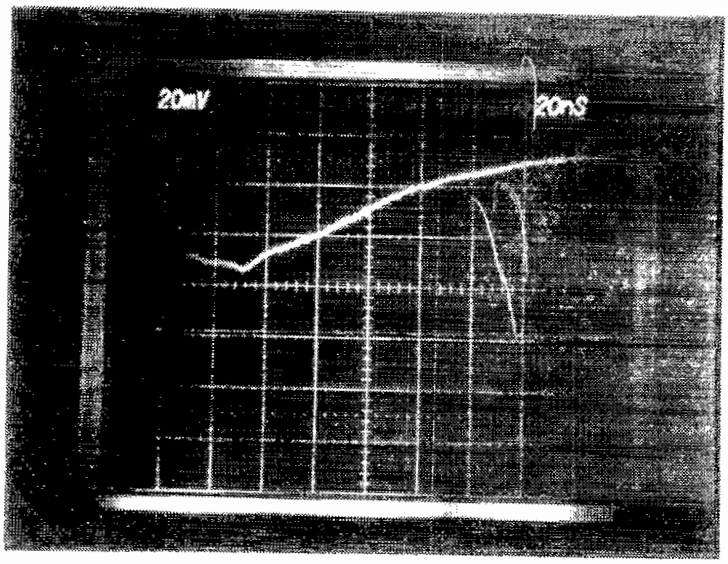

D5

FIGURE A7 (Continued)
B AND D DATA FOR +60 KV

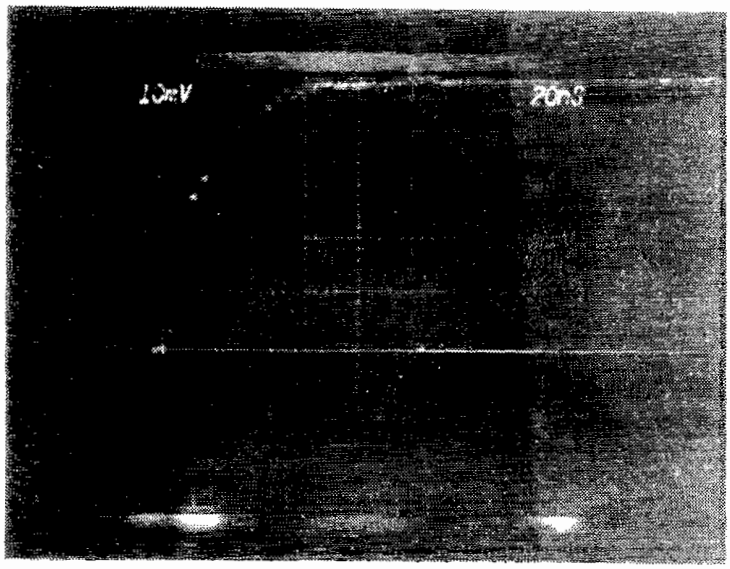

B1

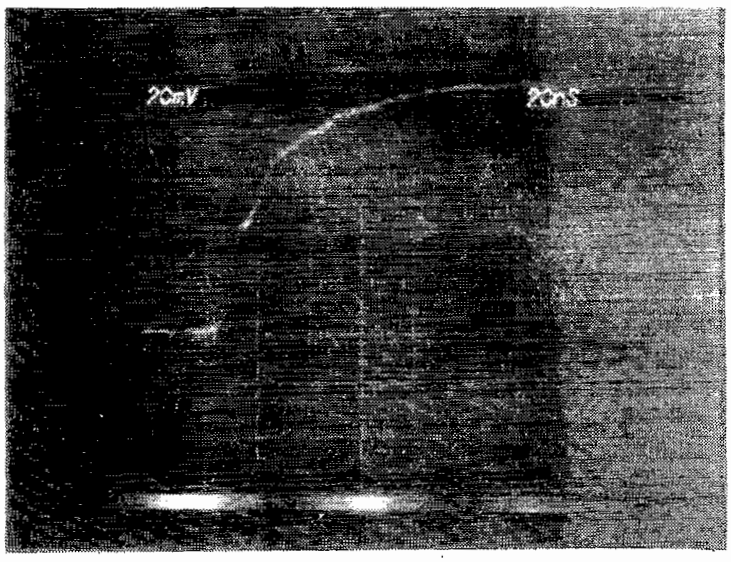

D1

FIGURE A8
B AND D DATA FOR +80 KV - SET 1

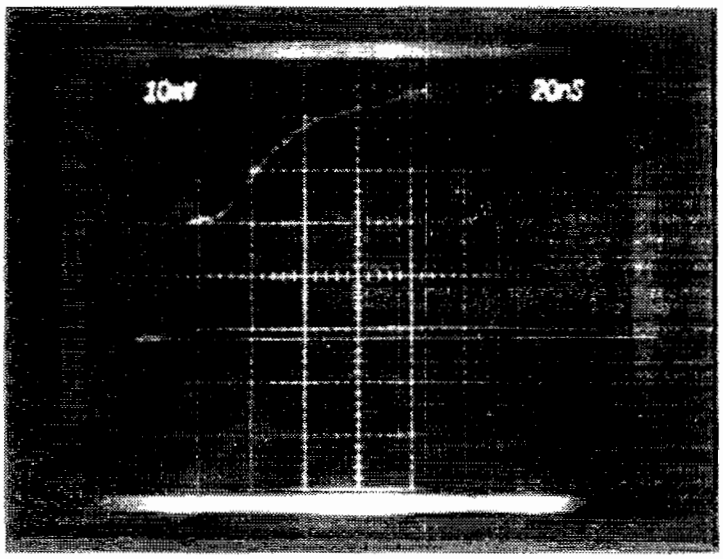

B3

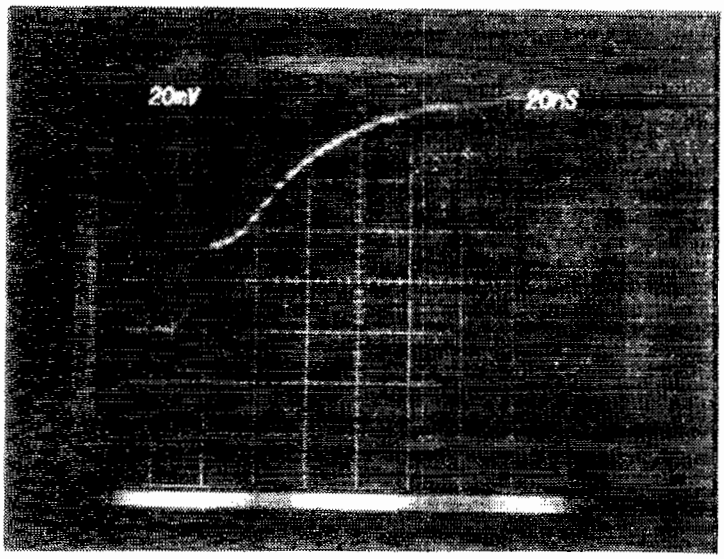

D3

FIGURE A8 (Continued)
B AND D DATA FOR +80 KV - SET 1

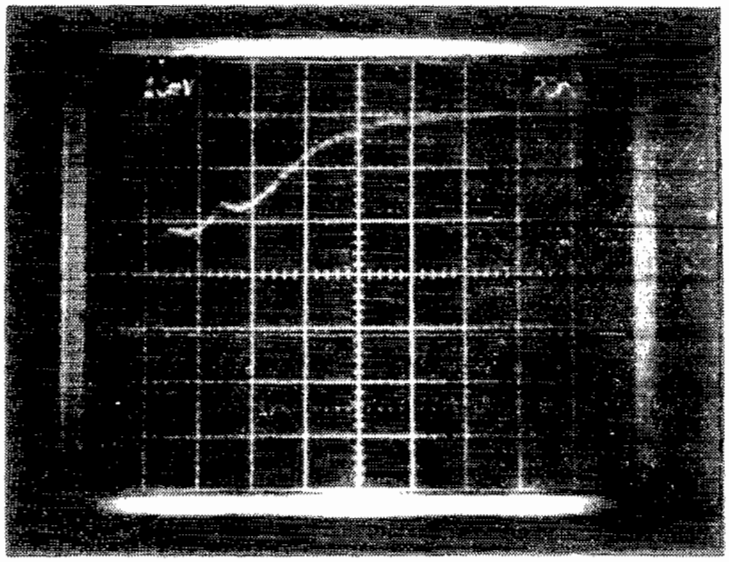

B5

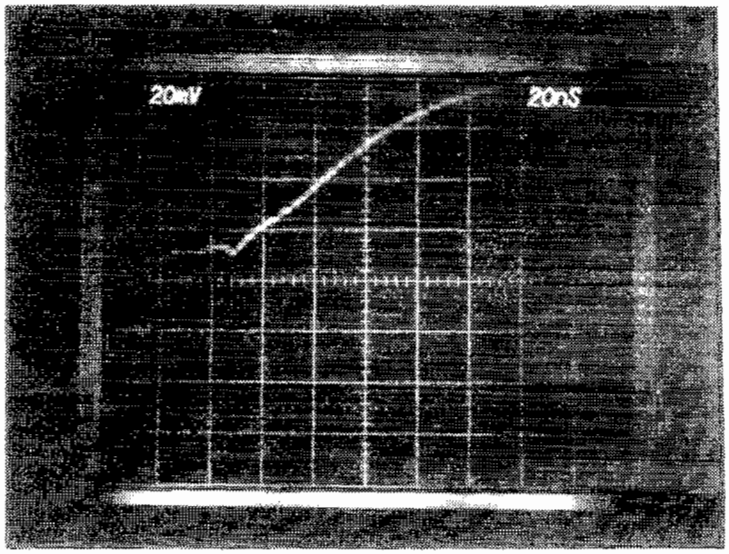

D5

FIGURE A8 (Continued)
B AND D DATA FOR +80 KV - SET 1

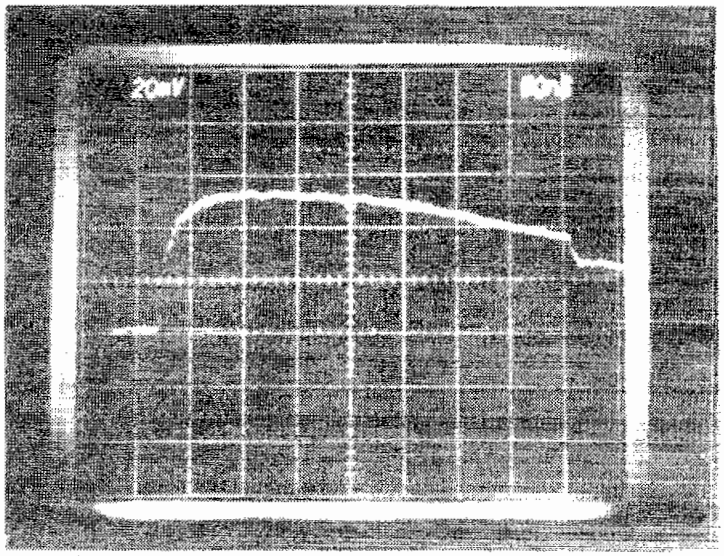

B1

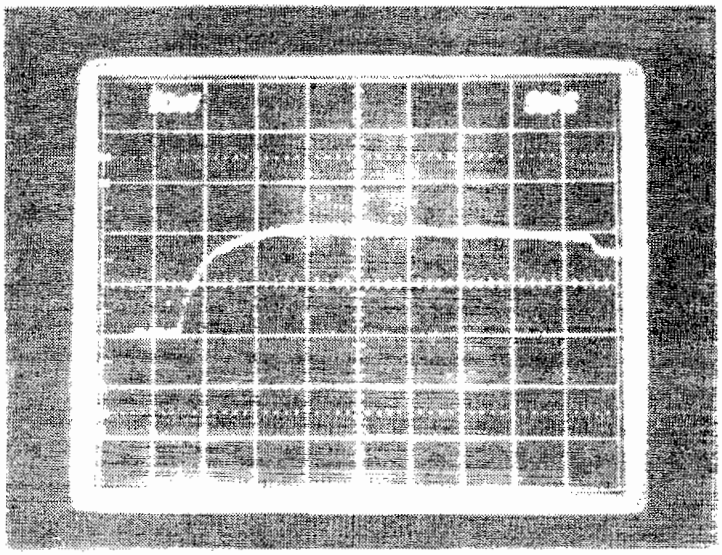

D1

FIGURE A9
B AND D DATA FOR +80 KV - SET 2

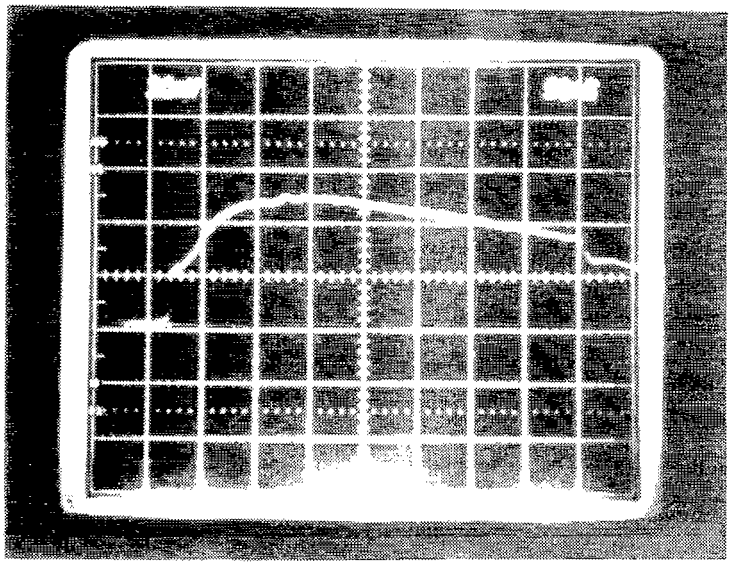

B3

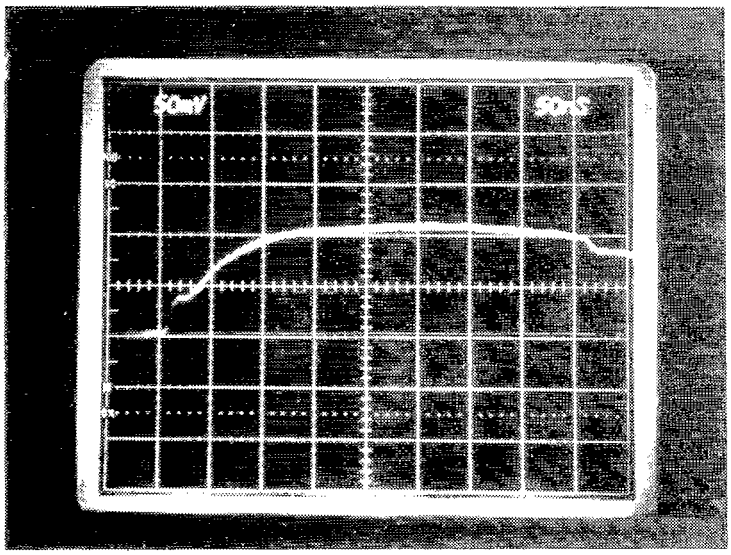

D3

FIGURE A9 (Continued)
B AND D DATA FOR +80 KV - SET 2

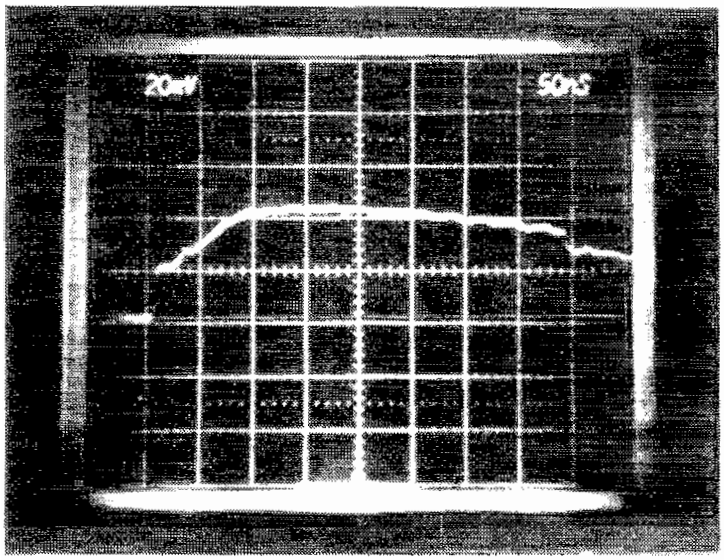

B5

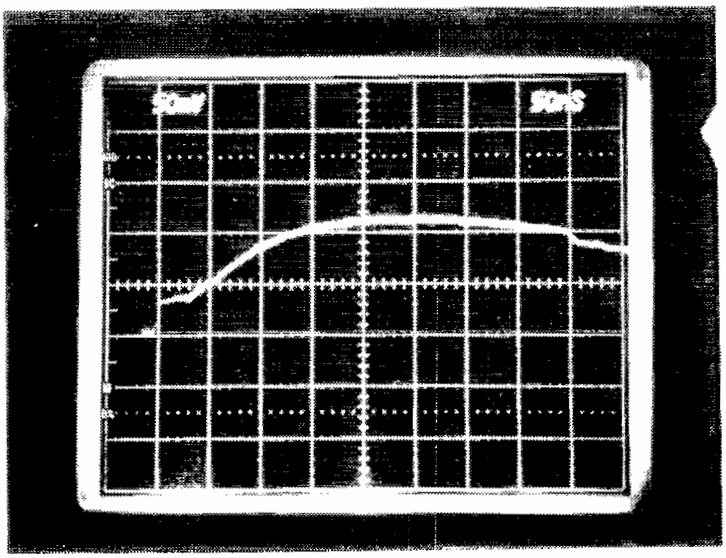

D5

FIGURE A9 (Continued)
B AND D DATA FOR +80 KV - SET 2

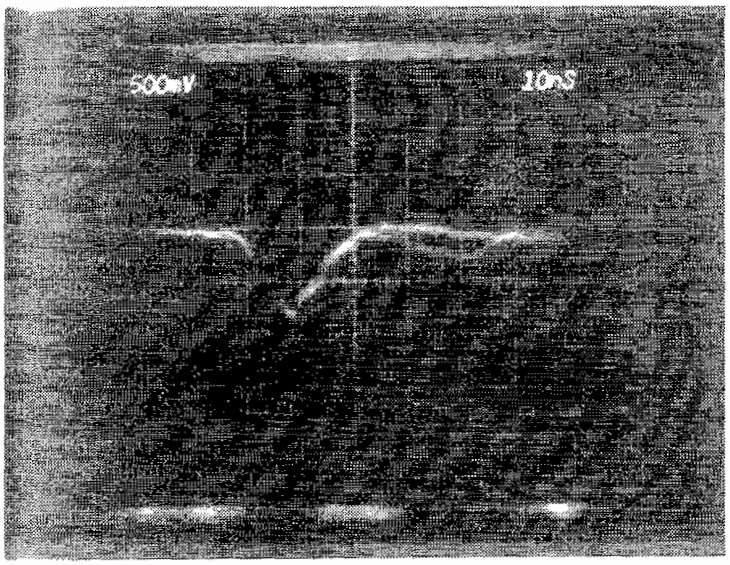

$\dot{B}1$

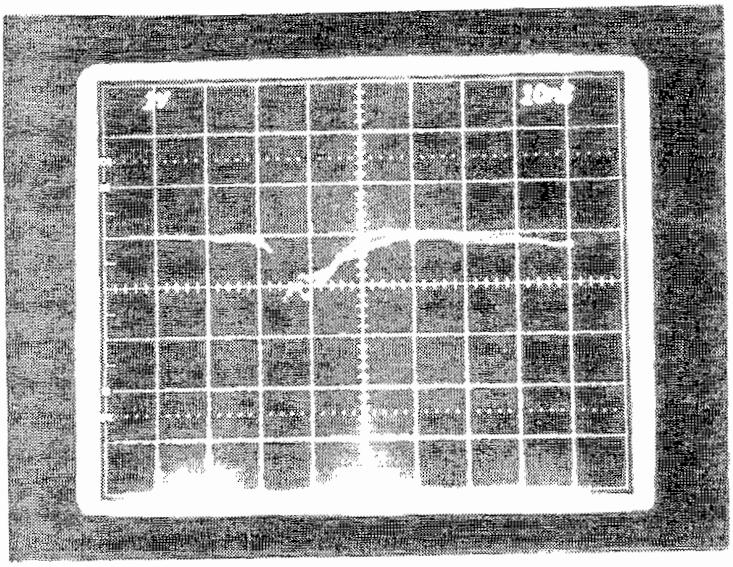

$\dot{D}1$

FIGURE A10

$\dot{B}$ AND $\dot{D}$ DATA FOR -30 KV

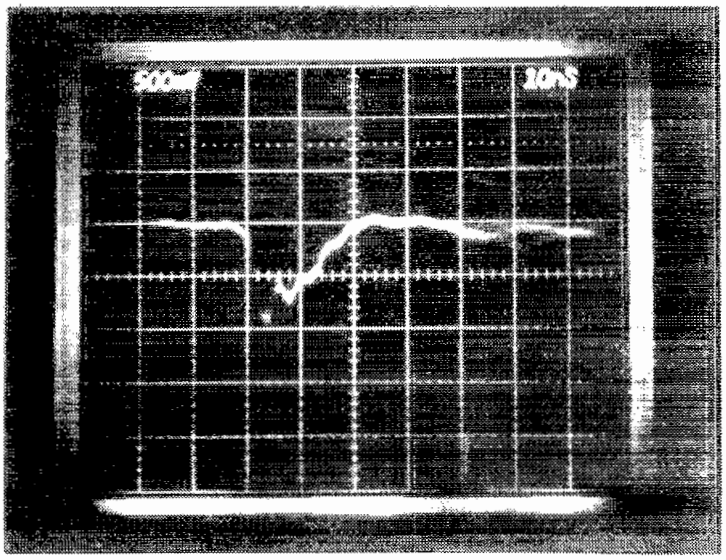

$\dot{B}3$

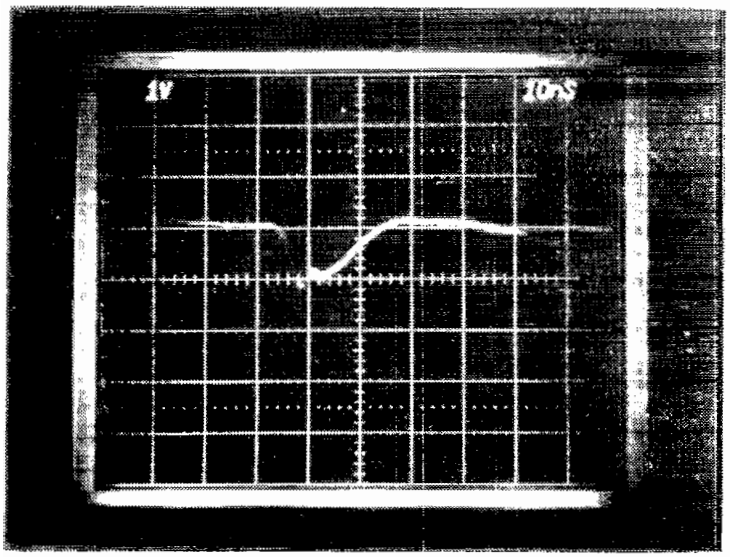

$\dot{D}3$

FIGURE A10 (Continued)

$\dot{B}$ AND $\dot{D}$ DATA FOR -30 KV

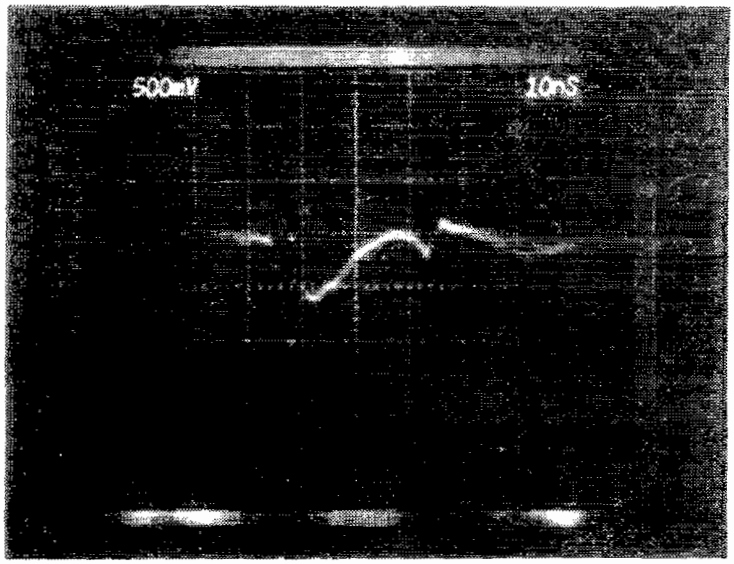

$\dot{B}5$

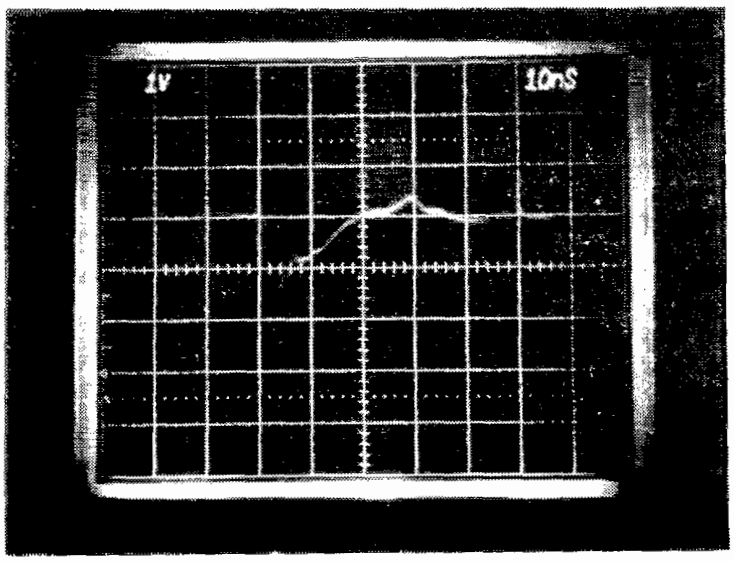

$\dot{D}5$

FIGURE A10 (Continued)
$\dot{B}$ AND $\dot{D}$ DATA FOR -30 KV

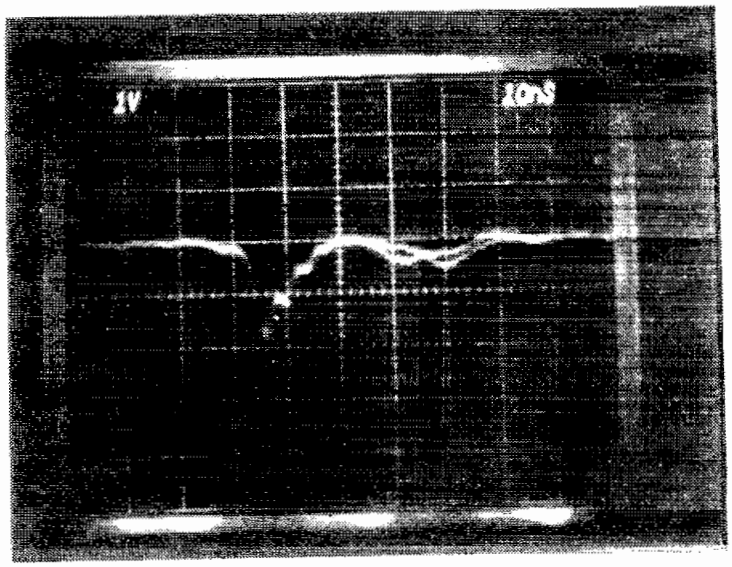

$\dot{B}1$

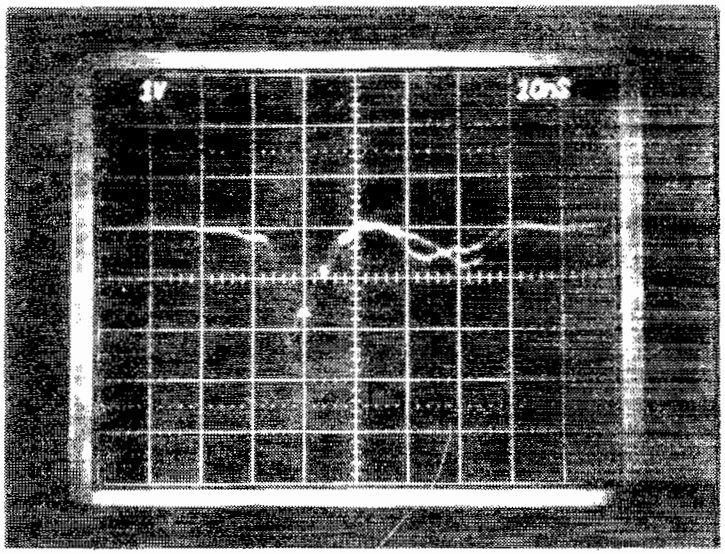

$\dot{D}1$

FIGURE A11

$\dot{B}$ AND $\dot{D}$ DATA FOR -40 KV

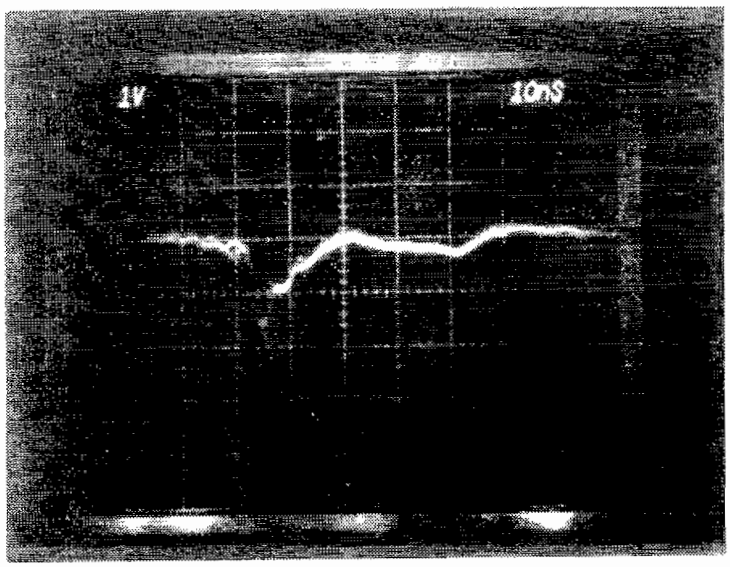

B3

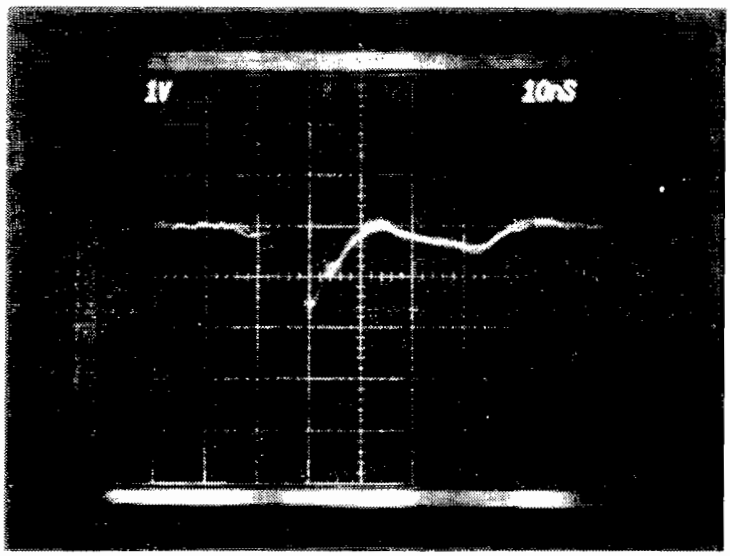

D3

FIGURE A11 (Continued)
B AND D DATA FOR -40 KV

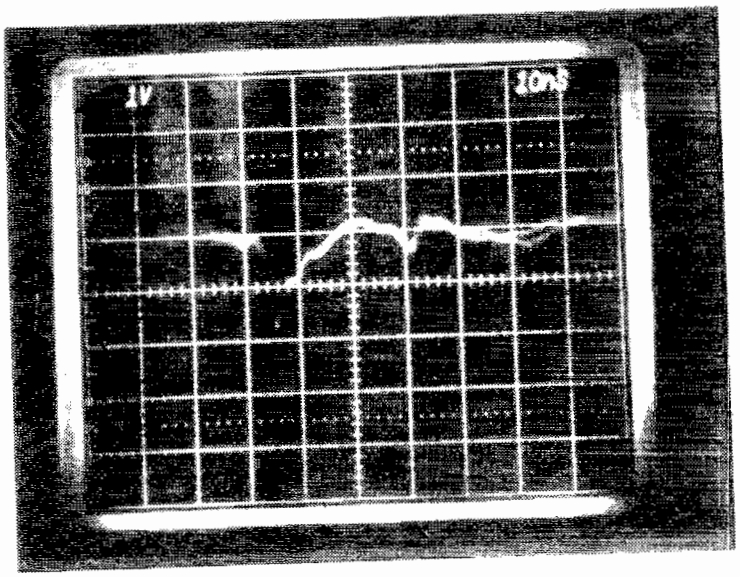

B5

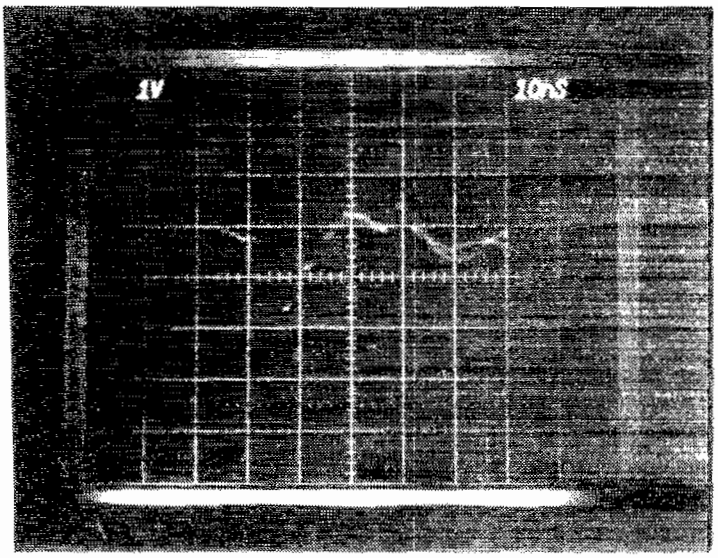

D5

FIGURE A11 (Continued)
B AND D DATA FOR -40 KV

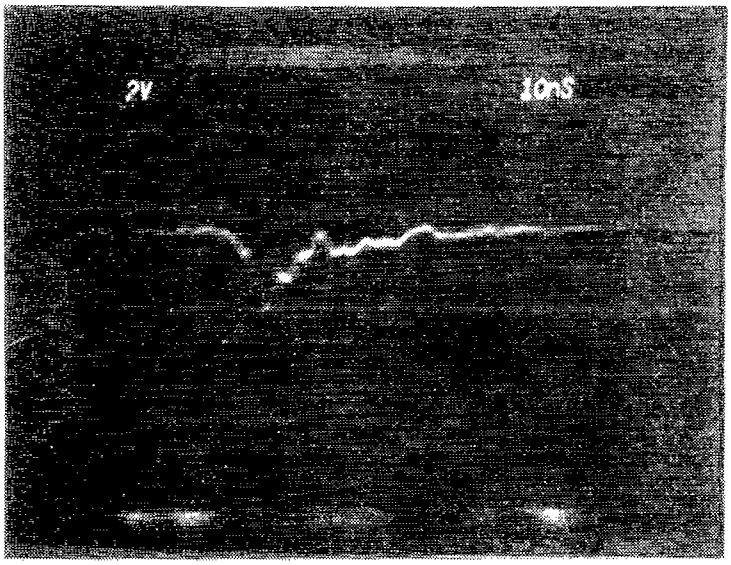

$\dot{B}_1$

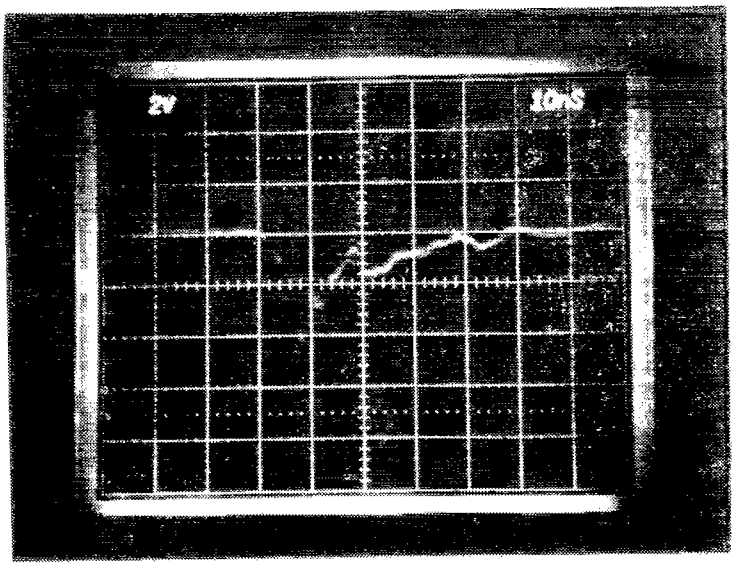

$\dot{D}_1$

FIGURE A12

$\dot{B}$ AND $\dot{D}$ DATA FOR -60 KV

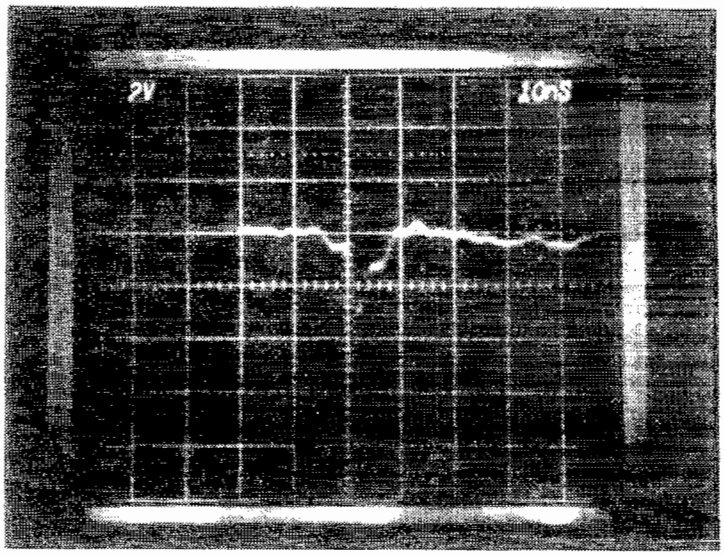

$\dot{B}3$

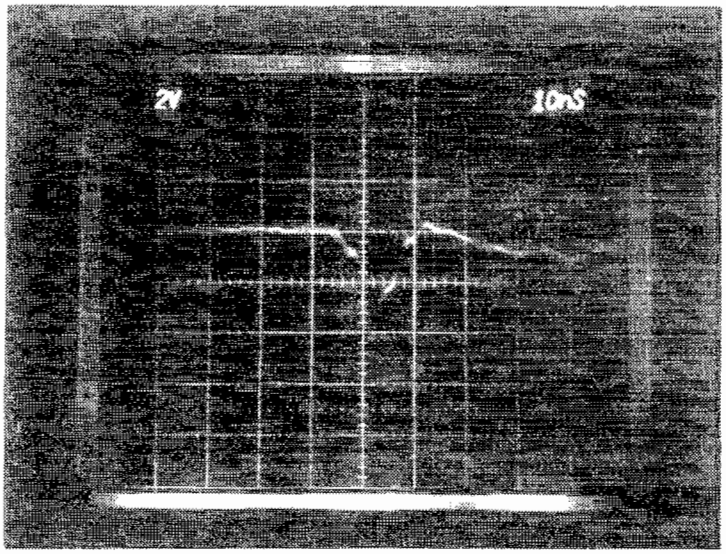

$\dot{D}3$

FIGURE A12 (Continued)
$\dot{B}$ AND $\dot{D}$ DATA FOR -60 KV

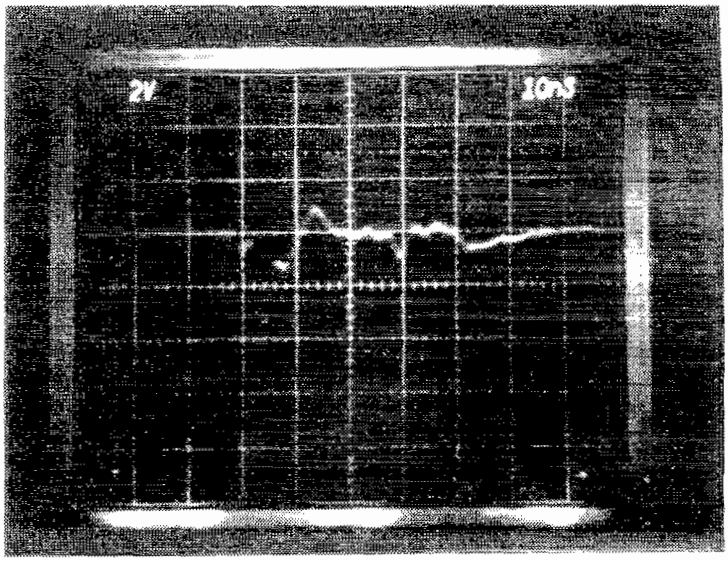

B5

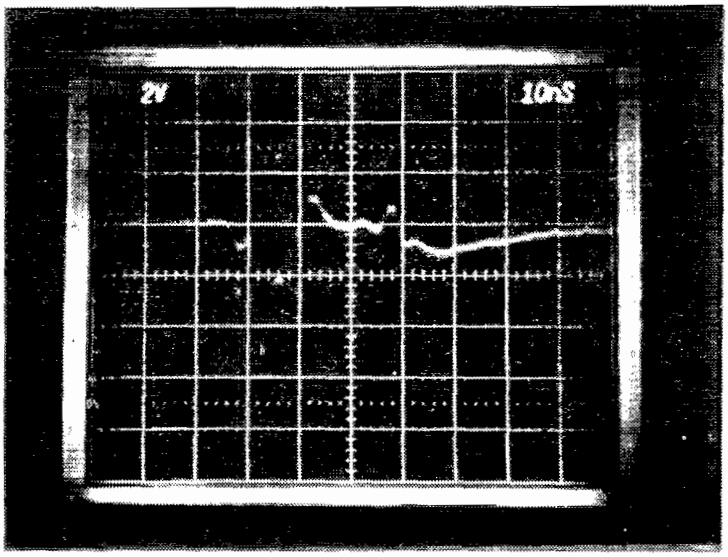

D5

FIGURE A12 (Continued)
B AND D DATA FOR -60 KV

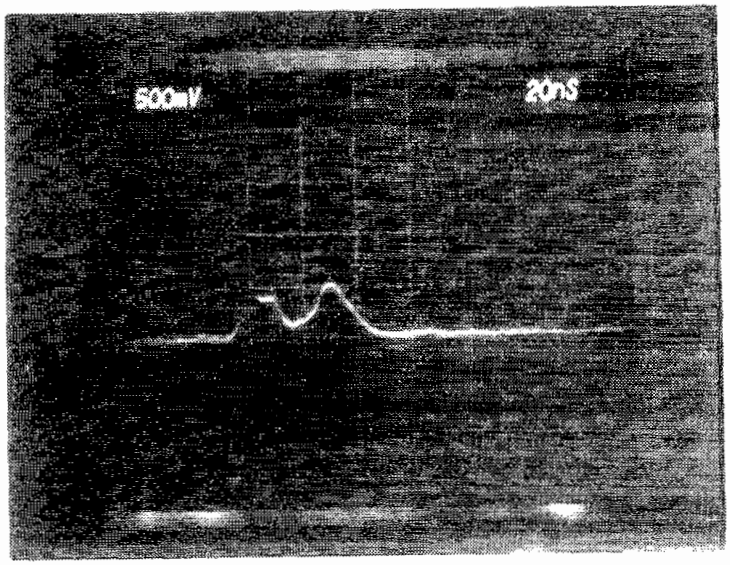

$\dot{B}1$

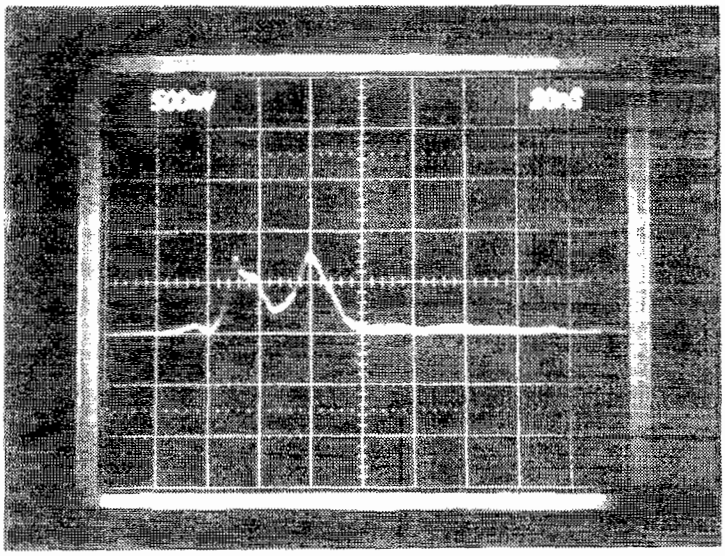

$\dot{D}1$

FIGURE A13

$\dot{B}$ AND $\dot{D}$ DATA FOR +30 KV

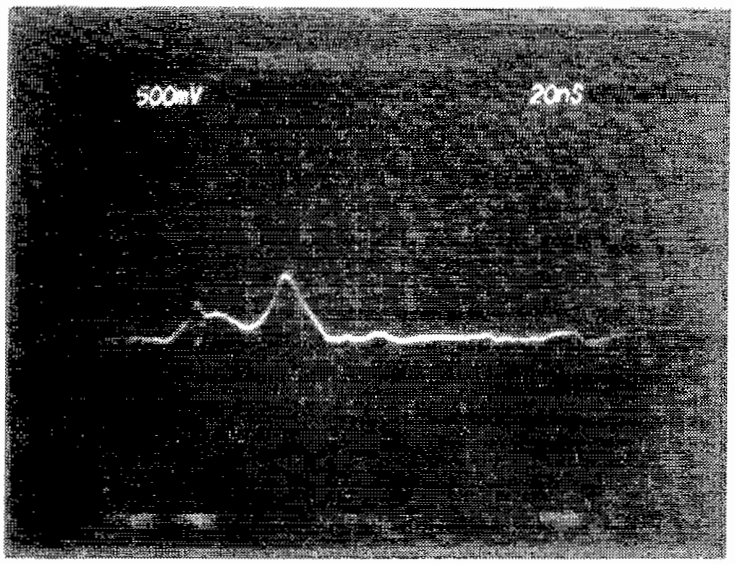

$\dot{B}3$

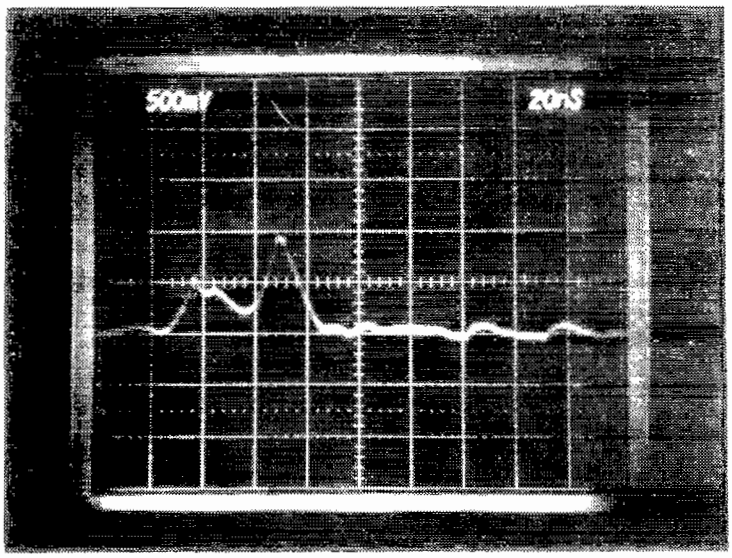

$\dot{D}3$

FIGURE A13 (Continued)
$\dot{B}$ AND $\dot{D}$ DATA FOR +30 KV

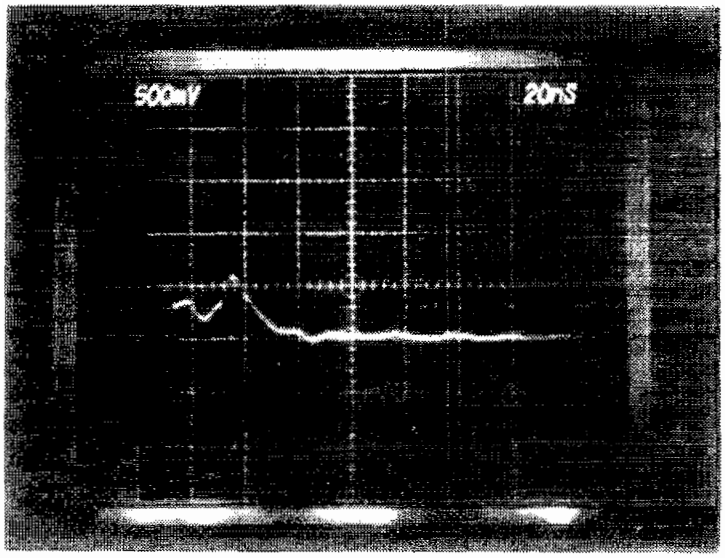

$\dot{B}5$

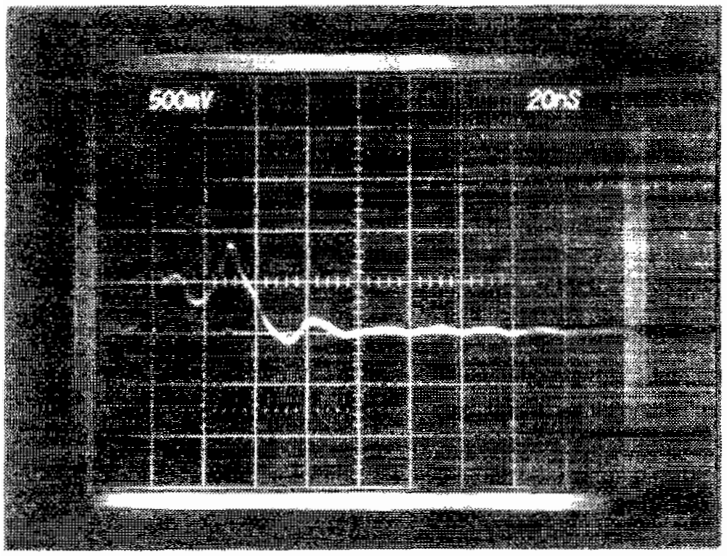

$\dot{D}5$

FIGURE A13 (Continued)
$\dot{B}$ AND $\dot{D}$ DATA FOR +30 KV

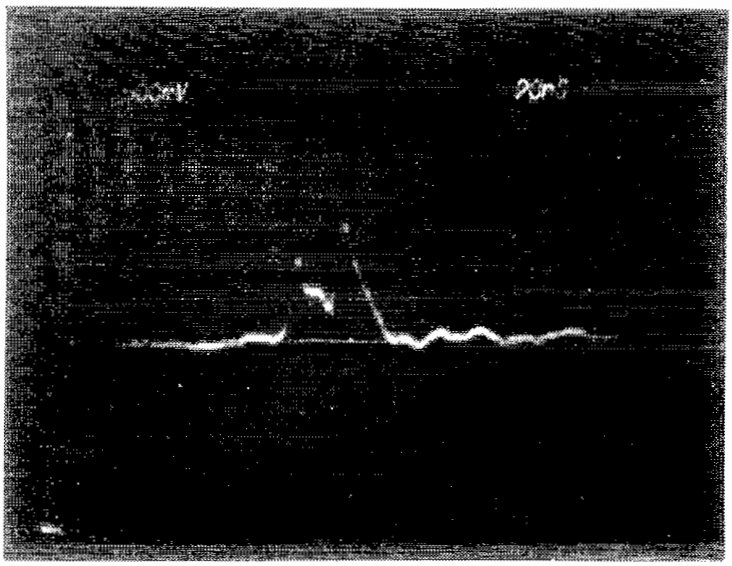

$\dot{B}1$

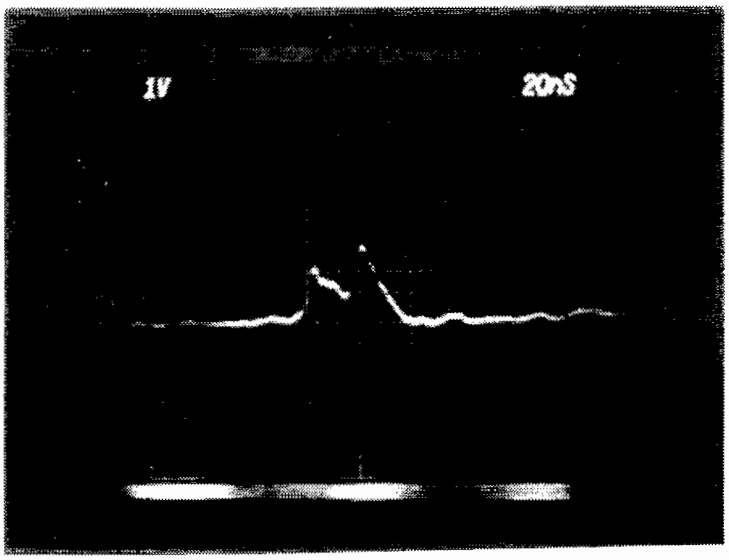

$\dot{D}1$

FIGURE A14

$\dot{B}$ AND $\dot{D}$ DATA FOR +40 KV

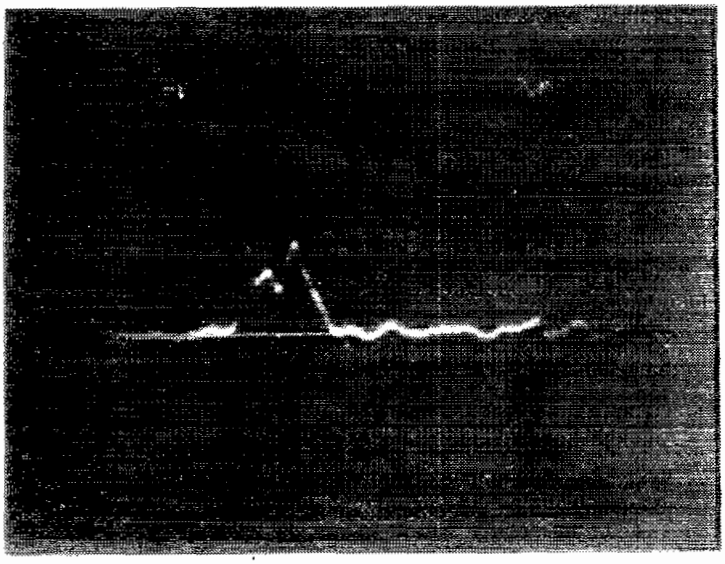

$\dot{B}3$

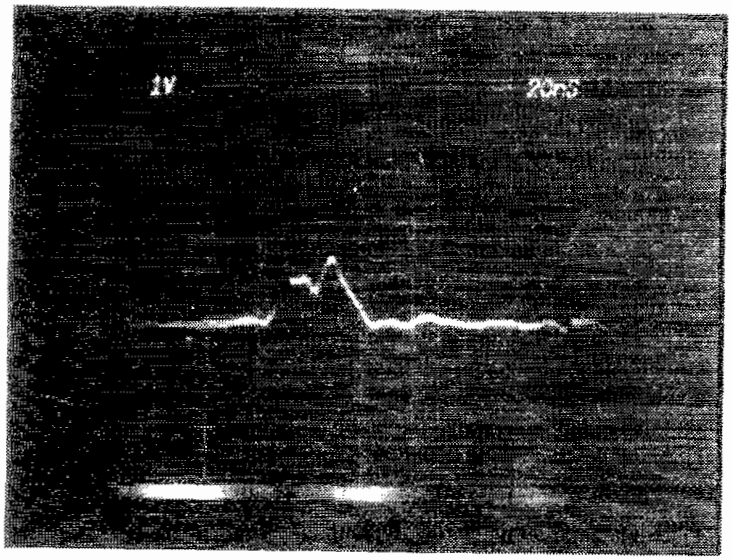

$\dot{D}3$

FIGURE A14 (Continued)

$\dot{B}$ AND $\dot{D}$ DATA FOR +40 KV

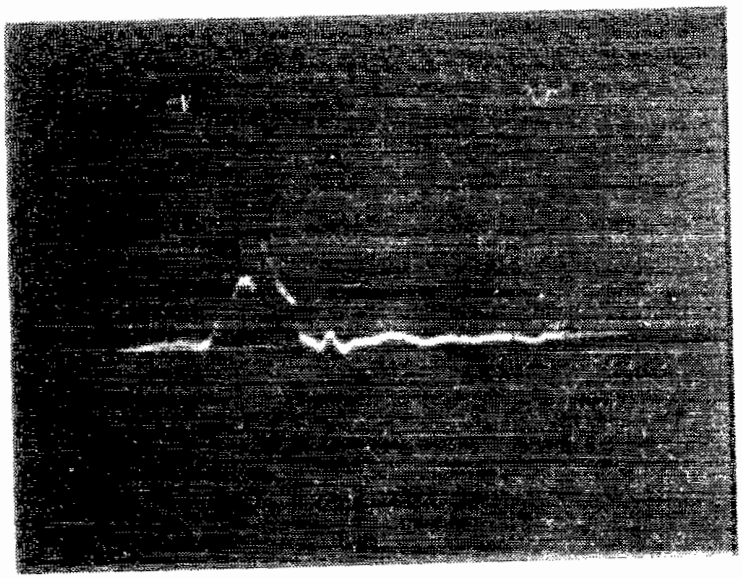

$\dot{B}5$

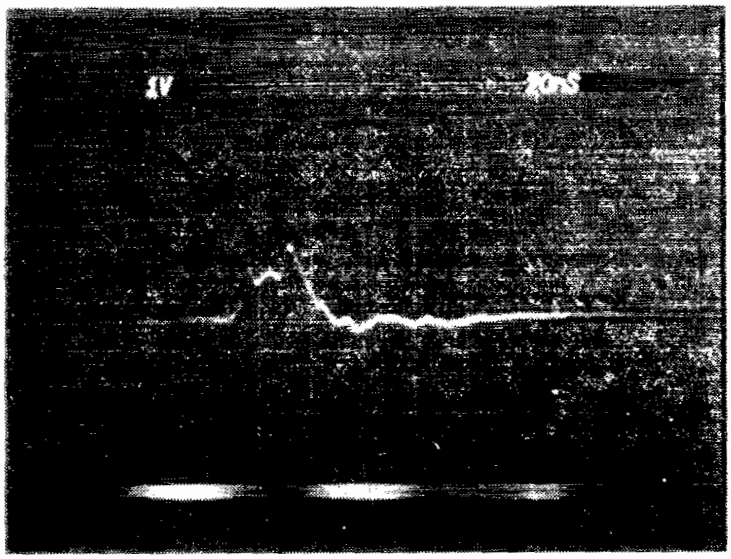

$\dot{D}5$

FIGURE A14 (Continued)
$\dot{B}$ AND $\dot{D}$ DATA FOR +40 KV

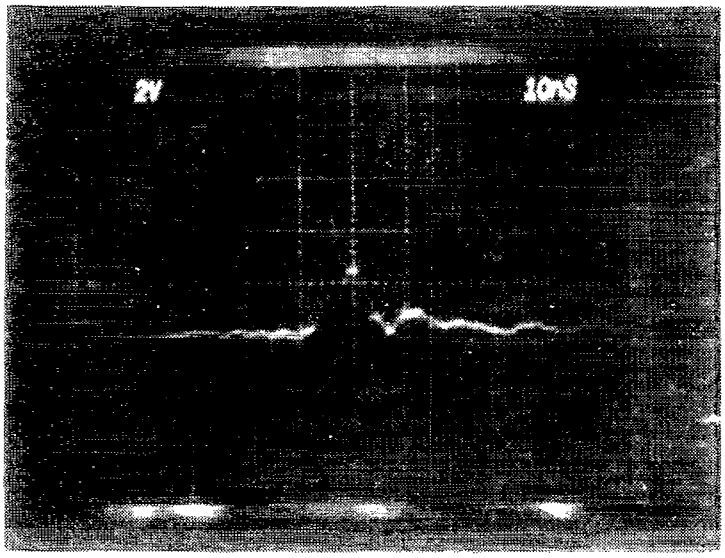

B1

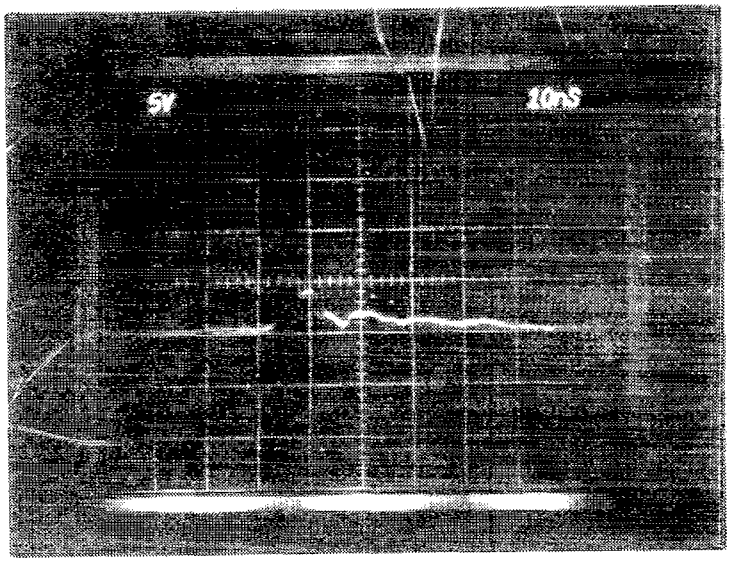

D1

FIGURE A15
B AND D DATA FOR +60 KV

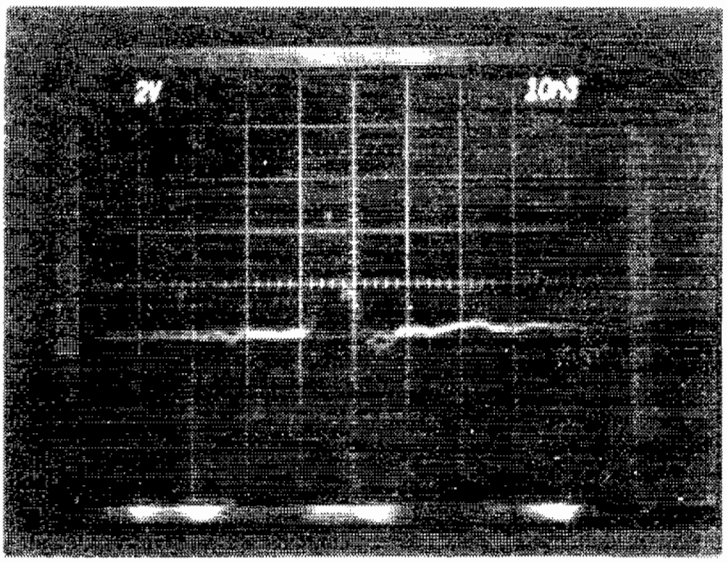

$\dot{B}3$

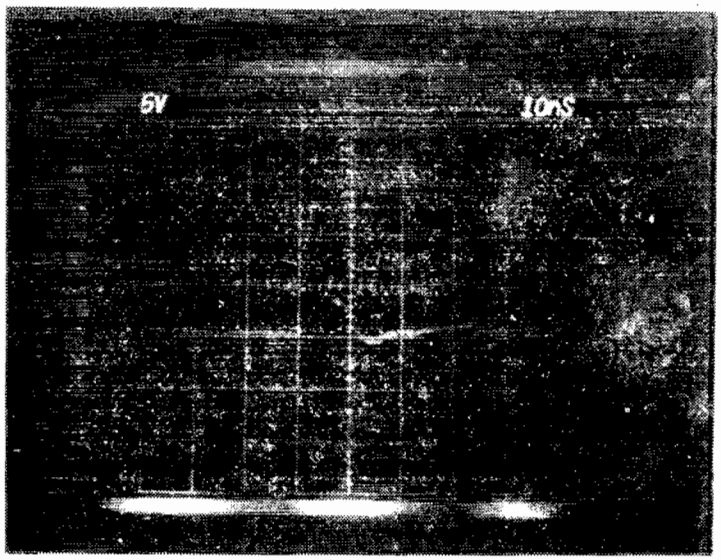

$\dot{D}3$

FIGURE A15 (Continued)
$\dot{B}$ AND $\dot{D}$ DATA FOR +60 KV

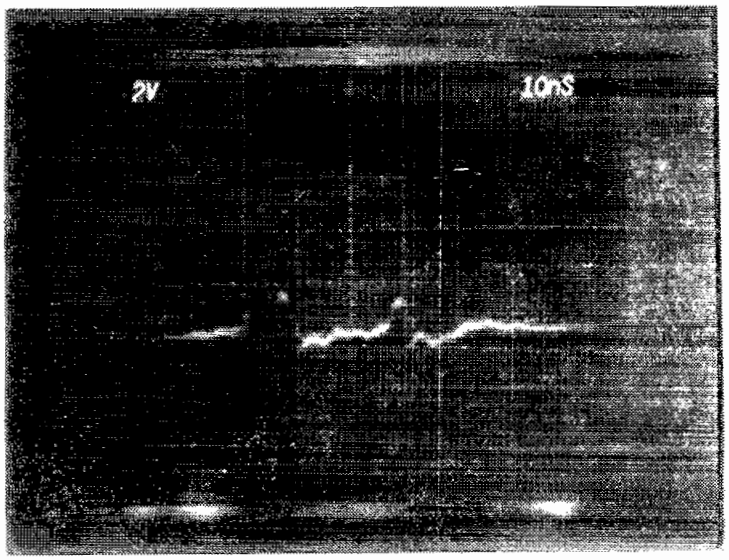

B5

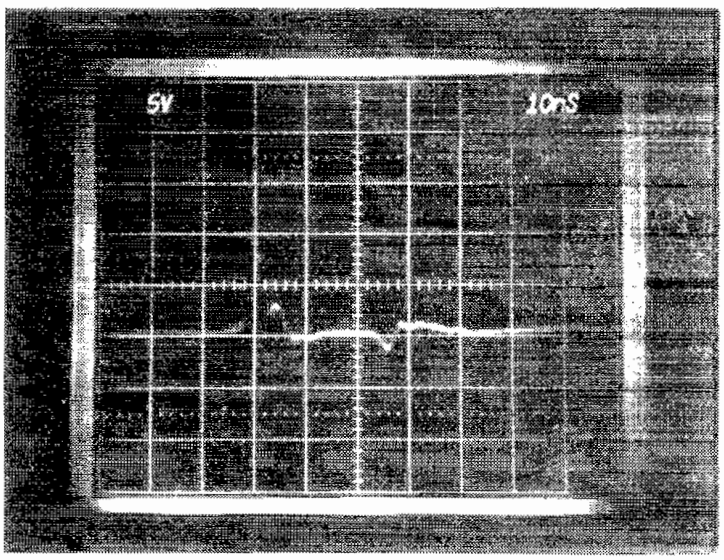

D5

FIGURE A15 (Continued)
B AND D DATA FOR +60 KV

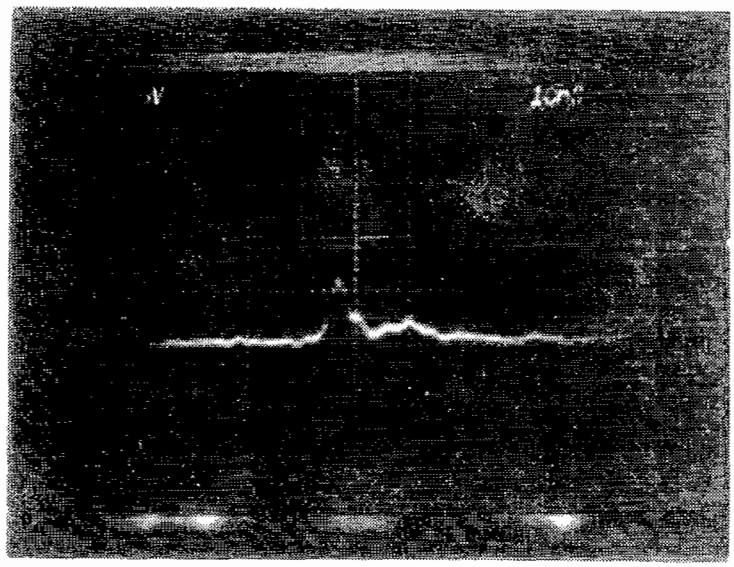

$\dot{B}1$

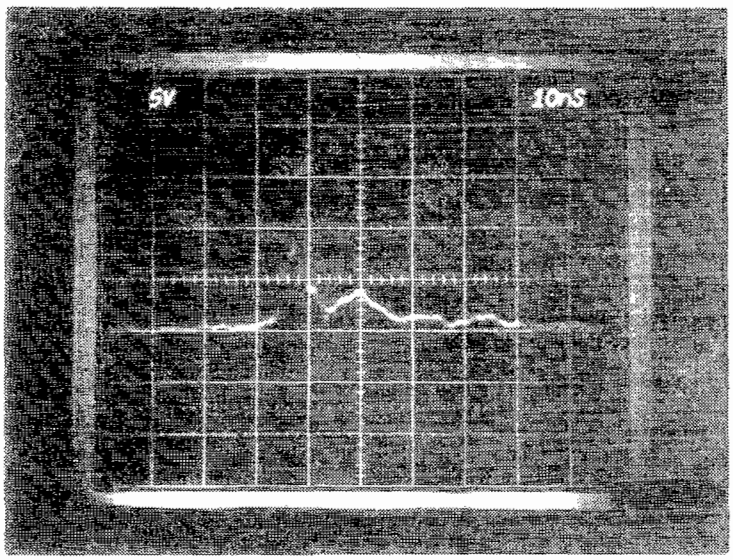

$\dot{D}1$

FIGURE A16

$\dot{B}$ AND $\dot{D}$ DATA FOR +80 KV

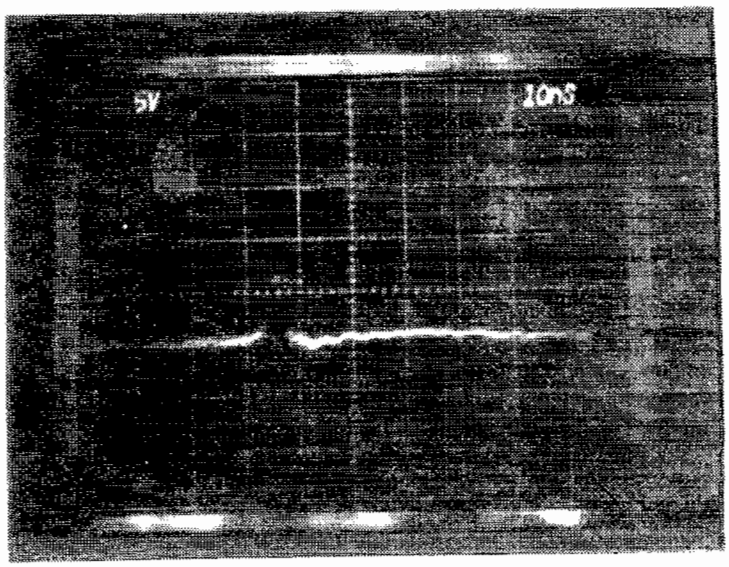

$\dot{B}3$

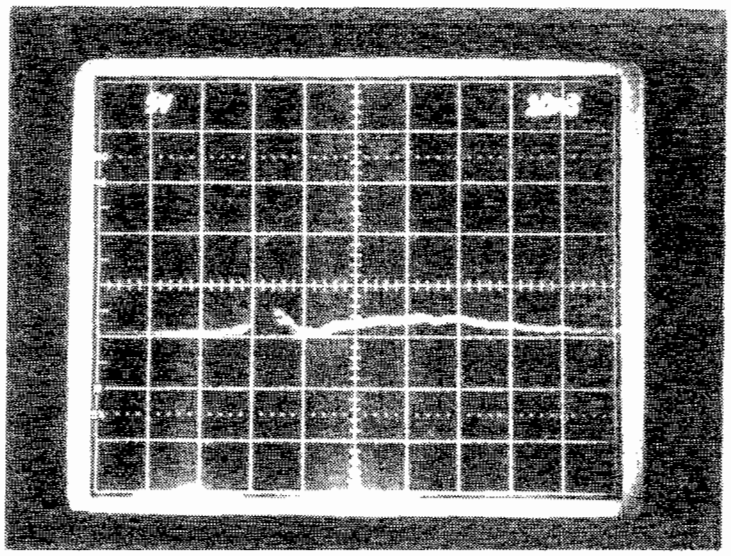

$\dot{D}3$

FIGURE A16 (Continued)
$\dot{B}$ AND $\dot{D}$ DATA FOR +80 KV

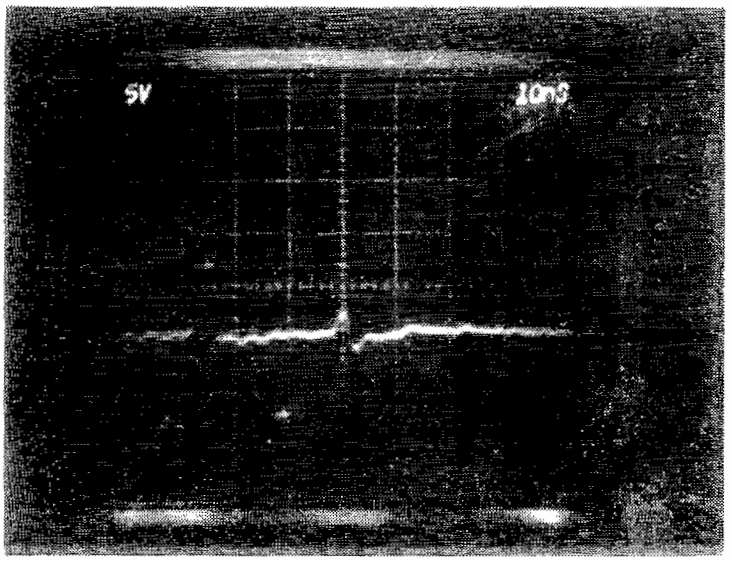

$\dot{B}5$

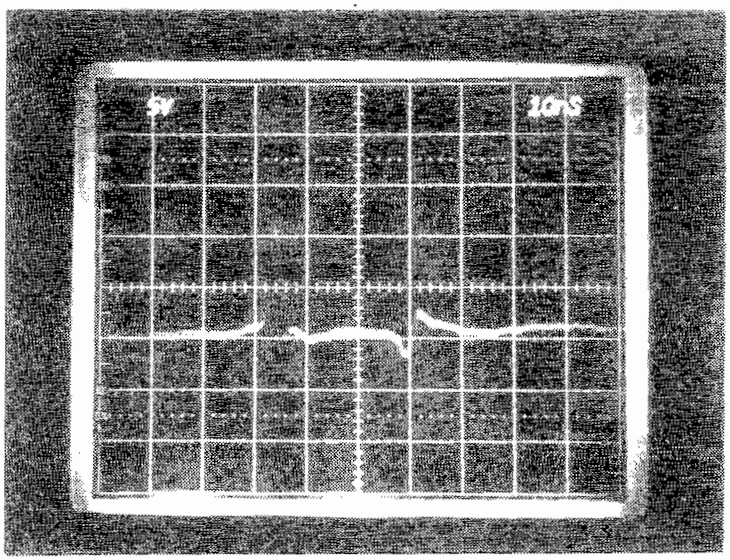

$\dot{D}5$

FIGURE A16 (Continued)
$\dot{B}$ AND $\dot{D}$ DATA FOR +80 KV